UNIVERSITÀ DEL SALENTO
FACOLTÀ DI SCIENZE MM. FF. NN.

Dott. Michele Bianco

PhD Thesis

ATLAS RPC
certification and commissioning with cosmic rays

Supervisors:
Prof. Edoardo GORINI

Dott. Gabriele CHIODINI

Dottorato di ricerca in Fisica XIX ciclo
settore scientifico FIS/04

To my parents

La ricerca scientifica
consiste nel vedere quello che ogni altro ha già visto
e nel pensare quello che nessun altro ha mai pensato.
P. Szent-Gyorgy

Contents

Introduction **1**

1 Physics Reach at LHC **4**
1.1 Introduction 4
1.2 The Standard Model 4
1.3 The Electroweak Theory 6
1.3.1 Introduction 6
1.3.2 Generation of Bosons Masses by Electroweak Symmetry Breaking 8
1.4 Higgs Bosons Mass Constraints 12
1.4.1 Open questions 13
1.5 Supersymmetry 14
1.5.1 The Minimal Supersymmetric Standard Model (MSSM) 15
1.5.2 GUT and mSUGRA 16
1.6 Search for the S.M. Higgs at LHC 18
1.6.1 Search for the MSSM Higgs 22
1.7 Other physics measurements at LHC 22

2 ATLAS experiment at LHC **25**
2.1 Introduction 25
2.2 CERN Accelerator System and LHC 25
2.3 ATLAS general overview 27
2.3.1 Magnet System 30
2.3.2 Inner Detector 31
2.3.3 The Calorimeter System 33
2.3.4 Muon Spectrometer 37
2.3.5 Trigger System 42

3 The Resistive Plate Chambers in the ATLAS experiment 45
3.1 Introduction . . . 45
3.2 RPC working principle . . . 46
3.3 The ATLAS RPC detector . . . 48
3.4 Muon Selection in the ATLAS Barrel Region . . . 53
3.4.1 Muon LVL1 trigger technology . . . 53
3.4.2 Muon Selection Algorithm . . . 55
3.4.3 Coincidence Windows and Cabling . . . 56

4 ATLAS RPC cosmic ray test facility in Lecce 60
4.1 Introduction . . . 60
4.2 Test Facility Overview . . . 61
4.2.1 Mechanical Structure . . . 62
4.2.2 Power System . . . 64
4.2.3 The Data Acquisition System . . . 65
4.2.4 The Detector Control System . . . 68
4.2.5 Trigger . . . 68
4.3 Offline Analysis . . . 70
4.4 Test Performed . . . 81
4.4.1 Data Taking . . . 81
4.4.2 Quality Assurance tests . . . 81
4.5 Results Presentation . . . 86

5 Results of ATLAS RPC tests in Lecce 88
5.1 Introduction . . . 88
5.2 High Voltage Correction for Temperature and Pressure . . . 89
5.3 Gas Volume Efficiency, Electronic Efficiency and Plane Efficiency . . . 96
5.4 Cluster Size and Noise as a Function of Front-End Threshold . 99
5.5 Current and Noise as function of Temperature . . . 101
5.6 HV Working Point Definition and its Properties . . . 106
5.7 Conclusion . . . 114

6 RPC test with cosmic rays in the ATLAS experiment 115
6.1 Introduction . . . 115
6.2 Sector 13 set-up . . . 115
6.3 Data Taking in Sector 13 . . . 118
6.3.1 Auto Trigger Strategy . . . 118

6.3.2 Data Taking 118
6.4 ATLAS Offline Software: ATHENA 120
6.5 RPC Sector 13 Data Quality Control 121
6.5.1 CMA Timing 121
6.5.2 Strip profiles, CMA and PAD control 121
6.6 A RPC Standalone track reconstruction program 127
6.6.1 The Pattern Recognition and Tracking Algorithm . . . 127
6.6.2 Efficiency determination 131
6.7 Efficiency and Cluster Size measurements 137
6.8 Conclusions 142

Summary and Outlook **144**

Bibliography **146**

Introduction

This thesis describes the experimental technique used and the analysis results for quality assurance of the RPC trigger chambers of the ATLAS experiment at the Large Hadron Collider (LHC) at CERN laboratory, in Geneve. Detailed results of the tests carried out at the Test Stand facility built in Lecce at Salento University and INFN laboratory and the ATLAS Sector 13 pre-commissioning will be given.

The LHC will provide proton-proton collisions at the center of mass energy of 14 TeV and luminosity $10^{34} cm^{-2} s^{-1}$. This energy is almost one order of magnitude higher than what has been achieved in previous accelerators. Main goal for the LHC will be the search for the Higgs boson, which in the Standard Model of particle physics is, responsible for all particle masses through the spontaneous symmetry breaking mechanism. Moreover, it will allow to explore physics in the TeV region and search for physics beyond the Standard Model.
The ATLAS detector is a general purpose experiment and it is composed of several sub-detector with very well defined purpose. ATLAS is designed to search Higgs signal in a very wide range of energy (100 GeV - 1 TeV). Moreover if will also allow precision measurements on beauty and top quark physics, to study CP violation and last but not least will allow the search for supersymmetric particles.

High momentum muon final states are amongst the most promising and robust signature of physics at LHC. To exploit this potential, the ATLAS Collaboration has designed a high-resolution muon spectrometer with stand-alone triggering and momentum measurement capability over a wide range of transverse momentum. Resistive Plate Chamber (RPC) are used as muon trigger chamber in the ATLAS barrel region. RPCs are gaseous detector providing typical space time-resolution of $1cm \times 1ns$. To provide muon trigger signal and allow the maximum hermeticity for the muon spectrometer

1116 units of 26 different typologies have been developed and built in Lecce University Physics Department and INFN laboratory from the RPC community.

In order to carry out a complete test on the detector performances and ensure a Quality Assurance as demanded from ATLAS design, three cosmic ray test stand has been built in Lecce, Naples and Rome Tor Vergata Physics department and INFN Laboratory. Lecce group, to which I belong, tested and certificated 380 units of 23 different typologies. The aim of this thesis is to characterize the RPC detector using the large amount of data acquired during the 18 months of test, describe all tools developed for the ATLAS RPC commissioning and certify the state of "ATLAS Sector 13" during the pre-commissioning test carried out in November-December 2006.

The dissertation is organized in six chapters:

- Chapter 1: **Physics Reach at LHC** contains a short summary of the Standard Model theory and in particular of the Higgs Sector with the possible experimental signature. An introduction of the physics beyond the Standard Model (SUSY) and the other possible physics studies at LHC is given.

- Chapter 2: **The ATLAS experiment at LHC** gives an overview of the Large Hadron Collider machine and an extensive description of the ATLAS experiment with all its subdetector focusing on the physics requirements that have leading the detector design and setup.

- Chapter 3: **The Resistive Plate Chambers in the ATLAS experiment** gives a very detailed description of ATLAS RPC design, and its location in the Muon Spectrometer. Moreover, all electronic chain from the front-end to the DAQ is described according to the muon selection algorithm that define the spectrometer cabling.

- Chapter 4: **ATLAS RPC cosmic ray test facility in Lecce** presents a detailed description of a dedicated facility built in Lecce INFN and Physics Department to test ATLAS RPC. The offline analysis algorithm and the software tools are described. A detailed description of the tests performed on each RPC unit and the Quality Assurance checks performed are given. Finally the results presentation and the results database organization are shown.

- Chapter 5: **Results of ATLAS RPC test in Lecce** gives an extensive detector characterization based on the large amount of data relative at the test performed at Lecce Test Stand. Moreover studies on detector performance as function of temperature an pressure variation are presented. A well defined working point for each ATLAS RPC unit, as a result of statistical analysis is given.

- Chapter 6: **RPC test with cosmic rays on the ATLAS Sector 13** presents the work developed during my presence at CERN Laboratory. In particular the set-up and software tools realized for the ATLAS Muon Spectrometer pre-commissioning. A stand alone software, able to reconstruct cosmic rays with only the RPC hits and its algorithm is presented. Example of checks needed to ensure data quality are given. Results obtained analyzing data collected in November-December 2006 with the detector for the first time in final configuration are presented and explained.

Chapter 1

Physics Reach at LHC

1.1 Introduction

The Electroweak Standard Model is one of the most successful theory of modern physics[1],[2]. It provides a valid detailed framework for the description of Electromagnetic and Weak forces. In fact, it is proved to be valid from microscopic scales of 10^{-16} cm up to cosmological distance of 10^{28} cm.
Nevertheless, one of the most relevant aspect of the theory, called Higgs sector, has not been directly verified, given the fact that the Higgs Boson was never been observed up to now. This has lead to the design of the Large Hadron Collider (LHC), a high-energy and high-luminosity proton-proton collider, under installation and commissioning at the European Laboratory for Nuclear Research (CERN) in Geneva (Switzerland).

1.2 The Standard Model

The Standard Model is a renormalizable theory based on the gauge symmetry group $G = SU(3)_c \bigotimes SU_L^{Weak}(2) \bigotimes SU_Y^{Weak}(1)$ [3], where $SU_c(3)$ is associated to the colour quantum, $SU_L^{Weak}(2)$ to the weak isospin and $SU_Y^{Weak}(1)$ to the hypercharge.

The fundamental constituents of the matter are half-integer spin particles (fermions), which appear in two groups called leptons and quarks, each one three different families . Each family consists of weak isospin doublets in

additions to one or two weak isospin singlets (Tab. 1.1).

lepton	$\begin{pmatrix} e \\ \nu_e \end{pmatrix}_L$ $(e)_R$	$\begin{pmatrix} \mu \\ \nu_\mu \end{pmatrix}_L$ $(\mu)_R$	$\begin{pmatrix} \tau \\ \nu_\tau \end{pmatrix}_L$ $(\tau)_R$
quarks	$\begin{pmatrix} u \\ d \end{pmatrix}_L$ $(u)_R,\ (d)_R,$	$\begin{pmatrix} c \\ s \end{pmatrix}_L$ $(c)_R,\ (s)_R$	$\begin{pmatrix} b \\ t \end{pmatrix}_L$ $(b)_R,\ (t)_R$

Table 1.1: The three fermions families.

The interactions between leptons and quarks are described in terms of integer spin particles exchange (vector bosons), which are the generator of the gauge symmetry group[4] (Tab. 1.2).

	Gauge Bosons	*Scalar Boson*
Before (EW Symmetry Breaking)	$W_{i=1,2,3}$ B $g_{a=1\div8}$ *all massless*	$\phi = \binom{\phi^+}{\phi^0}$
After (EW Symmetry Breaking)	$Z^0, W^\pm$ γ $g_{a=1\div8}$ *massive* *massless*	H

Table 1.2: Scalar and Vector Bosons before and after Symmetry Breaking .

In the Standard Model, in order to give mass to electroweak bosons as required by experiments without spoiling the renormalizability, a complex scalar weak isospin doublet field ϕ was introduced. In fact, imposing to the scalar field a non zero expectation value in the ground state, the electroweak symmetry is spontaneously broken and the weak bosons $W^\pm, Z^0$ acquire mass (Higgs mechanism). In addition, the scalar field is able to generate masses for to the fermions by an 'ad hoc' Yukawa potential term.

1.3 The Electroweak Theory

1.3.1 Introduction

In 1961 Glashow showed that the electromagnetic and the weak interaction are not different forces, but two aspects of the same force: the electroweak interaction. One of the concern was that the theory did not contain the boson masses. The basic problem was to generate weak bosons masses while preserving the renormalizability of the theory. In fact, the insertion of mass terms in the Lagrangian results in an unrenormalizable theory, therefore loosing all the predictive power. The solution to this problem was given in 1967 by Weinberg [1] and in 1968 by Salam [5]. Independently, they applied the Higgs mechanism [6] to the electroweak symmetry group. The Gargamelle Neutrino Collaboration in 1973 observed the first event generated by the Neutral Current Z^0 [7] and ten years later the $W^{\pm}$ and Z^0 bosons were observed at UA1 experiment [8] confirming the proposed theory.
In the GWS model the Lagrangian can be written as a sum of four independent terms:

$$\mathcal{L}^{EW} = \mathcal{L}_{Fermions} + \mathcal{L}_{Gauge} + \mathcal{L}_{Higgs} + \mathcal{L}_{Yukawa}. \tag{1.1}$$

In order to have $\mathcal{L}^{EW}$ invariant under local $SU_L^{Weak}(2) \times SU_Y^{Weak}(1)$ transformations, four gauge fields W_μ^i with i =1,2,3 and B_μ have to be introduced and the standard derivative ∂_μ has to be replaced with the covariant derivative D_μ according to the prescription:

$$D_\mu = \partial_\mu - \frac{i}{2} g_1 Y B_\mu + \frac{i}{2} g_2 \tau_i W_\mu^i \quad , \tag{1.2}$$

where Y and τ_i are the generator of the $U(1)_Y$ and $SU(2)_I$ group respectively, while g_1 and g_2 are the gauge group coupling constants.
The first term of the lagrangian is given by:

$$\mathcal{L}_{Fermions} = i\overline{\psi}\gamma^\mu D_\mu \psi \tag{1.3}$$

and contains massless fermion field ψ and their interactions with the gauge fields, in fact one can see that the basic QED interaction

$$-ie(J^{em})^\mu A_\mu = -ie(\overline{\psi}\gamma^\mu Q\psi)A_{mu} \quad , \tag{1.4}$$

is embedded in the neutral part of the electroweak interaction:

$$-ig_1(J^3)^\mu W_\mu^3 - i\frac{g_2}{2}(j^Y)^\mu B_\mu \quad . \tag{1.5}$$

In order to show that, one has to make a rotation of the two neutral fields by the Weinberg mixing angle Θ_W : and build the fields A_μ and Z_μ

$$A_\mu = B_\mu \cos\Theta_W + W_\mu^3 \sin\Theta_W \tag{1.6}$$

$$Z_\mu = -B_\mu \sin\Theta_W + W_\mu^3 \cos\Theta_W \tag{1.7}$$

Replacing these relations for the physical states A_μ and Z_μ in 1.5, one obtains:

$$-i(g_1 \sin\Theta_W J_\mu^3 + g_2 \cos\Theta_W \frac{j_\mu^Y}{2})A_\mu - i(g_1 \cos\Theta_W J_\mu^3 - g_2 \sin\Theta_W \frac{j_\mu^Y}{2})Z_\mu \tag{1.8}$$

which comparing with 1.4 we get:

$$g_1 \sin\Theta_W = g_2 \cos\Theta_W = e \quad , \tag{1.9}$$

that related the electric charge e with the two coupling constants through the Weinberg mixing angle $\tan\Theta = g_1/g_2$.

The second term:

$$\mathcal{L}_{Gauge} = -\frac{1}{4}W_{\mu\nu}^i W_{\mu\nu}^i - \frac{1}{4}B_{\mu\nu}B_{\mu\nu} \quad , \tag{1.10}$$

written in terms of the field strength tensors

$$W_{\mu\nu}^i = \partial_\nu W_\mu^i - \partial_\mu W_\nu^i - g_2\epsilon^{ijk}W_\mu^j W_\nu^k; \qquad B_{\mu\nu} = \partial_\nu B_\mu - \partial_\mu B_\nu, \tag{1.11}$$

contains the kinetic energy terms of the gauge fields W^i and B and the W^i self-interaction, due to the non-Abelian nature of $SU_L^{Weak}(2)$ group.

Mass terms cannot be contained in $\mathcal{L}_{Gauge}$ and $\mathcal{L}_{Fermions}$, in order to not destroy the gauge invariance under $SU_L^{Weak}(2) \times SU_Y^{Weak}(1)$ local transformations. A new scalar field has to be introduced in analogy with the Higgs mechanism for the superconductivity phenomena(1964), to produce the fermion and bosons masses.
The remaining terms of Lagrangian $\mathcal{L}_{Higgs}$ and $\mathcal{L}_{Yukawa}$, describe the Higgs field kinetic energy, its self-interaction and its interactions with boson and fermion fields.

1.3.2 Generation of Bosons Masses by Electroweak Symmetry Breaking

Up to this point all particles are massless and masses are introduced with the *Higgs mechanism*, that allows the $W_\mu^\pm$ and Z bosons to be massive, while keeping the photon massless to reproduce the known.
Let's consider the Higgs Lagrangian:

$$\mathcal{L}_H = (D_\mu \phi)^\dagger (D^\mu \phi) - V(\phi^\dagger \phi) \quad , \tag{1.12}$$

where ϕ is a $SU_L^{Weak}(2)$ doublet of complex scalar fields:

$$\phi = \begin{pmatrix} \phi^+ \\ \phi^0 \end{pmatrix} = \sqrt{\frac{1}{2}} \begin{pmatrix} \phi_1 + i\phi_2 \\ \phi_3 + i\phi_4 \end{pmatrix} \tag{1.13}$$

and:

$$V(\phi) = \mu^2 \phi^\dagger \phi + \lambda (\phi^\dagger \phi)^2 \quad , \tag{1.14}$$

is a phenomenological potential. The invariance of the Lagrangian under local transformation is manifest.

If $\mu^2 > 0$ the Lagrangian 1.12 describes a system of four scalar particles, each one of mass μ, interacting with four massless gauge bosons. In case $\mu^2 < 0$ and $\lambda > 0$ the potential $V(\phi^\dagger \phi)$ of 1.14 has a minimum at a finite value $\phi^\dagger \phi$ given by:

$$\phi^\dagger \phi \equiv \frac{1}{2}(\phi_1^2 + \phi_2^2 + \phi_3^2 + \phi_4^2) = -\frac{\mu^2}{2\lambda} \quad . \tag{1.15}$$

By choosing a particular minimum, i.e.:

$$\phi_1 = \phi_2 = \phi_4 = 0, \qquad \phi_3^2 = -\frac{\mu^2}{\lambda} \equiv v^2 \tag{1.16}$$

the symmetry, which was manifest in 1.15, has became hidden (*Spontaneous Symmetry Breaking*).
Expanding ϕ above the chosen vacuum state $\phi_0 \equiv \sqrt{\frac{1}{2}}\binom{0}{v}$ we obtain the Higgs physical fields H, according to the formula:

$$\phi = \sqrt{\frac{1}{2}}\begin{pmatrix} 0 \\ v + H \end{pmatrix} \quad . \tag{1.17}$$

After the spontaneous symmetry breaking, only one field H remains, out of the four we started with. The boson masses are obtained from the bilinear terms in the boson fields of eq. 1.12. Using eq. 1.17 we obtain:

$$\begin{aligned} &\mid (ig_1\frac{\tau^i}{2} \cdot W_\mu^i - i\frac{g_2}{2}B_\mu)\phi_0 \mid^2 = \\ &\quad (\frac{1}{2}vg_1)^2 W_\mu^+ W^{-\mu} + \frac{1}{8}v^2(W_\mu^3, B_\mu)\begin{pmatrix} g_1^2 & -g_1g_2 \\ -g_1g_2 & g_2^2 \end{pmatrix}\begin{pmatrix} W^{3\mu} \\ B^\mu \end{pmatrix} \end{aligned} \tag{1.18}$$

where we have introduced the field $W_\mu^\pm = \sqrt{\frac{1}{2}}(W_\mu^1 \mp iW_\mu^2)$ describing the massive charged boson. The first term of eq. 1.18 reproduces the charged boson mass:

$$M_W = \frac{1}{2}vg_1 \quad , \tag{1.19}$$

the second term can be rewritten as:

$$\frac{1}{8}v^2[g_1W_\mu^3 - g_2B_\mu]^2 + 0[g_2W_\mu^3 + g_1B_\mu]^2 \quad , \tag{1.20}$$

in order to reproduce the neutral boson mass, but leaving a massless photon. The physical fields Z_μ and A_μ diagonalise the mass matrix, than eq. 1.20 must be identified with:

$$\frac{1}{2}M_Z^2 Z_\mu^2 + \frac{1}{2}M_A^2 A_\mu^2 \quad . \tag{1.21}$$

Where the normalized fields are given by:

$$Z_\mu = \frac{g_2 W_\mu^3 - g_1 B_\mu}{\sqrt{g_1^2 + g_2^2}}; \qquad M_Z = \frac{1}{2}v\sqrt{g_1^2 + g_2^2} \quad , \tag{1.22}$$

$$A_\mu = \frac{g_2 W_\mu^3 + g_1 B_\mu}{\sqrt{g_1^2 + g_2^2}}; \qquad M_A = 0 \quad . \tag{1.23}$$

After replacing the expression of the Higgs field in the V potential we obtain:

$$V(\phi^\dagger\phi) = -\lambda v^2 H^2 - \lambda v H^3 + \frac{1}{4}H^4 = -\frac{1}{2}M_H H^2 + \cdots \quad , \tag{1.24}$$

where we can deduce the Higgs boson mass:

$$M_H = \sqrt{2\lambda}v \tag{1.25}$$

while the extra terms of the eq. 1.24 describe the Higgs boson self-interaction.

In electroweak theory we have seen that g_1 and g_2 are related with the electromagnetic constant e by the Weinberg angle Θ_W (1.9) and we can easily obtain:

$$\cos\Theta_W = \frac{g_2}{\sqrt{g_1^2 + g_2^2}} \quad e \quad \sin\Theta_W = \frac{g_1}{\sqrt{g_1^2 + g_2^2}} \tag{1.26}$$

therefore one can write the Z mass as function of the W mass and the Weinberg angle:

$$M_Z = \frac{M_W}{\cos\Theta_W} \quad . \tag{1.27}$$

From the Fermi weak interaction theory one obtains:

$$\frac{G_F}{\sqrt{2}} = \left(\frac{g_1^2}{8M_W^2}\right) \quad . \tag{1.28}$$

Combining eqs. 1.19, 1.27 and 1.28 and introducing the fine structure constant $\alpha = \frac{e^2}{4\pi}$, we can rewrite the W and Z masses as a function of known parameters:

$$M_W = \sqrt{\frac{\alpha\pi}{G_F\sqrt{2}}}\frac{1}{\sin\Theta_W} = (78.3^{+2.5}_{-2.3})GeV \tag{1.29}$$

$$M_Z = \sqrt{\frac{\alpha\pi}{G_F\sqrt{2}}}\frac{2}{\sin 2\Theta_W} = (89.0^{+2.1}_{-1.8})GeV \quad . \tag{1.30}$$

At these value one has to add the radiative correction, nevertheless these values are in agreement with the direct experimental measurement.

Fermion masses and coupling

The coupling of the gauge bosons to fermions which preserves gauge symmetry is specified by the covariant derivate eq.1.2. The U(1) charges of the left- and right-handed fermions, Y_L and Y_R are chosen to satisfy the relation $Q = T^3 + \frac{Y}{2}$, so that after symmetry breaking one obtains the correct values of the electric charges, Q. The Higgs field ϕ gives masses to the fermions via Yukawa interactions with the fermions fields. We will not give the explicits form of $\mathcal{L}_Y$ that describes the interactions, but is important to remark that after spontaneous symmetry breaking, a Yukawa interaction of the form $g_f\overline{\psi}_f\psi_f\phi$ leads to a fermion mass, $m_f = g_f v/\sqrt{2}$, and residual $\overline{\psi}_f\psi_f H$ interaction of strength $g_f = \sqrt{2}m_f/v$. The value of the Yukawa coupling required to reproduce the observed masses are shown in table 1.3

Due to the strength coupling a light Higgs boson prefer to decay in couple of heavy quark ($b\overline{b}$), since they are the heaviest fermions state available.

In 1971 G.'t Hooft [9] demonstrated that the Standard Model is a renormalizable theory, in this way Higgs phenomenon allow us to have a physically sensible theory which is also theoretically tractable in high order of perturbation theory.

g_u	2×10^{-5}	g_c	9×10^{-3}	g_t	1
g_d	4×10^{-5}	g_s	8×10^{-4}	g_b	3×10^{-2}
g_e	3×10^{-6}	g_μ	6×10^{-4}	g_τ	1×10^{-2}

Table 1.3: Yukawa coupling constants for quarks and leptons.

1.4 Higgs Bosons Mass Constraints

The Higgs sector is the only sector of the SM which is not yet tested: the only informations about it can be derived from direct searches and indirect constraints. In the last 10-15 years extensive studies has been performed on experimental and theoretical sides, in order to obtain these constraints.
A lower bound on the Higgs boson mass came from the experimental results [10]. Direct searches at LEPII excluded a mass value below 114.1 Gev/c^2 at 95% confidence level [11]. Moreover, a global fit to precision measurements of SM observables presents a χ^2 minimum at $m_H = 85$ GeV and upper bound $m_H < 212$GeV at 95% confidence level (fig. 1.1 *left*) .

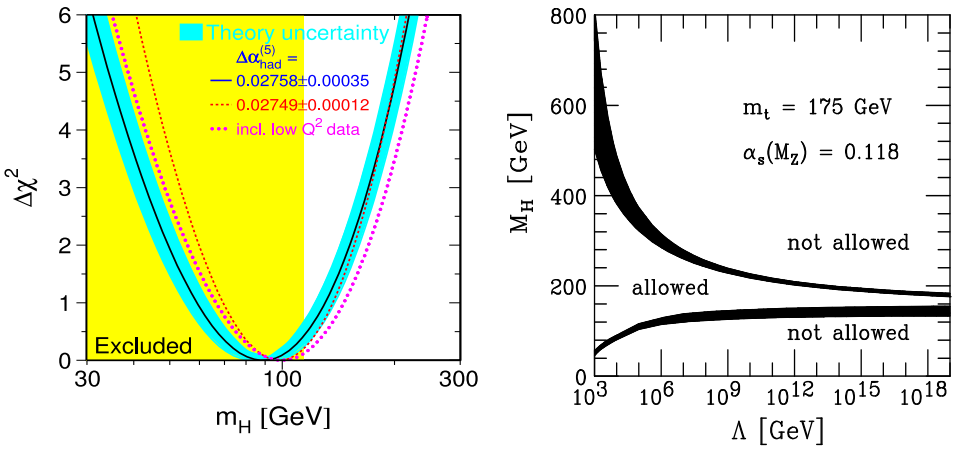

Figure 1.1: χ^2 *of the fit to the SM precision measurements as a function of Higgs mass (left). Theoretical Higgs mass bounds of the electroweak theory (right).*

Upper limit $m_h < 1.2$ TeV comes from the unitarity requirements for the scattering amplitude of longitudinally polarised W bosons, lower limits comes from the vacuum stability and is fixed at 7 GeV/e^2 [12]. From the theoretical point of view, the SM is a consistent theory up to energy Λ only if the Higgs boson mass, is between defined bounds (see fig. 1.1 *right*) [13]. As can be noticed, for a Higgs boson mass between 130 and 180 GeV/e^2 the SM could be valid up to the Planck scale ($M_{pl} \sim 10^{19}$ GeV). On the other hand outside this mass range the SM will break down at a certain scale $\Lambda < M_{Planck}$, where new physics should appear.

1.4.1 Open questions

The Higgs boson has never been observed at the energies actually accessible at particle accelerators even if the SM has been experimentally well confirmed [14].
However, there are several reasons to think that the Standard Model is only an effective description of a more fundamental theory and even that symmetry breaking has a different explanation. For example, it is natural to think that at higher energy scales, all interactions are described by an unique interaction (Great Unification Theory GUT) [4].
In fact, in the SM the colour interaction is not unified with the electroweak interaction, and Gravity is not even included. In addition, there are no explanation for the particle quantum numbers and at least 19 arbitrary parameters are contained in the theory. Finally, the last experimental results confirm the oscillations of neutrino and then more free parameters have to be added to the theory.
The SM also suffers of the so called *hierarchy problem* [15] which arises when there is a fundamental scalar in the theory. In a renormalizable theory, the radiative corrections to the scalar mass, due to the boson and fermion loops, diverge quadratically with the cut-off energy Λ^2. If the cut-off scale corresponds to the Planck energy scale, a fine tuning of 30 orders of magnitude is required to leave m_H under the TeV scale.
One has to remember that the Higgs sector and the spontaneous symmetry breaking were introduced 'ad-hoc' to solve the mass problem and they do not arises naturally from the theory. Several solutions to these problem have been proposed. Among them, Supersymmetry (SUSY)[16][17], a new symmetry between bosons and fermions, offers an elegant solution to the hierarchy problem.

1.5 Supersymmetry

Supersymmetry is a gauge transformation which relates particles which have integer and half-integer spins. For each SM fermion correspond a supersymmetric boson partners, and at each SM boson correspond a supersymmetric fermion partner. SUSY theory is able to give a solution to the hierarchy problem. It implies an equal number of bosons and fermions and these contribute with than opposite sign term in correction loop cancelling any quadratic divergence.
SUSY Boson particles associated to SM fermions have the same name plus an *s* at the beginning (*i.e. selectron, stop, sneutrino*), while SUSY fermion particles associated to SM bosons have the same name plus *ino* at the end (*i.e. gluino, wino, ...*). Supersymmetric partners of known particle are indicated by a tilde over the corresponding particle (*i.e.* $\widetilde{e^-}$). SUSY is an extension of the Lorentz group [18] and its generators are fermions operator Q and $\overline{Q}$ which satisfy the following rules:

$$\left\{Q, \overline{Q}\right\} = -2\gamma_\mu P^\mu \tag{1.31}$$

$$[Q, P^\mu] = \{Q, Q\} = \left\{\overline{Q}, \overline{Q}\right\} = 0 \quad , \tag{1.32}$$

where P^μ is the momentum operator and γ_μ are the Dirac matrices. The supersymmetry generator Q, commutes with the generators of the gauge group $G = SU(3)_c \bigotimes SU_L^{Weak}(2) \bigotimes SU_Y^{Weak}(1)$ gauge group, and relates particles with the same mass and other quantum numbers but differing of $\pm 1/2$ unit of spin. Since SUSY doesn't distinguish between quark/lepton fields and Higgs field, this result in a possible baryon and lepton violation which has not been observed.
In order to avoid it, a new multiplicative quantum number is introduced and assumed to be conserved, the R-parity defined as:

$$R = (-1)^{3B+L+2S} \tag{1.33}$$

where B and L are the baryon and lepton numbers and S is the spin of the particle. Is easy to see that all SM particle have $R = +1$ and all the supersymmetric partners $R = -1$. It is easy to see that if R-parity is

conserved SUSY particles (sparticles) are created in pair and each sparticle must decays in a state containing an odd number of sparticles, while the lightest supersymmetric particle (LSP) is stable. If the LSP is a neutral particle it would be undetectable and could be a good candidate for the explanation of th non barionic dark matter. SUSY is not seem in nature so should be broken otherwise e and $\widetilde{e}$ would have same masses.

1.5.1 The Minimal Supersymmetric Standard Model (MSSM)

The simplest supersymmetrical model is called Minimal Supersymmetric Standard Model (MSSM). It introduces the minimal number of sparticles, one for each SM particle, and the R-parity is conserved. In this model the Supersymmetry is explicitly broken adding to the Lagrangian all possible soft terms consistent with $G = SU(3)_c \bigotimes SU_L^{Weak}(2) \bigotimes SU_Y^{Weak}(1)$ gauge invariance. In this way 105 new free parameters are introduced in the theory.

Electroweak symmetry cannot be broken by hand, but it is necessary to use the Higgs mechanism. In this way we obtain the masses for the quarks, leptons, and $W^{\pm}, Z$ bosons. In the MSSM theory two Higgs doublets are required:H_u and H_d. The fields H_u which couples with the u-types quarks provide their masses while H_d couples with d-type quarks and charged leptons providing their masses. The new Higgs doublets lead to additional massive scalar boson. After electroweak symmetry breaking three of the eight degree of freedom introduced by the two Higgs doublets are removed and five physical remain: two neutral scalar boson H, h, a neutral pseudo scalar boson A and two charged scalar boson $H^{\pm}$. The supersymmetric partners of these five bosons (*Higgsinos*), mix with the winos and binos to form charged and neutral set of mass eigenstates. The two charginos $\widetilde{\chi}_{1,2}^{\pm}$ results from charged Higgsinos and charged wino mixing, and the four uncharged neutralinos $\widetilde{\chi}_{1,2,3,4}^{0}$ result from the two neutral Higgsino neutral wino and bino mixing. Since MSSM have a not barionic particle, in a generic experiment event with production of MSSM will be characterise from large missing transverse momentum. The complete particle content of MSSM is reported in table 1.4 and 1.5.

Names		*Spin 0*	*Spin 1/2*	$SU(3)_c \times SU(2)_L \times U(1)_Y$
squarks, quarks	Q	$(\widetilde{u}_L \quad \widetilde{d}_L)$	$(u_L \quad d_L)$	$(3, 2, \frac{1}{6})$
$(\times 3 families)$	U^c	$\widetilde{u}^*_R$	$u^\dagger_R$	$(\overline{3}, 1, -\frac{2}{3})$
	D^C	$\widetilde{d}^*_R$	$d^\dagger_R$	$(3, 1, \frac{1}{3})$
sleptons, leptons	L	$(\widetilde{\nu}_L \quad \widetilde{e}_L)$	$(\nu \quad e_L)$	$(1, 2, -\frac{1}{2})$
$(\times 3 families)$	E^c	$\widetilde{e}^*_R$	$e^\dagger_R$	$(1, 1, 1)$
Higgs, Higgsinos	H_u	$(H^+_u \quad H^0_u)$	$(\widetilde{H}^+_u \quad \widetilde{H}^0_u)$	$(1, 2, \frac{1}{2})$
	H_d	$(H^0_d H^-_d)$	$(\widetilde{H}^0_d \quad \widetilde{H}^-_d)$	$(1, 2, -\frac{1}{2})$

Table 1.4: Chiral supermultiplets in the MSSM.

Names	*Spin 1/2*	*Spin 1*	$SU(3)_c \times SU(2)_L \times U(1)_Y$
gluino,gluon	$\widetilde{g}$	g	(8,1,0)
wino, W	$\widetilde{W}^\pm, \quad \widetilde{W}^0$	$W^\pm, \quad W^0$	$(1, 3, 0)$
bino, B	$\widetilde{B}^0$	B^0	$(1, 1, 0)$

Table 1.5: Gauge supermultiplets in the MSSM.

1.5.2 GUT and mSUGRA

The $SU_L^{Weak}(2) \times SU_Y^{Weak}(1)$ gauge group is a product of two disconnected sets of gauge transformations. Only if the two interactions can be embed in a larger gauge group we can really unify the electromagnetic and weak force are unify in the electroweak force.

The aim of the grand unified theory (GUT) is to embedded the $SU(3) \times SU(2) \times U(1)$ gauge group in a simple large group, which is spontaneously broken at some high energy scale where only one coupling strength is present.

The coupling strength evolution depends on the particles accessible at that energy. Many GUT theory will be effect by the addition of new particles.

Fig.1.2 [19] show how the introduction of the SUSY partners provide a significant improvement on the existence of unification point, where all the three interaction unify.

If we assume that the SUSY is spontaneously broken and unified with gravity, we are led to supergravity models (SUGRA). If we apply these considerations on the MSSM, we obtain the minimal supergravity model

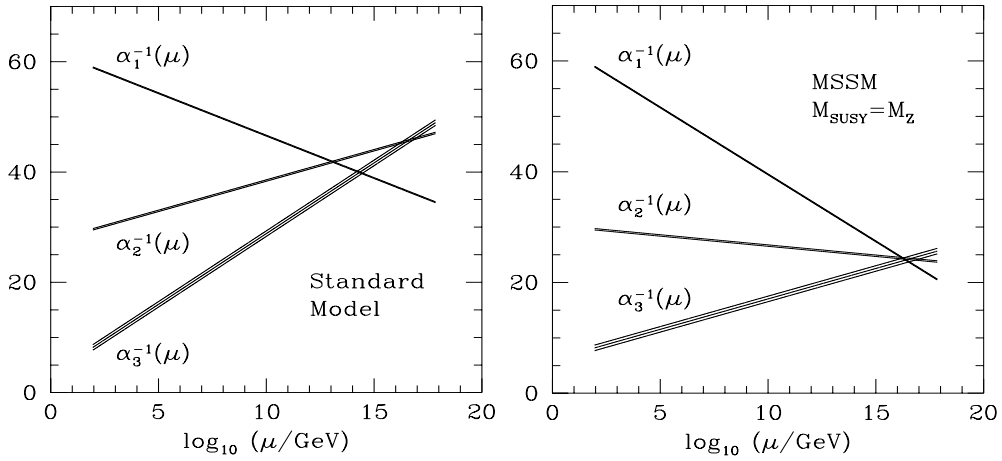

Figure 1.2: *The $SU(3) \times SU(2) \times U(1)$ gauge coupling evolution with energy value, without (left) and with (right) supersymmetry. $\alpha_1 \equiv (5/3)\alpha_Y$, where α_Y is the hypercharge coupling. The bands reflect the actual experimental uncertainties.*

(mSUGRA). In this scenario it is assumed that all the scalars (squarks, sleptons and Higgs bosons) at GUT scale, have a common mass m_0, all gauginos and Higgsinos have a common mass $m_{1/2}$, and all trilinear Higgs-sfermion-sfermion coupling have a common value A_0.
Other two parameters of the theory at GUT scale are the bilinear SUSY breaking term B and the SUSY conserving Higgs mass μ. Usually these two parameters are substituted in favour of $\tan\beta$ and $sgn\mu$. Then only the 5 parameters:

$$m_0, \quad m_{1/2}, \quad A_0, \quad \tan\beta, \quad sgn = \pm 1$$

characterise completely the theory.
The $\widetilde{\chi}_1^0$ in mSUGRA model is the lightest supersymmetric particle. Since it is stable and a neutral particle, it is a good candidate for the nonbarionic dark matter.

1.6 Search for the S.M. Higgs at LHC

Fig. 1.3 shows the cross sections of the standard model Higgs production at LHC as function of the mass and the corresponding Feynman diagrams: gluon-gluon fusion ($gg \rightarrow H$), vector boson fusion ($qq \rightarrow Hqq$), associated vector boson production ($q\overline{q} \rightarrow HW/Z$) and $t\overline{t}/b\overline{b}$ associated production ($gg/qq \rightarrow Ht\overline{t}/b\overline{b}$).
As can be seen, the dominant Higgs production mechanism at LHC will be the gluon fusion process for all accessible Higgs mass.

At the LHC many decay channels (fig.1.4) can be used to look for a SM Higgs boson of a given mass. The most promising channels can be classified in three main categories depending on the expected m_H range:

- ◇ *low mass region* for m_H <130 GeV.
- ◇ *intermediate mass region* for 130< $m_H < 2m_Z$.
- ◇ *high mass region* for $m_H > 2m_Z$.

- ◇ *Low mass region.* In this range of mass Higgs decays to fermion pairs dominate. In particular, the decay $H \rightarrow b\overline{b}$ has the largest branching ratio, being the coupling proportional to the fermion masses and the tag channel closed because of mass. Other decays as $\tau^+\tau^-$, $c\overline{c}$ and gg contribute to the total decay less than 10%[20]. The $H \rightarrow b\overline{b}$ has a quite large cross section (about 20 pb), but since the signal to background ratio is less than 10^{-5}, will be very difficult to detect the Higgs in this way.
  The rare decay mode $H \rightarrow \gamma\gamma$, having a cross section of about 50 fb, due to the more favourable signal to background ratio of about 10^{-3} is instead expected to be one of the golden channel for the discovery of the Higgs. A recent study [21] demonstrates an interesting possibility to detect the channel $H \rightarrow \tau^+\tau^-$ by tagging the vector boson fusion production with one or two forward jets.

- ◇ *Intermediate mass region.* The decay channel $H \rightarrow ZZ^* \rightarrow 4l$ provides a rather clean signature in this mass range. The branching ratio is larger than the $\gamma\gamma$ channel and increases up to $m_H \sim 150$ GeV. In addition to the irreducible background from ZZ^* and $Z\gamma^*$ continuum production, a large reducible background came from $t\overline{t}$

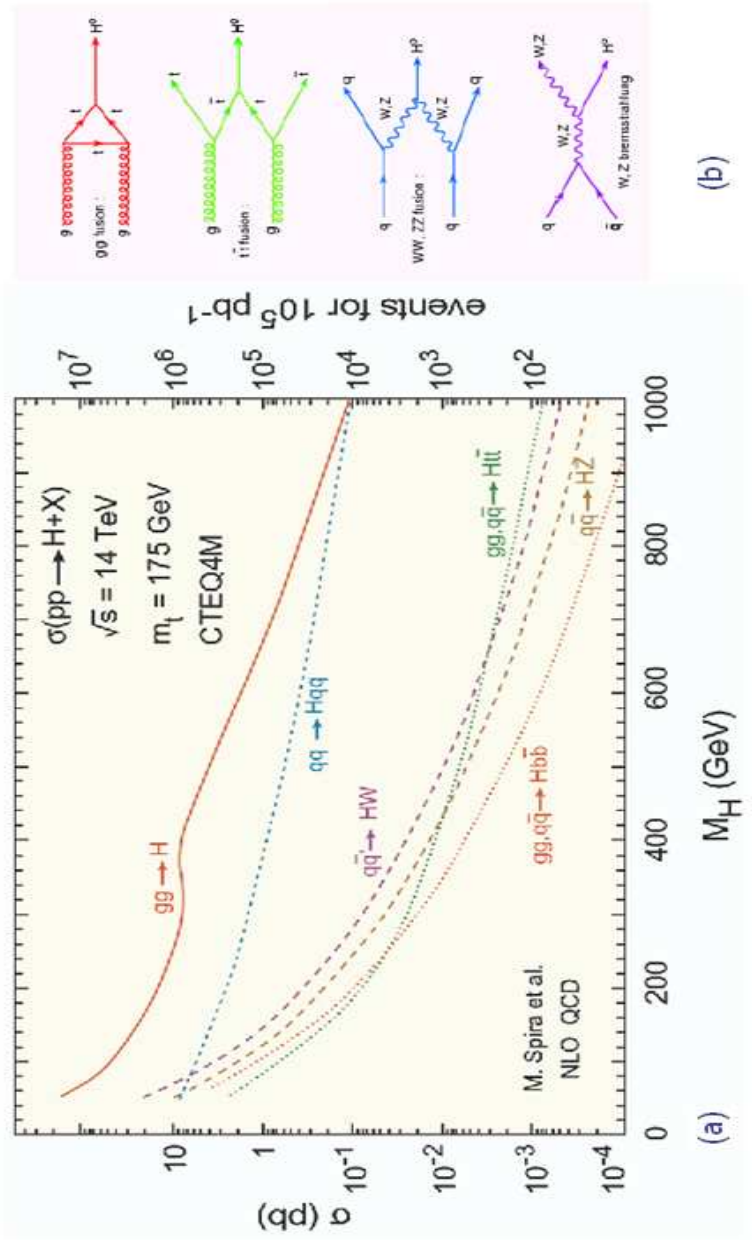

Figure 1.3: *Higgs cross section (a) and related Feynman diagrams (b) for main production processes at LHC.*

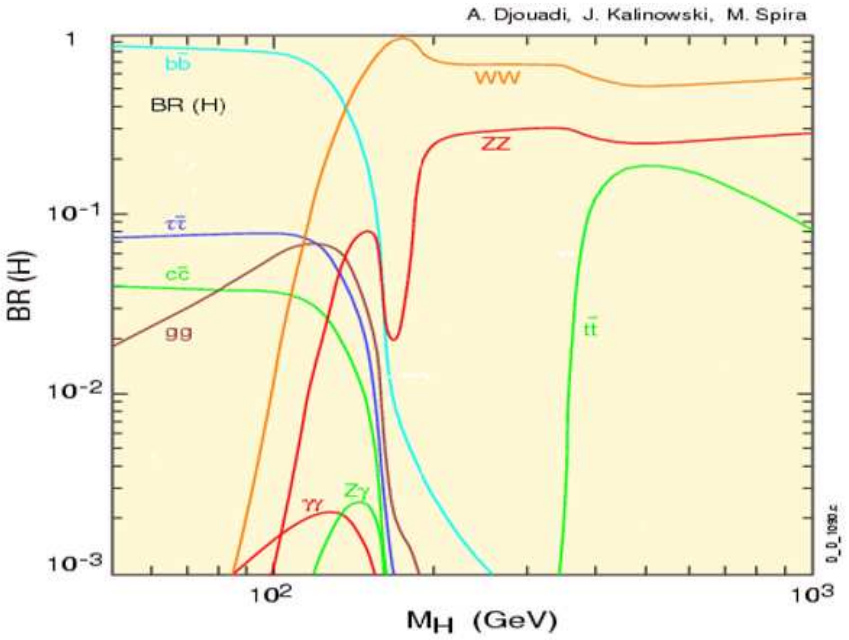

Figure 1.4: *Branching Ratio of Higgs main decays for different Higgs masses.*

and $Zb\overline{b}$. In particular $Zb\overline{b}$ contains a Z in final state, making their rejection more difficult [22]. A pronounced dip in BR curve appear, for $150 < m_H < 180$ GeV, due to the opening of the $H \to WW^{(*)} \to l\nu l\nu$ [23].

- ◇ *High mass region.* With a Higgs mass between $2m_Z < m_H < 600$ GeV the $H \to ZZ \to 4l$ channel is the most reliable channel for the discovery of a SM Higgs boson at LHC. The background is dominated by the continuum production of Z boson pairs, which is expected to be smaller than the signal. The momenta of the leptons in the final state are high and their measurements do not put severe requirements on the detector performance. In this channel the Higgs signal appears as a clear peak in the the four lepton invariant mass on top of the background. To obtain a clean reconstruction, only electrons and muons are required in the final state. In conclusion, the $H \to ZZ \to 4l$ signal should be observed easily above the continuum background with only $10 fb^{-1}$ which is the

luminosity expected in 1^{st} year of running at 10^{33} . Significant rejection of the continuum ZZ background can be achieved by requiring that in the transverse momentum p_t^{max} of the harder Z is larger than a given value $(m_H/3)$.

Fig. 1.5 shows the expected signal in ATLAS experiment from a Higgs boson with $m_H = 300$ GeV and integrated luminosity of $10fb^{-1}$. The signal is shown before and after the p_t^{max} cut is applied and is clearly visible above the ZZ continuum background.

If the Higgs boson mass is larger than 600 GeV other decay channels with large branching ratio must be considered. Three of such a decays are: $H \rightarrow ZZ \rightarrow ll\nu\nu$, $H \rightarrow WW \rightarrow l\nu jj$ and $H \rightarrow ZZ \rightarrow lljj$ respectively with a rate of 6, 150 and 25 times larger than the four-leptons mode. An accurate reconstruction of $W/Z \rightarrow jj$ is required to reject the QCD background. Moreover, for Higgs with very large mass, these channels would be observable only requiring two jets in the forward region $(2 < \eta < 5)$. With this technique a SM Higgs boson could be observed up to 1 TeV[24][25].

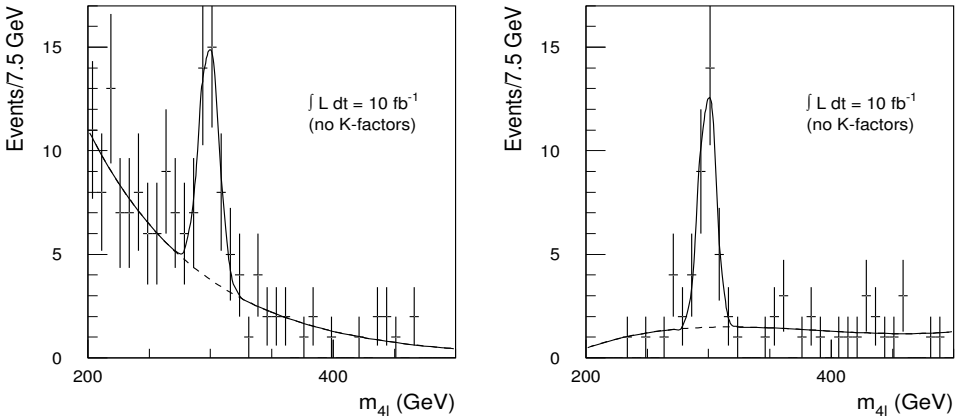

Figure 1.5: *Expected signal of* $H \rightarrow ZZ \rightarrow 4l$ *for* $m_H = 300$ *and integrated luminosity of* $10fb^{-1}$ *for the ATLAS experiment before (left plot) and after (right plot) cut with* $p_t^{max} = m_H/3$.

1.6.1 Search for the MSSM Higgs

As we said in section 1.5.1 the MSSM contains two charged Higgs bosons ($H^{\pm}$), and three neutral states (h, H, A). Masses and couplings can be expressed as a function of only two parameters: m_A and $\tan\beta$ which is the ratio between the Vacuum Expectation Value v_u/v_d of the MSSM Higgs doublets. Different decay modes will be accessible. In particular, the most interesting ones are the SM-like decays $h \to \gamma\gamma$, $h \to b\bar{b}$, $H \to ZZ \to 4l$ and the ones favourite by large $\tan\beta$ values $H/A \to \tau\tau$, $H/A \to \mu\mu$. The decay widths of MSSM Higgs bosons are strongly dependent on the value of m_A and $\tan\beta$. At the LHC the region of parameter space $m_A = 50 - 500$ GeV and $\tan\beta = 1 - 50$ could been investigated. In general, good photon/lepton identification and E_T^{miss} are required in order to perform MSSM Higgs search. Other interesting channels to discover a heavy MSSM Higgs are: $b\bar{b}H/A$ associated production with subsequent decays $H/A \to b\bar{b}$ and $H \to hh \to b\bar{b}b\bar{b}$. The main problem for these decay channels is the high background level, that leads to impose very high threshold on energy jets, with consequently loss of acceptance.

1.7 Other physics measurements at LHC

The main goal of the LHC and his experiments will be to led up the Higgs field nature and to give an answer to the electroweak spontaneous symmetry breaking. Nevertheless, the high energy and high luminosity of the LHC offer the possibility to perform precise measurements on known heavy particles. In next subsection we want to put our attention on W and top mass measurements, and heavy flavour physics.

W mass

From measurements performed at LEP and Tevatron colliders, the W mass is known with a precision of about 29 MeV [20]. The W mass is related to other parameters of SM through the subsequent relation:

$$M_W = \sqrt{\frac{\alpha\pi}{G_F\sqrt{2}}}\frac{1}{\sin\Theta_W\sqrt{(1-\Delta R)}} \tag{1.34}$$

where ΔR takes in to account the radiative corrections, which depends quadratically on top mass ($\sim m_{top}^2$) and logarithmically on the Higgs

mass ($\sim log(m_H)$). Precise measurements of W and top mass can constrain the mass of the SM Higgs. The precision on the top mass and on the W mass could be related by the following expression:

$$\delta M_w \simeq 0.7 \times 10^{-2} \delta m_{top} \quad , \tag{1.35}$$

in order to give a comparable error in the Higgs mass estimation. Since the top mass will be measured with a precision of about 2 GeV at LHC, the W mass should be known with a precision of 15 MeV or better. Due to the large sample of W's produced at LHC the statistical uncertainty will be smaller than 2 MeV. The main contribution to the uncertainty will be due to absolute momentum scale knowledge and to the momentum resolution. Combining measurements of two high-p_t LHC experiments should ensure the knowledge of a W mass with precision better than 20 MeV.

Top-physics

Ten years after the top quark discovery at the Tevatron collider, due to the limited statistic, we still know quite little about top production and decay mechanism. LHC will be a top factory, with a cross section for $t\overline{t}$ pairs and single tops roughly 100 times larger than Tevatron. As a consequence, statistical uncertainties will be negligible and the measurements will be dominated by systematic uncertainties. Using semileptonic, dileptonic and all-hadronic $t\overline{t}$ final states, from $t \to Wb$ decays, a total error on top mass below 2 GeV should be feasible. It could be possible to achieve an ultimate precision of about 1 GeV combining measurements of two high-p_t LHC experiments.
The high statistic available at LHC will also allow to study many properties of the top quark, beside its mass. For example, top quark spin properties could be studied through the W polarisation and the $t\overline{t}$ spin correlation and single top production.
Direct searches for new physics are also possible. In the SM a $t\overline{t}$ resonance is not allowed, but heavy resonance decaying to $t\overline{t}$ might produce a peak in the $t\overline{t}$ invariant mass spectrum, as predicted by various model beyond the SM. In addition, many models beyond the SM, with a complicated Higgs sector, have implications for top decays. For example, top decay to a light charged Higgs boson $t \to H^+b$ could

be searched through an excess of $t\bar{t}$ with τ-jets or a deficit of dilepton events.

B-physics

Due to the large hadronic cross section, at LHC the rate of B hadron production will be very high. During the first year of operation of LHC, about 2.3×10^{10} $b\overline{b}$ pair will be produced. This will allow high precision measurements in the b-physics sector. Precision measurements of B-hadron decays that over-constrain the CKM matrix elements, could give indirect evidence of new physics beyond the Standard model. The golden channels to perform this study will be the CP violating decays $B_d^0 \to J/\Psi K_s^0$ and $B_d^0 \to \pi^+\pi^-$.
Moreover, other measurements of CP violation will be performed on $B_d^0 \to J/\Psi\phi$ and on $B_d^0 \to D^0 K^{*0}$ decays.
The oscillations in $B_d^0 - \overline{B}_d^0$ system, have been directly observed and measured [26], $\Delta M_d = 0.505 \pm 0.005 ps^{-1}$. In $B_s^0 - \overline{B}_s^0$ system, oscillation have been observed in $B_s^0 \to D_s^- \pi^+$ and $B_s^0 \to D_s^- - \pi^+\pi^-\pi^+$ channels, $\Delta M_s = 17.3^{+0.33}_{-0.18}(stat.) \pm 0.07(syst.) ps^{-1}$ but only at 95% of CL. Measurements at LHC can improve these results.
Some possible B decay like $B_{d,s} \to \mu\mu(X)$ are strongly suppressed in a SM, typical branching ratio for these decay are in the range $10^{-5} - 10^{-10}$, these decay are forbidden in the at tree level in SM. Since SM predict very low branching ratio, an enhancements of these decay could be an effect of a new physics beyond the Standard Model.

Chapter 2

ATLAS experiment at LHC

2.1 Introduction

There are hints that new physics could be discovered at energies around 1 TeV . Search for this new physics, is one of the goal of the the Large Hadron Collider (LHC)[27][28]. This machine is accommodated in the existing 27-kilometers LEP tunnel at CERN and will use the most advanced superconducting magnet and accelerator technologies ever employed. It will collide proton beams with energies of 7+7 TeV at a design luminosity of $10^{34}m^{-2}s^{-1}$, providing the experiments with high interaction rates. It will also collide beams of heavy ions such as Pb with a total collision energy in excess of 1,250 TeV, about thirty times higher than the Relativistic Heavy Ion Collider (RHIC) at Brookhaven (USA).

2.2 CERN Accelerator System and LHC

A complex system of accelerators will be used, to allow to the proton beams to reach the final energy of 7 TeV. The new accelerator machine, will use the former accelerator system operating at CERN. LHC will be supplied with protons from the injector chain Linac2 - Proton Synchrotron Booster (PSB) - Proton Synchrotron (PS) - Super Proton Synchrotron (SPS) as shown in fig.2.1. All these machines have been upgraded to meet the LHC demands. The energy of the Proton Synchrotron Booster has been increased from 1 GeV to 1.4 GeV. The beam brightness (intensity/emittance) of the PS machine is now almost twice the previous, and provide beams of 26 GE.

The SPS is the last step before LHC, beams are accelerated from 26 GeV to 450 GeV before extraction via two specially transfer line connecting the SPS and the LHC ring tunnel. During the years, many changes have been brought to the original plan, mainly due to the decision to close the CERN west experimental area, the modifications of proton bunch patterns and the approval of the *Cern Neutrino to Gran Sasso* (CNGS) facility, which share the new SPS east extraction channel with LHC ring. To transport the protons beam at 450 GeV/c and the ions beams from the SPS to the LHC two new transfer lines have been built with a total length of 5.6 Km.

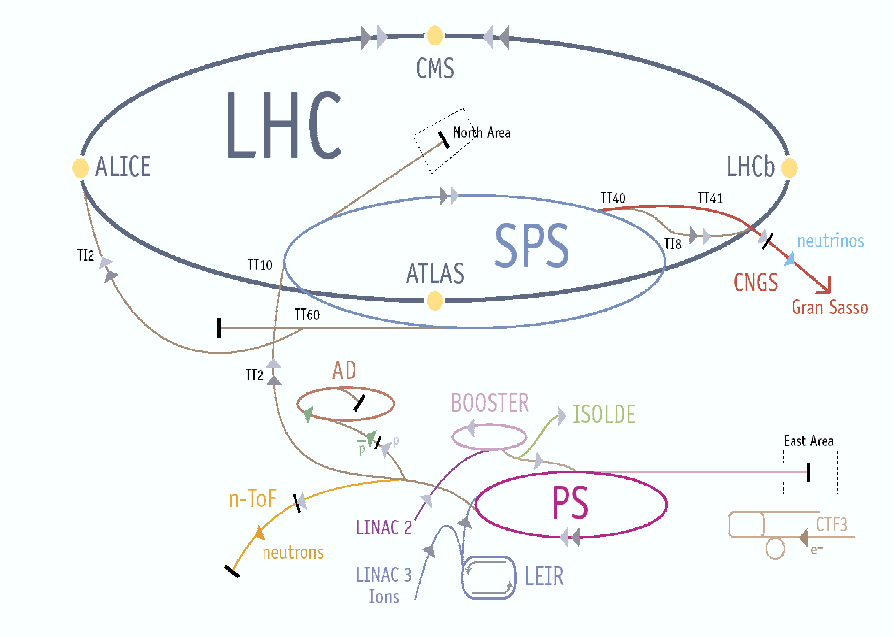

Figure 2.1: *CERN accelerator system.*

The LHC machine comprises 1232 main dipole magnets and 392 main quadrupole magnets, which allow to keep protons beams at 7 TeV in two adjacent beam cavity. Superfluid helium cooling will provide the operational temperature of $1.9°K$ necessary to the superconductive magnet dipole to generate a B field strengths of 8.4T necessary to bending the proton beams. Beams collide in four interaction point at nominal CM energy of 14 TeV. The number of events interaction/second generated in the LHC at an interaction

point (IP) is given by:

$$N_{interaction} = L\sigma_{total} \tag{2.1}$$

where σ is the total cross section and L the luminosity at the collision point. The luminosity depends only on the beam parameters and can be written for a Gaussian beam distribution as:

$$L = \frac{N_b^2 n_b f_{rev} \gamma_r}{4\pi\epsilon_n \beta^\star} F \tag{2.2}$$

where N_b is the number of particle per bunch, n_b the number of bunches per beam, f_{rev} the revolution frequency, γ_r the relativistic gamma factor, ϵ_n the normalized transverse beam emittance, $\beta^\star$ the beta function at the collision point and F the geometric luminosity reduction function, due to the crossing angle at the Interaction Point (IP).
In table 2.1 the LHC accelerator and beam parameters are listed [29].

LHC is planned to have the first pilot run in the spring of 2008 [30]. In this phase 43 single bunch of protons will be transferred from PS to LHC via SPS. With 43 bunches for beam there will be no parasitic crossing and in order to provide collision in LHCb IP bunches will be displaced by 75 ns [31]. In 2008 and for the next three years, operation will be at 75 ns and subsequently at 25 ns bunch spacing. In the 75 ns mode, each beam will contain 936 bunches instead of 2808 of final configuration. In the first run period the total current stored in a beam cannot exceed half the nominal value, this will limit the initial luminosity to $\mathcal{L} = 2 \times 10^{33} cm^{-2} s^{-1}$ until the 2010 run, when the accelerator machine will reach the final luminosity of $\mathcal{L} = 1 \times 10^{34} cm^{-2} s^{-1}$.

2.3 ATLAS general overview

In the LHC interaction point number one there will be placed ATLAS (**A** **T**oroidal **L**HC **A**pparatu**S**) one of the six experiments approved for data taking at the LHC. It is a general purpose detector, which takes advantage of the most modern techniques of particle detection, implemented in its different subdetectors. Its main scope is to find the origin of the symmetry breaking in the SM (Higgs) or eventually the equivalent mechanism in a more complex theory. To absolve to this aim, large sensitivity on a very wide range of

Accelerator length	26.66 Km
Beam energy	7 TeV
Luminosity	$10^{34}\ cm^{-2}s^{-1}$
Dipole field	8.56 T
Total beam current	0.584 A
Beam revolution frequency f	11.246 kHz
Distance between bunch	7.48 m
Bunch separation	25 ns
β function at I.P.	0.5 m
Number of protons for bunch	$1.15 \cdot 10^{11}$
Number of bunch	2808
Crossing angle at I.P.	200 μrad
Luminosity lifetime	14.9 h
Beam lifetime	22 h
Energy loss per turn	6.9 KeV
Radiated power per beam	3.7 kW
Stored energy per beam	362 MJ
Maximum transverse beam emittance	$\epsilon_n = 3.75 \mu m$
R.M.S. beam with σ	15 μm
R.M.S. beam length σ	75 μm

Table 2.1: LHC accelerator and beam parameters

energy is demanded, imposing tightening requisite on each subdetector.
A three dimensional view of the ATLAS detector is shown in fig.2.2.
The detector is cylindrical, having a total length of 42 m an a radius of 11m. Mechanically it is divided in to three sections, the *barrel* in the central region and two *end-cap* at either end of the barrel. The detector is realized with a tracker-calorimeter-muon chamber onion skin configuration, all subsystem will be described in more detail in the following paragraph. The layout of the apparatus is characterized by the muon spectrometer magnet system, which define the detector size.

Spherical coordinate system is defined in terms of the z direction (beam axis), polar angle, measured from this axis (θ) and azimuthal angle (ϕ). The $x - y$ plane is the plane transverse to the beam direction, which divides the detector in three section side A and C for $z > 0$ or $z < 0$ and side B for

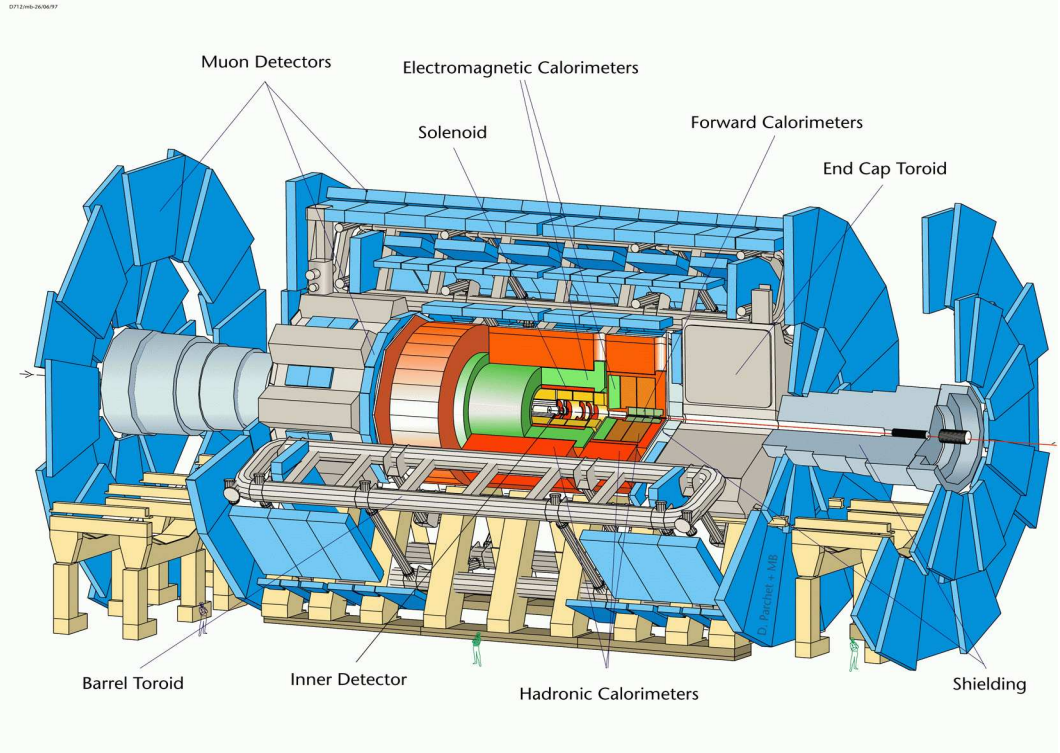

Figure 2.2: *ATLAS detector and its subsystems.*

$z = 0$.
Another important variable to be considered is, the pseudorapidity η defined as:

$$\eta = -ln\left(tan\frac{\theta}{2}\right) \tag{2.3}$$

which is zero at $\theta = 90^0$ while going to infinite as θ goes to zero. The pseudorapidity has two qualities which make it particularly useful for an high energy physic detector:

- It is Lorentz invariant.
- The production of particles is distributed almost uniformly in the pseudorapidity.

2.3.1 Magnet System

The aim of magnet system in the ATLAS experiment is to provides the measurements of the charged particle momentum. In order to minimize the multiple scattering of the muon product in particle decay, the muon detector system is located in air, surrounded by a toroidal magnet system. It is made of a Central Solenoid (CS), an air-core Barrel Toroid (BT) and two air-core End-Cap Toroids (ECT)[32].
The CS is positioned in front of the electromagnetic calorimeter and provides the bending for the Inner Tracker momentum measurement. It has a length of 5.3 m, an internal radius of 1.2 m and provides at the operating current of the CS is 7.6kA a nominal magnetic field of 2 T with a peak of 2.6 T at the superconductor windings.
The CS is hosted in the vacuum vessel of the electromagnetic calorimeter to avoid degradation of electrons and gammas energy measurement [33].
The Barrel Toroid consists of eight flat coils assembled radially and symmetrically around the beam axis. The BT winding that provide to generate the magnet force are built up with 20.5 kA aluminium stabilized NbTi superconductor. Each coil is contained in a different cryostat, where the only openings are due to the electrical and cryogenic lines, that allow to test each single toroid before the final installation [34]. The overall dimensions of the Magnet System are determined by the BT that extends over a length of 26 m in length, and an outer diameter of 20 m.
The magnet system is completed by two End-Cap Toroid (ECT) insert at the end of BT and lined up with the CS. Like the BT each of the ECT is made of 8 coils rotated by $22,5^0$ with respect to the BT coils to realize a radial overlap and to optimize the particle bending in the two system transition regions. Each ECT is made of the same technology and material as the BT but the 8 coils are located in one large cryostat, that have a length of 5 m, an outer diameter of 10,7 m and an inner bore of 1,65 m, where the beam pipe is hosted. Central Solenoid BT and ECT system are cooled at 4.5^0K by forced flow of helium. The magnet field integral characterize the bending power of the muon spectrometer region depends on the pseudorapidity. The BT provides 2-6 Tm for $|\eta < 1.3|$ while the ECT provides 4-8 Tm at $1,6 < |\eta| < 2,7$. The bending power is lower in the transition region.

2.3.2 Inner Detector

The scope of the ATLAS Inner Detector (ID), is to provide as many signature as possible, in the high-rate environment like at the LHC accelerator, the detector have to assure good performance at highest possible luminosity which could be delivered by the LHC. In order to meet these requirements a complex tracker system based on three different technologies, Silicon Pixel, Silicon Strips and Straw Tube Tracker (TRT), has been developed [35].
The Silicon Pixel system detector consist of three coaxial layer in the barrel region and four end-cap disks on each side for a total of 140 million detector elements arranged in about 2500 identical modules. The pixel technology resolve automatically all space ambiguities, and the fine segmentation ($50\mu m$ in $R\phi$ plane and $300\mu m$ in z) provide three high precision point for the pattern recognition near the interaction point, fundamental to reconstruct the primary and secondary vertex of short-lived particles. Of primary importance is the radiation hardness of the detector which has to support the damage due to the $500 fb^{-1}$ that the LHC experiment have to collect during the 10 years of data taking.
The silicon tracker system is completed by the Silicon Strips (SCT). It is made by four layer in the barrel region and nine wheels for each end cap. Each strip is $80\mu m$ wide and $6,40cm$ long, 768 strips are arranged in a silicon detector, four detectors realize a module. The total surface of the (SCT) is about $61m^2$, it guarantee an spatial resolution of $16\mu m$ in $R\phi$ and $580\mu m$ in z and allow to distinguish tracks separated by $200\mu m$. The SCT layout is optimized to ensure at least four precision measurements for each track.
Due to the high cost, and the necessity to not introduce a large amount of material in front of the electromagnetic calorimeter the silicon detector have to be limited in number and radiation length. The TRT can provide instead a large number of track points with a good precision at relative low cost and low radiation length. It is based on 4mm tubes with a sense wire filled with xenon-based gas mixture. The TRT can detect the transition radiation that occur when a relativistic particle traverse two different material. Setting an appropriate threshold it can discriminate on the particle velocity allowing electron/pion rejection. The TRT are parallel to the beam pipe in barrel region and arranged in 16 disks at the end-cap region for a total of 420000 read out channels providing about 36 hit for tracks. Each straw tube has a resolution of $170\mu m$. The trt system can reach $50\mu m$ including errors from alignments.

The entire dimension of the ID are : 7 metres in length with 115 cm of radius, and are defined by the dimension of the electromagnetic calorimeter cryostat. All tracks with $|\eta < 2.5|$ are measured with at least seven high precision point and about 36 straws. Fig.2.3 shows the average number of hit per tracks for each technology.

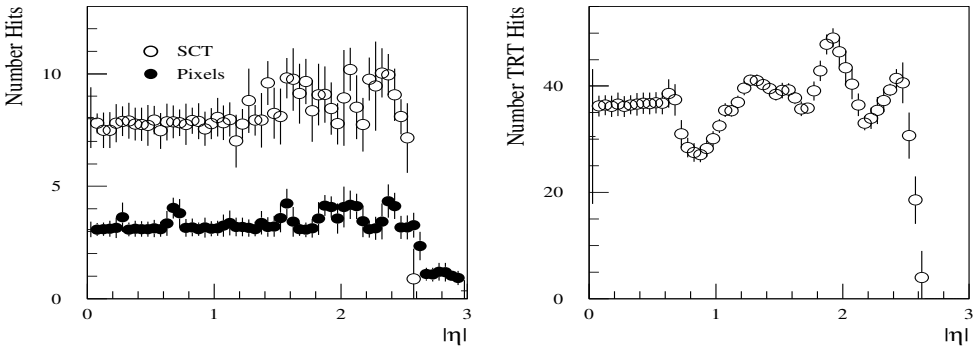

Figure 2.3: *Number of hits in the ID per tracks as function of η.*

The momentum resolution is also limited by the magnetic field because the coils of the CS do not cover the cryostat for all the ID length but only for 5.3 m. The magnetic field degrades at the end of the ID, nevertheless all studies demonstrate that it ensures a good momentum resolution and charge sign identification. Fig.2.4 show the magnetic field along z and R.

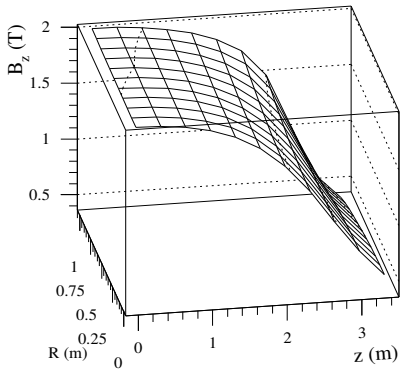

Figure 2.4: *B Field in Inner Tracker System as function of η and R.*

2.3.3 The Calorimeter System

The ATLAS calorimeters will play a leading role in the reconstruction of the most important physics channels. At an hadron collider are of primary importance the accurate measurements of energy and position of electromagnetic and hadronic shower, particle identification, and an high hermetic design to allow measurements of missing transverse energy. The Calorimeter System is composed by an Electromagnetic Calorimeter, a Hadronic Calorimeter and a Forward Calorimeter. Fig. 2.5 shows a schematic view of the system.

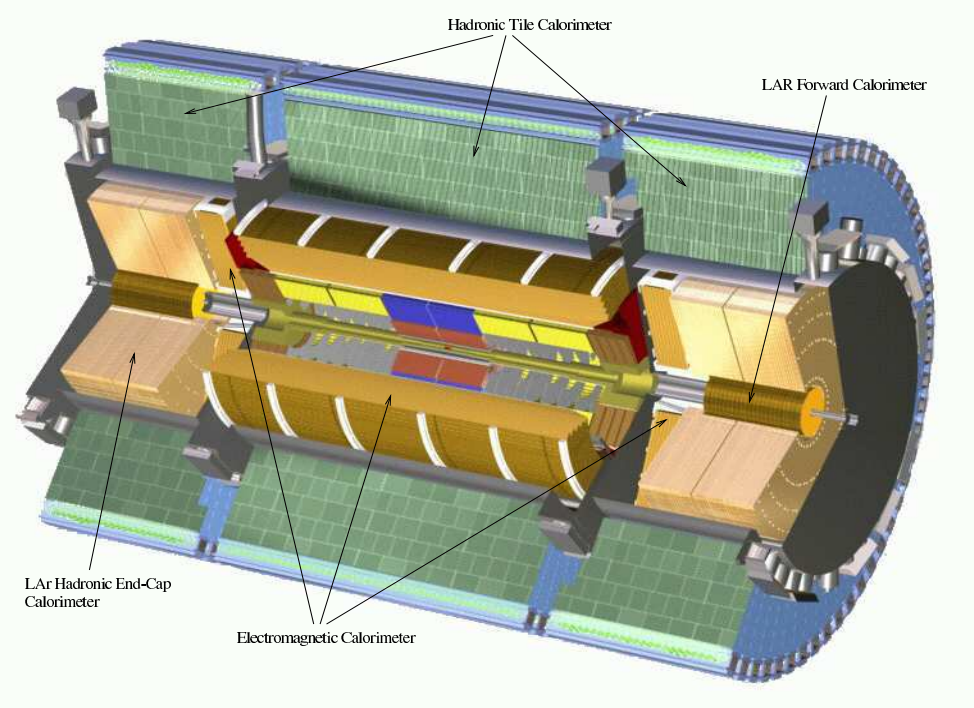

Figure 2.5: *ATLAS Calorimeter System.*

- **Electromagnetic Calorimeter**

  To satisfy the very tight physics requirements for an electromagnetic calorimeter the ATLAS collaboration has chosen a sampling lead-liquid argon calorimeter, with the absorbers bent in accordion shape [36], [37].

It has to satisfy at the subsequent physical requests:

- Largest possible acceptance to increase the significance of $H \rightarrow \gamma\gamma$ and $H \rightarrow 4e$.
- Electron reconstruction from 1-2 GeV up to 5 TeV to reconstruct electron from semileptonic b-decay and from $Z^{'}$ or $W^{'}$ decays.
- Excellent energy resolution in a wide range (10-300 GeV).
- 24 radiation length at $\eta = 0$ to give limited leakage for energy showers.
- Excellent separation for photon/jet, electron/jet and τ/jet.
- High granularity and an energy-scale precision of 0.1% to assure a good mass recostruction for $H \rightarrow \gamma\gamma$ and to allow specific SUSY studies.

The ECAL span, in pseudorapidity $|\eta < 3.2|$ and it is divided in two half-barrel separate by 6 mm gap, and two end-cap (EMEC) each constituted by two coaxial wheels. The accordion geometry provide the perfect uniformity along ϕ direction. At $|\eta < 1.8|$ the ECAL is preceded by a presampler used to correct the measurement for the energy loss in the ID material. In barrel region the liquid-argon gap has constant thickness of 2.1 mm and the absorber are shaped as function of η, instead in the endcap, the thickness of the lead is constant and the amplitude of the gap is variable. To assure high granularity, along ϕ the ECAL three sampling in depth are implemented. The first sampling, is made of strips of $\Delta\eta \times \Delta\phi = 0.003 \times 0.1$ size for $\sim 6X_0$ of depth. Strips have been introduced to improve the π^0 and jet rejection and to allow, with the second sampling, the measurement of the electromagnetic shower direction. In second sampling the granularity is $\Delta\eta \times \Delta\phi = 0.025 \times 0.025$, due to Moliere radius of the calorimeter for a depth of $16X_0$ and in the last sampling it becomes $\Delta\eta \times \Delta\phi = 0.1 \times 0.0982$ for a depth of $2X_0$. Many tests, on energy resolution, energy reconstruction and response uniformity, have been carried out on different ECAL module on electron beams. Energy scan have been performed at several position and the energy resolution has been extracted using the function:

$$\frac{\sigma_E}{E} = \frac{a}{\sqrt{E(GeV)}} \oplus b \tag{2.4}$$

where a is the stochastic term and b is the constant term, results are shows in fig.2.6.

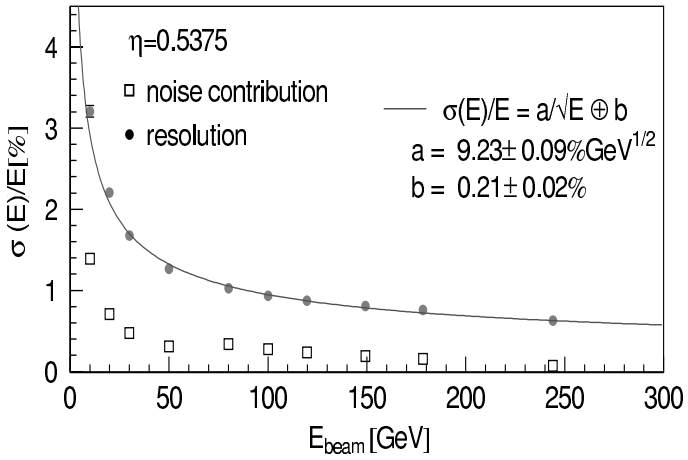

Figure 2.6: *Energy response results of a barrel ATLAS ECAL module [38].*

Extensive tests have been performed to estimate the global constant term, which take in to account the possible difference module by module. The results are satisfactory, all parameters match the design expectations. In particular a stochastic term better than $10\%\sqrt{E(GeV)}$ and a constant term at level of 0.7% have been achieved[38].

- **Hadronic Calorimeter** The main scopes of the hadronic calorimeter are the following:
  - Jets identification, energy and direction measurements .
  - Good hermiticity to measure missing transverse energy.
  - Good energy resolution and linearity in response over the whole η range, to enhance the particle identification capability of the electromagnetic calorimeter.($\frac{\sigma_E}{E} = \frac{50\%}{\sqrt{E(GeV)}} \oplus 3\%$).

  ATLAS collaboration has chosen for the barrel region a Tile Calorimeter solution [39] and for the end-cap a Liquid-Argon sampling

calorimeter [36].
The Tile Calorimeter is designed as one barrel and two extended barrel, separated by a crack region of about 600 mm, in order to allow the passage of the ID and ECAL cables. It consists of a cylindrical structure with a inner radius of 2280 mm and an outer radius of 4230 mm. The barrel part is 5640 mm in length ($|\eta < 1|$), while each of the extended barrel is 2910 mm long ($1 < |\eta| < 1.7$). The Tile Cal use iron (passive material), plastic scintillator (active material) and wavelength shifting fibers connected to PMTs for the read-out. The total thickness $\sim 10\lambda_0$ is enough to ensure no shower leakage towards the muon spectrometer. ATLAS has chosen for its Hadronic End-Cap Calorimeter (HEC) the copper-liquid argon sampling technique with flat plate geometry and GaAs preamplifiers in the argon. It shares the two end-cap cryostat with the EMEC and forward calorimeter (FCAL). The HEC is structured in two wheels, each with external diameter of about 4m. The length of the first is 0.82 m and use copper absorber plate with thickness of 25 mm, instead the second one is length 0.96 m with thickness of 50 mm. Each wheel is made out of 32 identical modules. The are 40 gaps and each end-cap, 24 (16) in the first (second)wheel, with a thickness of 1.85mm filled by liquid-argon. The granularity is $\Delta\eta \times \Delta\phi = 0.1 \times 0.1$ for $|\eta| < 2.5$ and $\Delta\eta \times \Delta\phi = 0.2 \times 0.2$for $2.5 < |\eta| < 3.2$. The energy resolution as a function of the energy has been measured in many test beams, A fit to the data with $\frac{\sigma_E}{E} = \frac{a}{\sqrt{E}} \oplus b$ yields for the sampling term $(84.1 \pm 0.3)\%\sqrt{GeV}$ and for the constant term zero within errors[40].

- **Forward Calorimeter**

  The Forward Calorimeter (FCAL) is designed to work in the range $3.1 < \eta < 4.9$, very close to the beam pipe. Therefore it has to cope a region with a high level of radiation. In a limited space it has to guarantee about 9.5 interaction lengths to avoid spilling out of energy from the forward calorimeter to muon spectrometer. For this reason it consist of three sections, the first made of copper and the other two made of tungsten. Each section consist of a metal matrix realized with a concentric tube and road that realize a small gap filled with liquid argon. The choice to use tungsten like absorber material make its implementation challenging for the difficulty in assembly that this material present. In terms of electronics and readout, the rods are

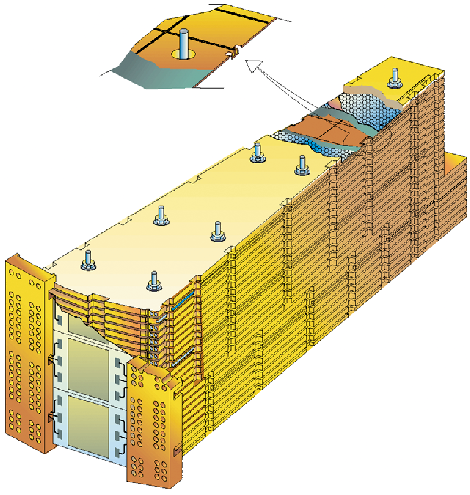

Figure 2.7: *Artistic view of a module of HCAL with cutaway showing the read-out structure.*

linked by 4 on detector and the signal is carried out by polyimide insulated coaxial cables. The total number of channel for both end-cap is 11.288.

2.3.4 Muon Spectrometer

The presence of high momentum muons in the final state, as for $H \rightarrow 4\mu$ is one of the most promising signatures for interesting events. The requirements of high quality measurements for muons has characterized significantly the design of the ATLAS detector [41].

The ATLAS muon spectrometer is designed to meet the following requirements:

- **Operation**: it have to operate reliably for many years in a high rate and high background environment. This affects the operating point and the detector response. In particular due to possible detector aging performance degradation can arise;

- **Precision**: the measurement accuracy must be commensurate with the physics requirements. The large air-core toroidal magnet system configuration and the muon chamber design provide three high

precision track segment over a large volume in a moderate magnetic field, which allows a precision momentum determination;

- **Standalone Apparatus**: the muon spectrometer, in principle, has to be able to perform physical measurement without other subdetector as an example the Higgs discovery in the golden channel $H \rightarrow \mu\mu$;
- **Realization**: muon chamber production took a long time period and involved many different institutes. Due to the long time operation robust technology suitable to mass production was required and continuous quality assurance was needed.

ATLAS Muon Spectrometer Geometry

The ATLAS Muon Spectrometer is a very large apparatus and its geometry is quite complex, it is organized in 16 sector associated with the eight coils of the toroidal magnets. Natural symmetries are broken by the feet structures supporting the detectors and the apertures for access and services such as cables and cryogenics pipe line. To cover the large surface of barrel and endcap region, four technologies of gaseous detector are used. Monitored Drift Tubes chambers (MDT) and Cathode Strips Chambers (CSC) provide precision coordinate measurement in the bending plane, while Resistive Plate Chambers (RPC) and Thin Gap Chambers (TGC) provide the second coordinate measurement and most important they generate the trigger signal in barrel and end-cap region in both coordinate. providing the second coordinate measure. In Tab.2.2 summarizes the number of chambers instrumentation.

	PrecisionChambers		*TriggerChambers*	
	CSC	*MDT*	*RPC*	*TGC*
Number of chambers	32	1194	596	192
Number of readout channels	67000	370000	355000	440000
Area Covered (m^2)	27	5500	3650	2900

Table 2.2: *ATLAS chambers instrumentation.*

To ensure a good hermeticity large number of chamber which differ in size are built. The layout is designed to provide three point of precision in the

bending plane and trigger measurements. In the barrel ($|\eta| < 1$) they are be arranged in three concentric cylinders with the beam axis at radii of about 5 m, 7.5 m and 10 m. Particles trajectories are measured near the inner and outer field boundaries, and inside the field volume, in order to determine the particles momentum from the sagitta generated by the magnetic field. The end-cap chambers will cover the pseudo-rapidity range $1 < |\eta| < 2.7$ and are arranged in four disks at distance of 7 m, 10 m, 14 m and 21-23 m, from the interaction point. In the forward region, for $|\eta| > 1.4$, the magnet cryostat doesn't allow the positioning of the chambers inside the magnetic field. For this reason the chamber are arranged before and after to determine the momentum by an angle measurement. At the end of march 2007 the installation of muon spectrometer was almost complete, first end-cap big wheel has been assembled in ATLAS pit, and the assembling of the others is was progress.

Fig.2.8 show the ATLAS atlas muon spectrometer section.

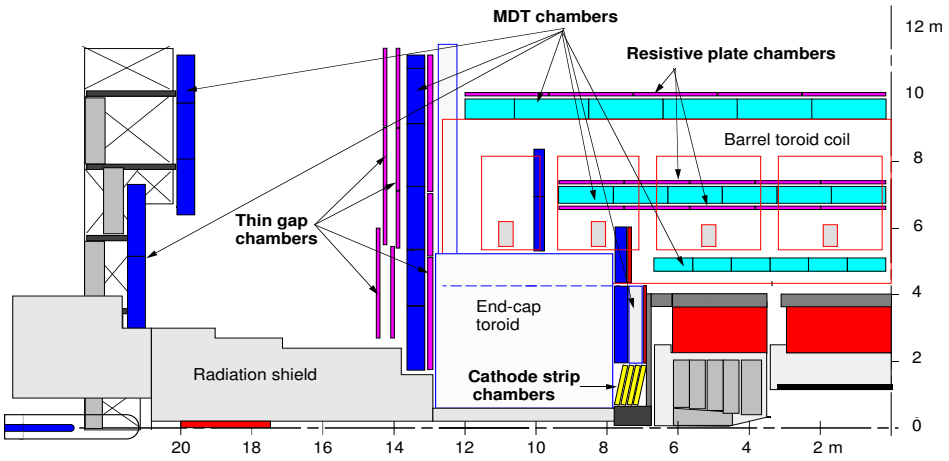

Figure 2.8: *Side view of one muon spectrometer quadrant.*

ATLAS Precision Chambers Technologies

MDT

The precision measurements of the muon trajectory is performed by *Monitored Drift Tubes* (MDTs) in all the spectrometer with the exception of the inner most layer of the end-caps. Drift tubes are made of aluminium

with 3 cm diameter and length in the range 0.9 to 6.2 m. Tubes are arranged in two multilayer, each made of three or four layer, as shown in fig.2.9. The MDT chambers use a mixture of $Ar - CO_2$ $(93\% - 7\%)$ at 3 bar absolute pressure and are operated with a gas gain of about 2×10^4. No evidence of aging effect have been found during the laboratory tests.

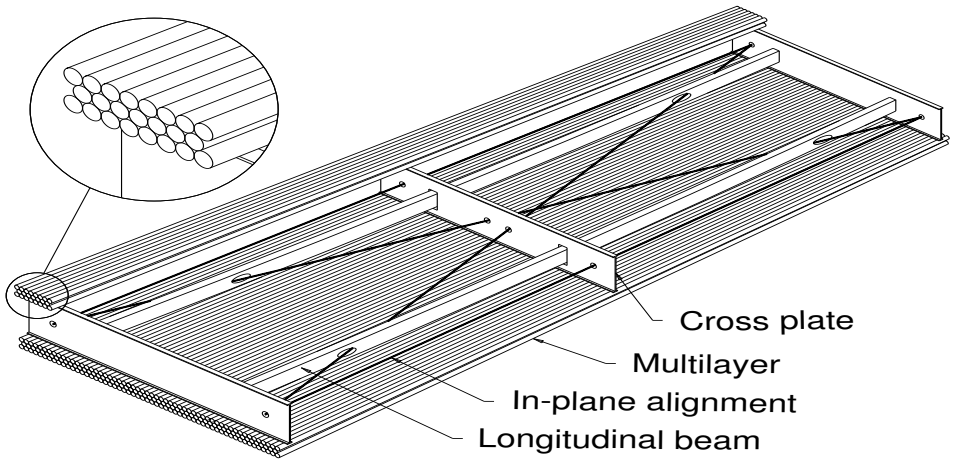

Figure 2.9: *Schematic view of MDT chambers.*

Single tube resolution is about $80\mu m$ and the resolution of a multilayer is approximately equal to $50\mu m$. Particular attention has been put at designing of the chambers to ensure the best mechanical stability. To avoid deformation, the MDT's are suspended at three points and the sagitta of each chamber is constantly monitored with a complex alignment system [42]. Thirteen institute, in Europe, Asia and North America were involved in MDT chambers construction and certification.

CSC

The background rate in the $2 < |\eta| < 2.7$ region of the inner end-cap station is so large to require the use of a precision detector with higher granularity than MDT. A MWPC with strip read out (CSC) is used to cover this spectrometer region. The sense wire pitch is 2.54 mm, and the pitch of the read out strip is 5.08 mm. The cathode is segmented into strips orthogonal to the anode wires. Due to the avalanche effect around the anode wire, charge is induced on the cathode and by charge interpolation between neighboring strips a high

precision measurement can be accomplished. The track resolution in the bending plane is $60\mu m$. The chambers are operated with a non-flammable mixture of $Ar - CO_2 - CF_4$. Advantages of the CSC are small electron drift times, good time resolution, good two-track separation and low neutron sensitivity. The chamber production was made at BNL.

ATLAS Trigger Chambers Technologies

The ATLAS muon trigger chamber must satisfy to three fundamental tasks: Bunch crossing identification with resolution better than LHC bunch spacing (25 ns), p_t threshold selection in order to reject low p_t backgrounds, Second coordinate measurement with a resolution of 5-10 mm, because the MDT chambers provide a measurement only along the bending direction.

TGC

In the end-cap region the muon trigger is provided by the Thin Gap Chambers. These are multi wire chambers operated is saturated mode. The anode-to-anode pitch is equal to 1.8 mm, and the anode to cathode gap is 1.4 mm. The cathode is coated with graphite, and external pickup strips provide the coordinate along the sense wires. The chamber is filled with a mixture of carbondioxide and *n*-pentane $(55\% - 45\%)$. Three multilayer of chambers (one triplet and two doublets) are located in the middle tracking station. Additional TGCs are part of the inner station and are used to increase the tracking ability.

Tests performed at high rate have shown single-plane time resolution of about a 4 ns rms, with 98% efficiency, corresponding to a trigger efficiency of 99.6%.

RPC

Resistive Plate Chambers, give the trigger signal in the barrel region. These are gas detector operated in saturated avalanche mode. Each unit use two gas volumes made of low resistivity plastic laminated electrodes, and four planes of read-out strips. The active material is a gas mixture composed by $94.7\% - C_2H_2F_4$, $5\% - isoC_4H_{10}$ and $0.3\% - SF_6$.
Two layer of chambers are installed in the middle station and provide the trigger for muon of low momentum. A third layer of RPC is installed on the

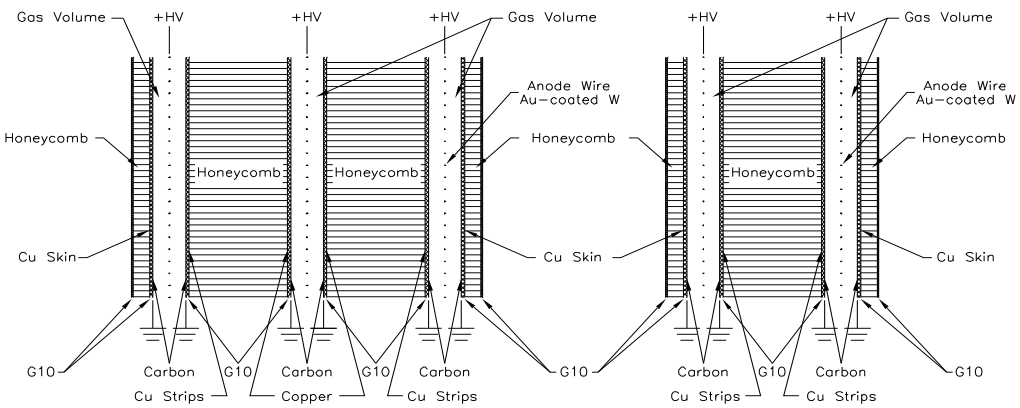

Figure 2.10: *Cross section of a triplet (left) and a doublet (right) of TGCs.*

outer cylindrical layer and it is used to trigger on the high momentum muon. RPC will provide trigger signal with 3 ns resolution, each chambers has an intrinsecal resolution below 2 ns [43]. All chamber have been produced, delivered at CERN and installed in the ATLAS muon Spectrometer. A more accurate description of the physics of the RPC detector and the solution adopted for the ATLAS experiment will be given in next chapter.

2.3.5 Trigger System

The ATLAS detector at LHC will be exposed to proton-proton collision at a rate of 40 MHz. In order to reduce the data rate only potentially interesting events are selected by a three-level trigger system. The first level (LVL1) implemented on the detector electronics, use information from the calorimeters and muon trigger detectors. The other two levels of trigger (LVL2 and Event Filter EF) are collectively called the High-Level Trigger (HLT) and are implemented on a farm of on-line computers. The HLT are based on successive analysis of the data from the whole detector [44]. A schematic view of trigger system is shown in fig.2.11.

The Level-1 Trigger Selection Strategy

The ATLAS Level-1 trigger receives information from the calorimeter and trigger muon detectors. The calorimeter trigger is based on multiplicity

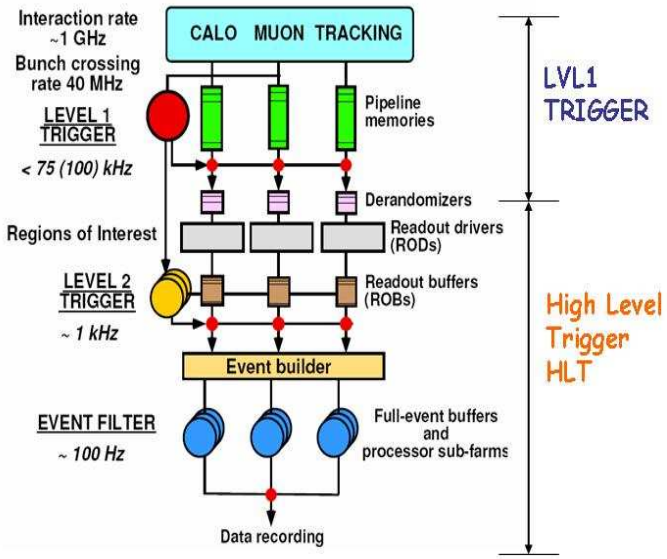

Figure 2.11: *The three physical level of the ATLAS Trigger.*

information from clusters found in the calorimeters, and from global energy deposition. Eight trigger threshold sets for each of electron/photon, hadrons/tau and jets with programmable parameters, including isolation criteria, can be operated concurrently. Total transverse energy and total missing energy of jets are calculated for each sets of programmable thresholds. The muon trigger provides information on the hit coincidences of hit in RPC and TGC detectors. Different momentum thresholds for muon tracks can be selected. The Muon Central Trigger Processor Interface (MUCTPI) combines the multiplicity information from the barrel and end-cap muon detectors avoiding double-counting single muons in regions where the barrel and end-cap trigger detectors overlap.

The Central Trigger Processor (CTP) combines trigger information from the calorimeter trigger and the muon trigger and makes the final LVL1 Accept (LVL1A) decision. This together with other timing signals is sent out to the detector front-end electronics which are organized in Timing, Trigger, and Control (TTC) partition. The decision of the LVL1 trigger is based on calorimetry (in coarse granularity) and on dedicate muon trigger chambers. LVL1 operates within a maximum latency of 25 μs and is based on special purpose hardware, using custom designed chips (ASICs) and programmable

logic arrays (FPGAs). It also provides guidance to next stage (LVL2) about regions in the detectors where high p_t objects are located, called Regions of Interest (RoI).

The High Level Trigger

The high-level trigger is based on successive analysis of data from all detectors and on the principle of early rejection. The HLT selection is executed in steps. The LVL2 component of the HLT will use mostly only a few percent of the full event data, thanks to the guidance through the RoI information provided by LVL1. It has access to the full granularity information from all sub-detectors and thus can combine for example, calorimeter and tracking information. LVL2 has to make its decision within a latency of about 10 ms. After event building, the full event information is available for EF processing, which will also have access to more detailed calibration and alignment information. The latency requirements are less strict than for LVL2: the average time for an event decision is about 1s. Both components of the HLT will perform a selection based on algorithms implemented in software, thus proving a very flexible approach to cope with changes in conditions.

Chapter 3

The Resistive Plate Chambers in the ATLAS experiment

3.1 Introduction

Resistive Plate Chambers, were developed by R.Santonico and R. Cardarelli [45]. The RPC is a gaseous parallel-plane detector, with a typical space-time resolution of the order of $1cm \times 1ns$ with digital readout. RPC operation is based on the detection of the electrical discharge generated when a charged particle go through the gas volume.
RPC are the evolution of the Parallel Plate Avalanche Chamber (PPAC) introduced by Pestov [46], which used a metallic plane as electrode and as a consequence of this choice when a charged particle generated an electrical discharge, the electrical potential on the detector surface decrease, increasing the dead time of the detector. The introduction of a resistive plate as electrode removed this limitation and make easier the realization of the detector.
Typical RPC is made of two bakelite plate kept parallel by insulating spacer, which define the size of the gas gap. A very high uniform field (50 kV/cm) produced by a differential potential applied on the bakelite plates produces the avalanche multiplication of the ionization electrons. The signal is read out via capacitive coupling to metal strips placed at both sides of the detector. A schematic view of RPC detector is shown in fig.3.1.

Due to their very good time resolution, good space resolution and relative low cost RPC play an important role for the generation of the first level muon

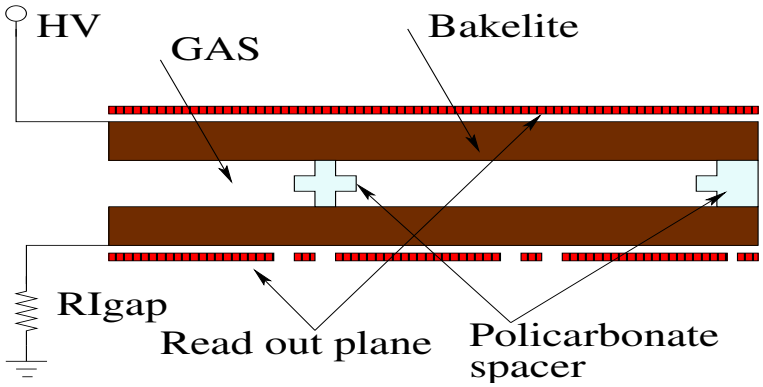

Figure 3.1: *Schematic view of a single gap RPC.*

trigger in many HEP experiments.

3.2 RPC working principle

When a particle through a material it loses energy in according to the Bethe-Bloch formula [20]. The inelastic collision of a particle in gaseous means can produce electron-ions pair *primary ionization*. If the electron generate from the primary ionization has enough energy, can itself generate an electron-ions pair *secondary ionization*. If an electric field is applied to the gas container the electron and ions start to drift along the field line. For a field enough strength the electrons quickly catch up the energy necessary in order to produce a new ionization. The process is cumulative, and the number of free electrons will go increasing generating an avalanche which grows exponentially according to:

$$n = n_0 e^{\alpha x} \tag{3.1}$$

where n_0 is the initial number of electron, α is the first *Townsend coefficient* depending on the applied high voltage and on gas mixture and x is the path where avalanche grow up. In eq. 3.1 the number of electron can grow indefinitely, but it is limited to about $\alpha x < 20$ after which breakdown occurs, this is know as the Meek limit [47], [48]. The charge produced by RPC operating in region near the Meek‘s condition is about 100 pC, this is called streamer operation. Due to the relative high charge produced, RPC

operated in streamer cannot support high particles rate typical of hadron collider environments. In order to limit the charge production and ensure an stable working point, for the RPC detector, many study have been performed on the gas mixture. In particular have been tested gas mixture with small amounts of sulphur hexafluoride (SF_6) which is able to limit the avalanche grow (*saturate avalanche regime operation*). Results show that gas mixture with SF_6 assure $\sim 1kV$ operating plateau in pure avalanche mode with detection efficiency $> 98\%$ [49].
ATLAS RPC are operated in saturate avalanche regime. Fig. 3.2 shows the detection efficiency and streamer probability for $C_2H_2F_4/iso - C_4H_{10}$ gas mixture with different amount of SF_6, as a function of applied high voltage.

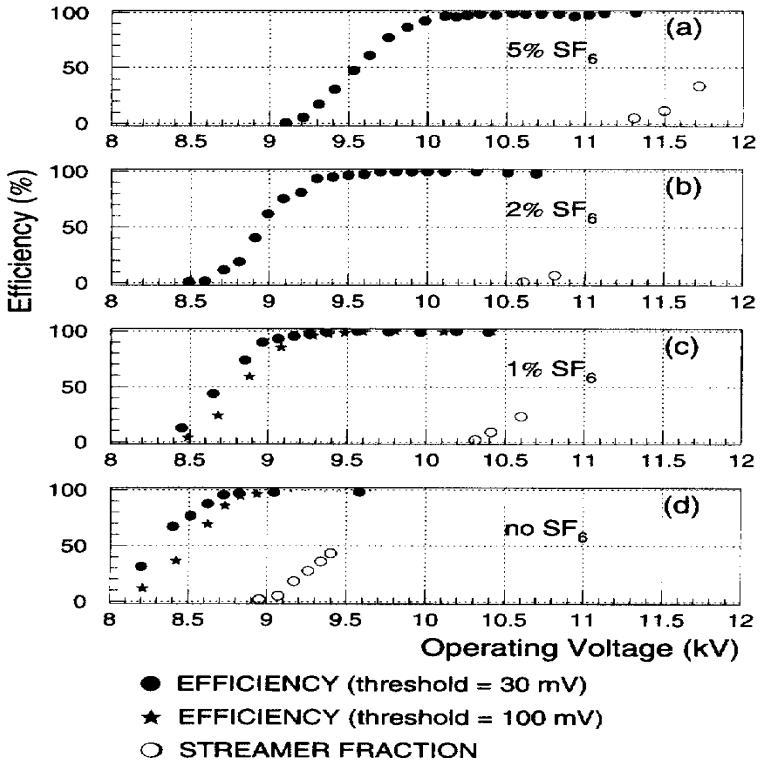

Figure 3.2: *Detection efficiency and streamer probability vs. operating voltage for (a)5%, (b)2%, (c)1% SF_6 concentration and (d) no SF_6*

3.3 The ATLAS RPC detector

The main tasks required to the ATLAS RPC system are:

- Fast tracking to discriminate on the muon transverse momentum p_t ;
- Good time resolution for bunch-cross identification;
- Good rate capability to stand the low p_t neutron and gamma dominant background;
- 2nd-coordinate measurement with a required resolution of 5-10 mm.

Several studies have been performed in order to realize a detector able to fulfill this requirements.

An ATLAS RPC unit is composed by two independents layer of active detector, each one equipped with two orthogonal read-out strip panels, thus allowing two independents lectures for both η and ϕ coordinate. The first layer of active detector consist of: pick-up strip panel, segmented in the azimuthal (ϕ) direction, a bakelite planar chamber containing 2 mm thick active gas layer, a plastic foil insulating th HV side of the bakelite gas gap from a second pick-up strip plane, segmented along the longitudinal (η) direction.
A central support panel made of sandwich of paper honeycomb and aluminum skins act as a Faraday cage avoiding cross-talk between the two layer of detector. The second layer of active detector is identical to the previous but is assembled in the reverse order. A support panel made of paper honeycomb and aluminum skins or aluminum honeycomb and aluminum skins on each external side provide the necessary mechanical robustness. A shunt resistance of 100 $k\Omega$ connect the gas volume with the Faraday cage allowing the measurements of the current that flow inside the gas volume applying the high voltage (dark current). The total thickness of an RPC module is about 100 mm and the active area span from about 0.4 m for the smaller unit to more of 1.1.5 m for the largest type.

Gas volumes have been produced at General Tecnica (GT) in Colli (FR-ITALY), starting from 2 mm thick bakelite plates selected according to their

bulk resistivity ($\rho \sim 1 - 4 \times 10^{10}\Omega/\Box$)cm[1] and the external surface are coated with graphite for the high voltage distribution. The graphited side has covered with 190 μm of Polyethylene-Trephtalate (PET) to ensure electrical insulation. Finally the gas volume has assembled sandwiching two balk plates with a $10 \times 10 cm^2$ grid of polycarbonate spacers which define the 2 mm gap and a special frame (containing the gas in-let and out-let) which define the closed volumes (fig. 3.3.

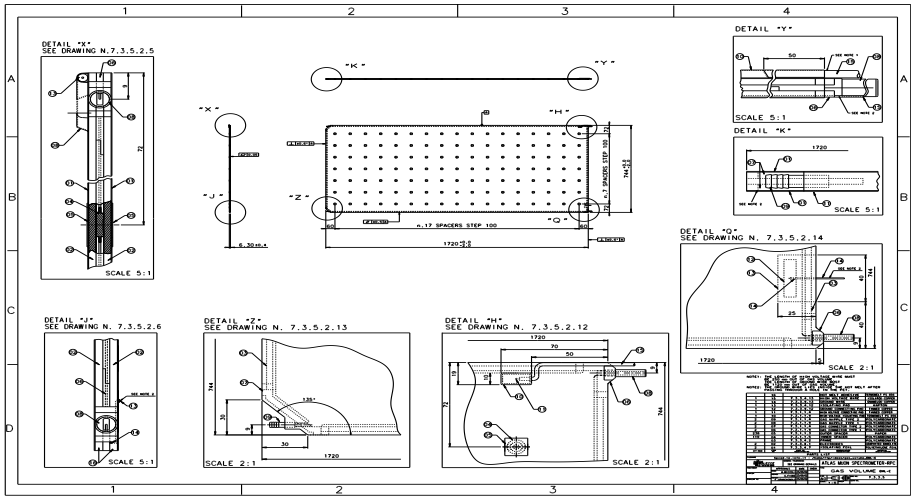

Figure 3.3: *ATLAS RPC Gas Volume design with the in-let/out-let details, design at the INFN Lecce CAD*

After the mechanic assembly the internal surface of each gap has treated with linsed oil in order to reduce eventually surface imperfection. An high voltage test has performed before the delivery to the RPC assembly site.

The front-end (FE) board is based on an 8 channel GaAs custom circuit chip consisting of a three-stage voltage amplifier followed by a comparator which give 6 ns shaped standard ECL signal. The amplifier output is bipolar giving zero integrated charge, thus avoiding a possible dependence of the steady output voltage on counting rate.
The chip is used in form of die to avoid extra cost of packages. It is glued

[1]The surface resistivity is measured in Ω but usually it is indicate with $\Omega/\Box$ to denote that the surface is measured on a square independently on its dimension.

on a 4 layer printed board using a sliver epoxy adhesive and electrically connected via wire bonding. The FE board has the purpose of detecting and discriminating the 1 pC detector signal associated with the passage of particles charged. Physical threshold V_{ph} is set on the comparator applying a negative voltage V_{th} between 0 and -1.4 Volt using the formula:

$$V_{ph} = V_{th} - \frac{V_{ee}}{3} \tag{3.2}$$

where $V_e e$ is the supply voltage which is set to -6 Volt.
A back-end board is used to terminate the signal pick up strips and distributing the test pulse signal to the front-end. Both boards are embodied inside the read-out panels, which have been realized with a copper layer on pet substrate shaped in strips by milling and glued on a supporting foam slab. Read-out electrode are made of copper strips with pitch in the range (26.5-39)mm depending on the unit type.
After the electronic integration at the Napoli INFN labs all read-out panels have been tested in Roma2 INFN lab, and than delivered to Lecce labs to the RPC assembly site.

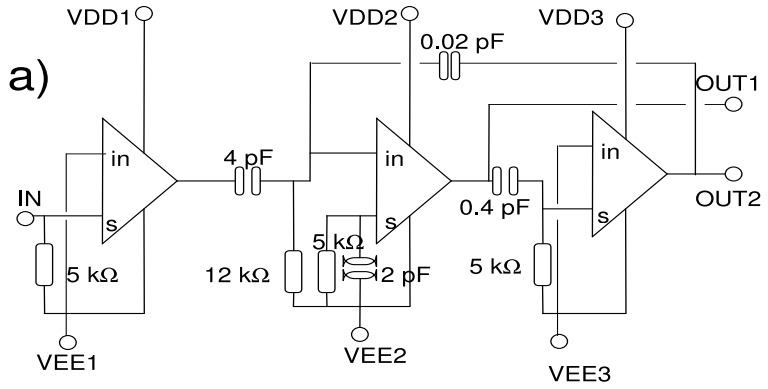

Figure 3.4: *Block diagram of the ATLAS RPC three-stage amplifier.*

To ensure the perfect mechanical realization, a dedicated assembly facility has been realized at the Lecce INFN laboratory, where all the component delivered from all the production site has been assembled using specific tools. In final layout the RPC unit are rigidly held together by two support

panels which provides the required mechanical stiffness of the chamber. Full size prototypes have been successfully tested with and without particle source[50]. These test showed that ATLAS RPCs, equipped whit final front-end electronics and realized with all the previous described material, can work with high efficiency and high resolution up to $10^3 Hz/cm^2$.
In fig.3.5 is shown the final ATLAS RPC layout, main mechanical structure are in evidence.

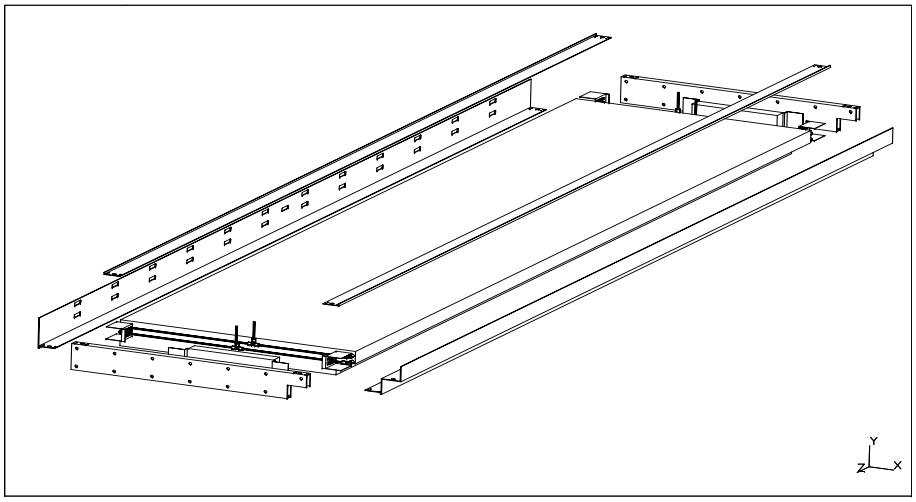

Figure 3.5: *Exploded view of ATLAS RPC units.*

The RPC in the ATLAS Muon Spectrometer

The ATLAS Muon Spectrometer in the barrel region is divided in three coaxial cylindrical region:*Inner, Medium and Outer*, at radial distance of about 5, 7.5 and 10.5 m. In the transverse plane, the eight coil divide the Muon Spectrometer in 16 sector, (8 Large, 8 Small, see fig.3.9)

One or two units coupled together form a trigger chamber (see fig. 3.7) which are organized in three layers located above a below the MDTs in the middle region, and above the BOL or below the BOS MDTs in the outer region. The MDT-RPC system are called station.

The longitudinal and lateral dimension of the RPCs have been chosen such that their active areas match the ones corresponding MDTs. Full acceptance

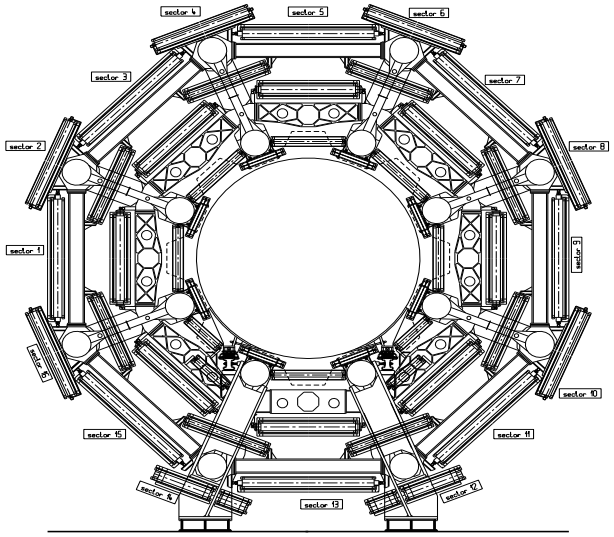

Figure 3.6: *View of the ATLAS Muon Chambers in the barrel region.*

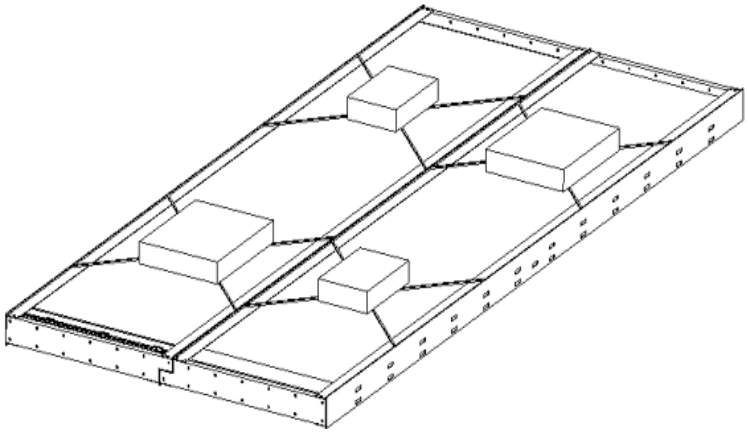

Figure 3.7: *ATLAS RPC Chambers with the electronic box installed.*

is achieved by overlapping the active zones of the RPCs in the same sector and between the adjacent sector.
The total number of RPC unit installed is 1116, and they cover a total surface of about $4000m^2$. Several special unit have been designed and realized in order to cover region in which are present mechanical interferences with

other part of the detector, or MDT alignment system corridors.
The standard unit classification is a consequence of the chamber final position in the Muon Spectrometer and their longitudinal and transversal dimension. The acronym which identify the chamber consist of four letter, the first **B** is used to indicate the barrel position, the second **M/O** indicate the Middle or Outer layer, the third **S/L** is relative to Small or Large sector, the last one **A, B, ... G** indicate the longitudinal size, 23 different topology of standard unit have been realized. RPC unit dimension as function of typology are listed in tab. 3.1.

Length (mm)		*Width (mm)*	
BOL	5090	A	1200
BOS	3900	B	1080
BML	3680	C	960
BMS	3200	D	840
		E	720
		G	480

Table 3.1: *ATLAS RPC unit dimensions.*

3.4 Muon Selection in the ATLAS Barrel Region

The scope of the RPC, is the selection of events with muons having large p_t coming from the interaction vertex. Together with the detector a complex electronic ans software system has been designed to absolve to this scope.

3.4.1 Muon LVL1 trigger technology

The basic element of the ATLAS muon trigger is the **Coincidence Matrix (CM) ASIC** which contain both local and trigger readout functions. It is mounted on the RPC chamber very close to the front end electronics to reduce the cable length. RPC signals are sampled by the CM every 3.125 ns into pipelines of programmable depth which are used to correct for different cable length or time of flight. Each CM has 192 input channels and provide

low or high p_t algorithms in one Regions of Interest. An CM dedicate to low p_t together with the relative high p_t CM form the Local Logic (LL) that selects the muon candidate in an area of $\Delta\eta \times \Delta\phi = 0.2 \times 0.1$ (η CMA) and $\Delta\eta \times \Delta\phi = 0.1 \times 0.2$ (ϕ CMA).

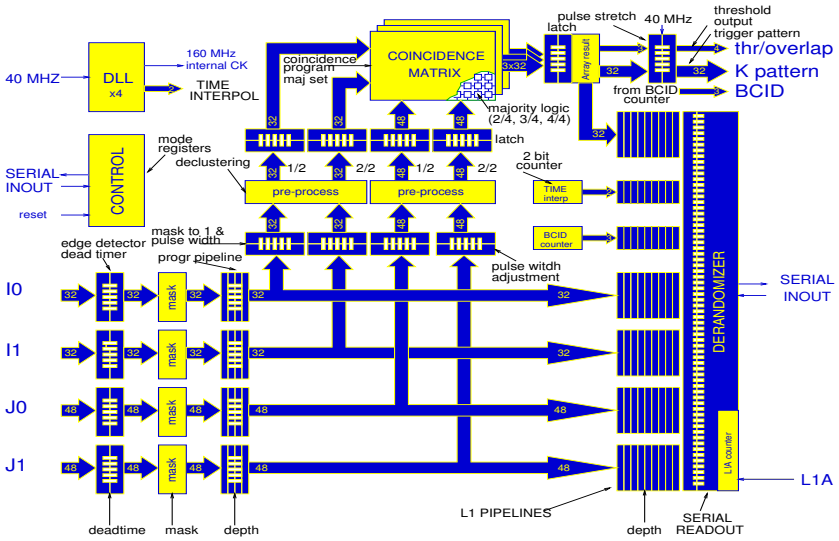

Figure 3.8: *Scheme of the ASIC Coincidence Matrix.*

The **Pad Logical board** (PL) combines the trigger and readout information from four LL, two PL boards are used in a trigger tower, one is used to perform the low-p_t trigger and another for the high-p_t. Each Pad covers a region $\Delta\eta \times \Delta\phi = 0.2 \times 0.2$, associate the muon candidate with a region $\Delta\eta \times \Delta\phi = 0.1 \times 0.1$ and with the correct bunch crossing, solves overlaps due the cabling and selects the highest p_t threshold triggered track in the pad. Low-p$_t$ boards send trigger and readout data to the corresponding high-p_t boards, while high-p_t boards send trigger and readout data to SL boards. Each physical sector, small or large, is divided in two parts along z and in two parts along ϕ, the resulting area is denominate **Logical Sector**, in this way for each physical sector we obtain 4 Logical Sectors (LS) 64 LS in total. On each LS there are 6/7 Pad for high and low p_t related to one Sector Logic (SL) board which sorts the candidates by p_t and select up to 2 tracks per sector. The SL is also able to solve the double counting generate by muon passing in the PL overlap region.
The **MuCTPI** (**Mu**on to **C**entral **T**rigger **P**rocessor **I**nterface), collect the

information from 64 barrel SL, 96 end-cap SL and 48 forward SL (208 in total). Each of which can deliver up to 2 candidates to the the MuCTPI. It calculates the number of received muon candidates for each muon p_t threshold and sends the multiplicities on 3 bits per threshold (18 bits total) to the (Central Trigger Processor) CTP. The CTP takes the LVL1 decision generating the accept signal.

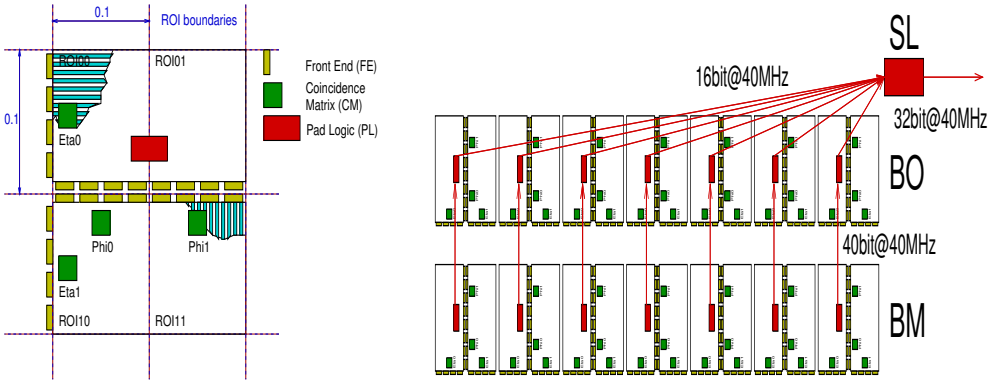

Figure 3.9: *Position of the local trigger logic circuits on the RPCs and scheme of the trigger data links among Pad Logics, Sector Logic and Central Trigger Processor.*

3.4.2 Muon Selection Algorithm

The muon selection algorithm in is based on the measurement of the deflection of charged particles passing through the magnetic field region.

The selection mechanism is based on the definition of allowed geometrical roads (*Coincidence Windows*) whose is defined by the infinite momentum track. The muon track distance from the center of the Coincidence Windows is mainly a function of the muon p_t. The higher is the p_t the smaller is the distance, applying this mechanism the algorithm selects only muons with a p_t greater than a certain value (threshold definition). Fig. 3.10 shows the possible low and high p_t coincidence. Two threshold regimes for muon trigger have been chosen:

- Low-p$_t$ muon trigger ($6 \leqslant p_t < 20$ GeV): This regime maximizes the B-physics trigger capabilities in the context of a possibly staged initial Trigger system. In the barrel subsystem low-p$_t$ trigger analyzes signal

coming only from the middle RPC station. Usually 3-out-of-4 majority coincidence is required.

- High-p_t muon trigger (> 20 GeV): It operates only in presence of a low-p_t trigger by requiring the spatial coincidence with the outer chamber and requiring 1-out-of-2 majority.

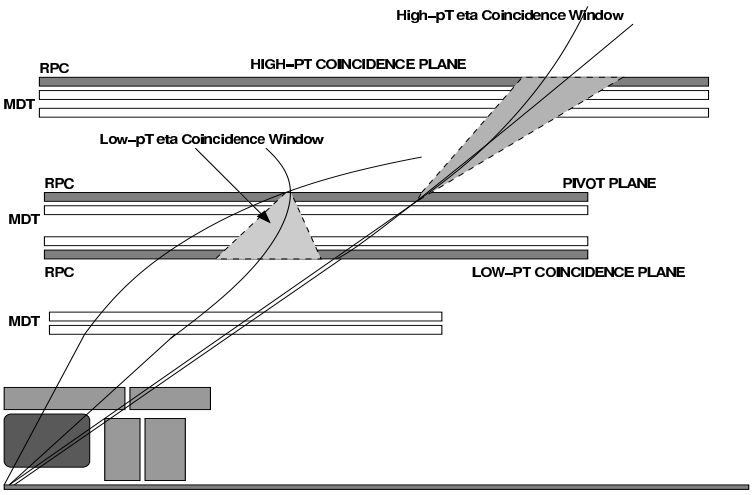

Figure 3.10: *Scheme of the muon trigger algorithm in the barrel region.*

The system is designed so that up to 3 p_t threshold for low-p_t and 3 p_t threshold for high-p_t can be applied in parallel. At the present trigger threshold are set to: **6**, **8** and **10** GeV for Low-p_t and **11**, **20** and **40** for GeV High-p_t. The lower available threshold value is limited by the cabling and it is equal to 5 GeV.

3.4.3 Coincidence Windows and Cabling

The Coincidence Windows define which strips of coincidence plane are associates to every single segment of pivot plane. This corresponds to the cabling of the coincidence matrices. The size of the window opening whit the respect to the momentum threshold is determined primarily by the Monte Carlo. However, the exact determination of the window sizes is dependent on constraints originating from the readout system design. The readout

is performed on the basis of groups of strips connected to the CM via strip connector. For the η-trigger system, 8-pin strip connectors are utilized at the pivot plane, while 4-pin connectors are employed on the coincidence planes. The ϕ-trigger system uses only 8-pin strip connectors. This design governs the granularity of the coincidence windows definition. One has to remember that CMs cannot accept more than 32 inputs on the pivot plane entry, and 64 inputs on the coincidence plane entry. In order to assure correct windows implementation same channels are read-out by two CM at the same time, this is achieved through the use of signal splitters. Fig.3.11 shown a configuration for a Large Trigger Sector, for the η-CMs, this will be used in last chapter where will be analyze the first data of Sector 13.

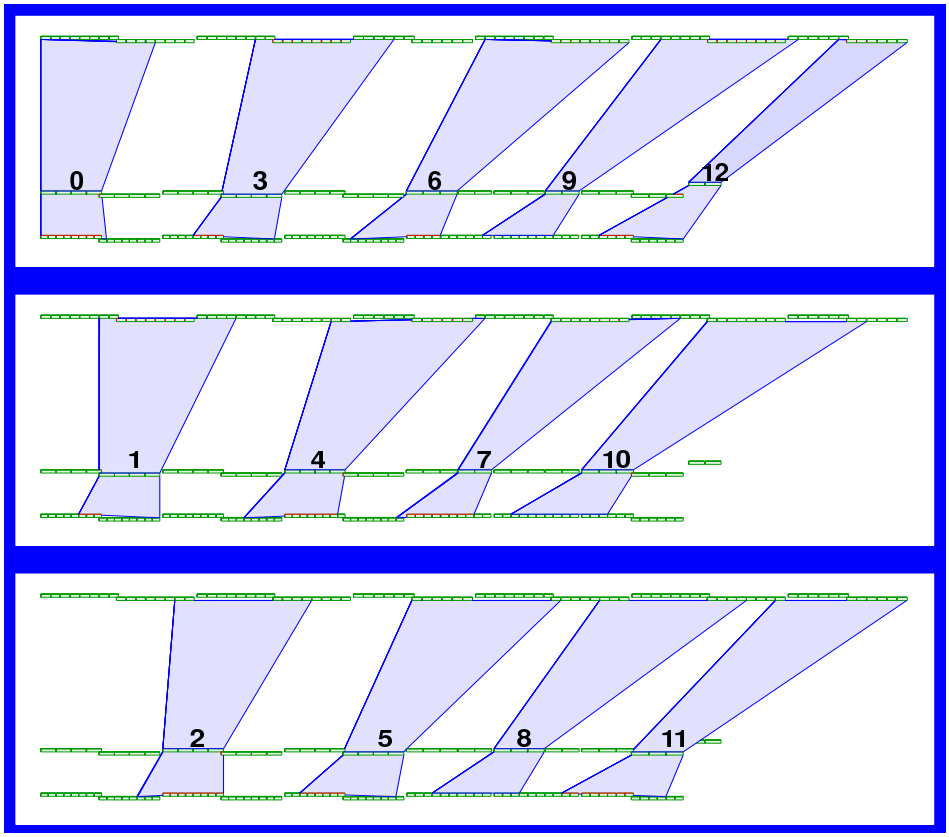

Figure 3.11: *Cabling of a Large Trigger Sector, Coincidence Matrix are listed on the pivot plane.*

The cabling for the ϕ-trigger defines which ϕ strips of the coincidence plane are fed into the ϕ-CMs. These strips must be situated within the span of the coincidence windows defined by the η cabling of the two η-CMs overlapping with a ϕ-CM. This is equivalent to the cabling of the full PAD unit. Since the PAD windows can encompass several chambers of the coincidence planes, it is necessary to link the corresponding strips through a system of Logical OR. In this context, an additional constraint must be taken into account: the association in Hardware OR of the two consecutive chambers belonging to the same overlapping RPC units. An illustration is given in Fig.3.12, showing the cabling of the second ϕ-CM in a Large Trigger Sector.

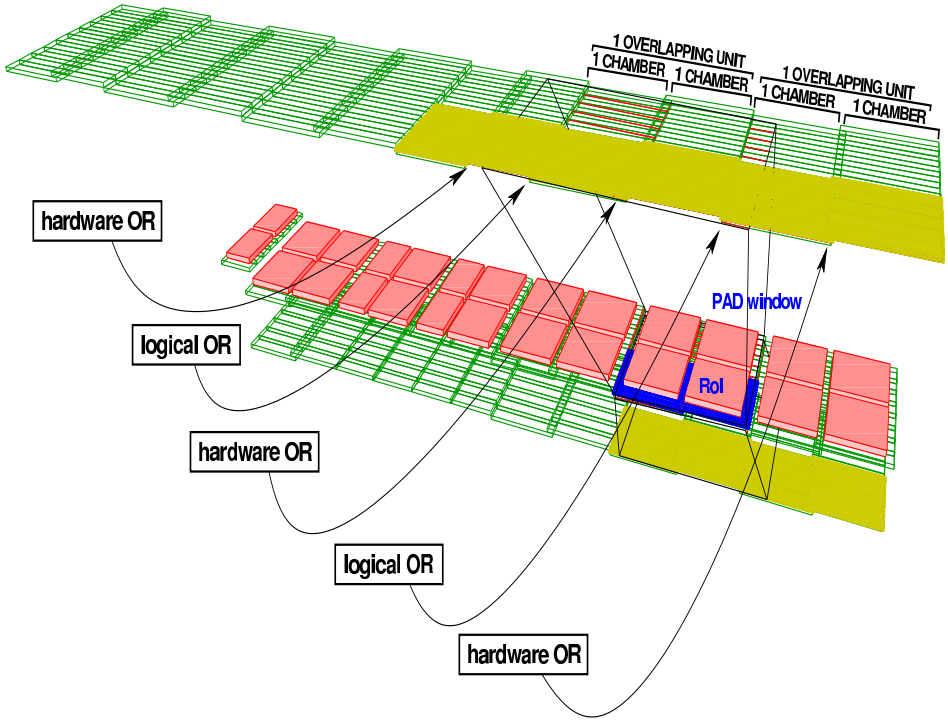

Figure 3.12: *Phi Coincidence Window scheme.*

This illustrates which strips are readout to the second ϕ-CM of a Trigger Large Sector, and how strips from different chambers are connected by the OR system. Strips feeding the pivot entry of the CM are shown in blue, strips feeding the coincidence plane entry of the CM are shown in yellow. Groups

of 8 strips are shown in green (corresponding to 8 pins strip connectors) over the entire Trigger Sector. The span of the ϕ-cabling of the high pt CM is rather important, covering half of the corresponding coincidence plane. The ϕ-cabling on the coincidence plane can involve up to 3 RPC chambers (6 units).

Chapter 4

ATLAS RPC cosmic ray test facility in Lecce

4.1 Introduction

The RPC production has been optimized during years with many efforts from the research laboratories and the involved industries. The production chain of these detectors has been organized in order to allow for an optimal sharing of task according to the different skills available at each collaboration site. The production involved the Physics Departments and INFN Sections of Lecce, Naples, Rome Tor Vergata and the Protvino IHEP. Each production site had the responsibility of a specific part of the RPC unit which finally were assembled in Lecce [51]. Fig. 4.1 shows the RPC production chain.

The time of life of the experiments installed at LHC is expected to be about 10 years, for this reason each RPC units have been accurately tested after the production and before the installation on the experimental apparatus. The tests have involved all the principal RPC components and have been focusing on the following aspect: *Electric Test*, *Gas Tightness*, *Efficiency, Noise, Cluster Size and Gap Dark Current measurements*. The units that not ensure adequate performance have to be repaired or eventually substituted. This process is denominate in the following Q.A. Cosmic rays telescope can be used to perform all the requested measurements and to this purpose three cosmic ray test stations have been built and setup in Lecce, Naples [52] and Rome Tor Vergata Physics Department and INFN Laboratories.

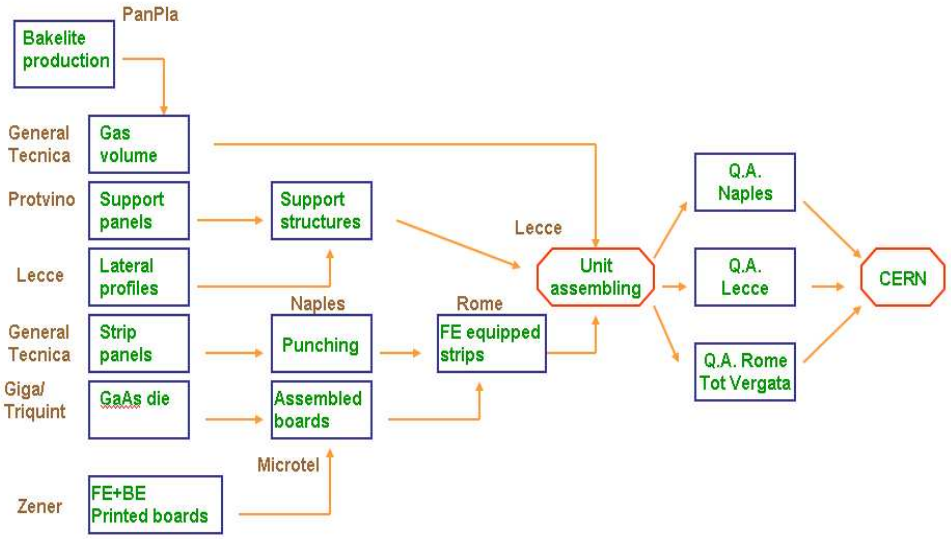

Figure 4.1: *RPC production and test chain. Together with the production phase are listed the production site or the industry in charge of the production.*

Although the three facilities use different techniques to trigger and reconstruct cosmic rays, very similar test are performed, in order to have standard detector quality certification.

In this chapter will be given an extensive description of the Lecce cosmic ray test station and of the test performed.

4.2 Test Facility Overview

The Lecce RPC cosmic ray testing facility[53], consists of several subsystems: gas system, power system, (for low e high voltage distribution), Data Acquisition System, Detector Control System and Trigger System each one with a specific task. With it is possible to test 8 standard RPC detector at the same time using 4 RPC units to produce the trigger and a tracker system. The 4736 read out channel allow to test up to 64 read out panels, 32 gas volumes and all the other element that complete the detector (pulse system, high voltage and low voltage connector, threshold distribution). In particular, custom made DAQ [54] and DCS [55] allow to acquire data

produced by the passage of a cosmic ray particle and to set and monitor all operational parameters of the test stand.
Same software tools and programs (locally written and developed) allow an easy monitoring, data analysis, display of events and results on easily accessible web pages.

4.2.1 Mechanical Structure

The mechanical structure allows for the housing of two RPC trigger modules on the top and two on the bottom, the latter being separated by about 10 cm of iron absorber acting as a low energy, high multiple scattered particle filter. The units under test are located between the tracking system by means of the use of a mobil support mounted on rails that allows to host two groups of 4 unit each, at the same time.
In order to control the temperature of the whole station a plastic tent has been mounted around the apparatus and two air conditioner have been installed near the test stand inside of the volume limited from the tent.

The read-out cable are hosted behind and laterally to the structure in order to allow an easy connection with the read-out channels and to avoid interference with the mobile support. All cables are not completely fixed to the main structure, allowing to test easily unit with different size and layout. The mechanical structure is completed by three patch panels installed on the frame of the structure itself that hosts low voltage boards and gas services. Fig. 4.2 shows a picture of the the cosmic ray testing facility.

Gas System

The flow of the gas mixture (94.7% C2H2F4, 5% C4H10, 0.3% SF6) is provided by the system illustrated in Fig. 4.3. The gas components to be mixed are contained in bottles located outside of the laboratory and the three different lines connect the bottles to three flowmeters that are controlled by an MKS Gas Controller system which provide the control and setup of the correct gas mixture. The MKS and the flowmeters are controlled by a dedicated DCS software module running on a dedicated PC which allow to set and easily control the gas mixture and the flow. The three lines are sent to a gas mixer and if the gas composition deviates from the selected amount by more than 5%, an automatic hardware system switches off RPC high voltage on the detector. In addition, a buffer is placed after the mixer

Figure 4.2: *The Lecce cosmic ray testing facility.*

in order to smooth out any sudden changes in the gas composition. A safety bubbler vents off the gas at an adjustable value of pressure (between 0 and 10 mbar) with respect to the atmospheric pressure to prevent excessive inflation of the RPC gas gap. The buffer output is then split into 20 gas lines, 4 for the Trigger RPCs and 16 for the modules to be tested. Each line is equipped with an flux adjust to split fairly the flow in each line, two pneumatic valves, one at the input and the other at the output, and with a high precision differential pressure meter in order to perform a gas leak test on each individual bakelite gas gap layer.
All the hardware necessary to the gas system is lodged in two dedicated rack located on a side of the test stand. On the other side is mounted a patch panel where are located the bubblers relative to each gas line. All the gas

line output are sent to the air out of the laboratory.
The gas DCS modules sends at regular intervals, information about the mixture to the main DCS PC that provide to store the information in a dedicate historical file. Moreover information about the gas mixture are also automatically stored in each run acquired.

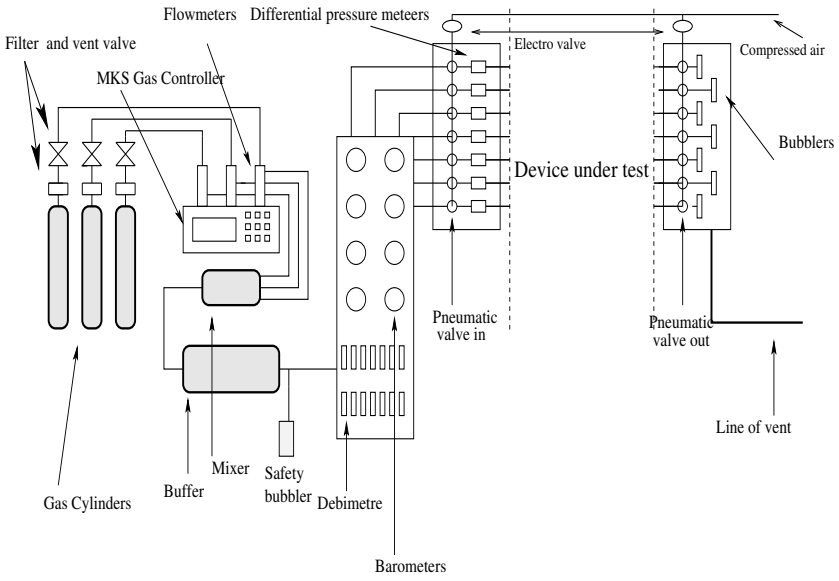

Figure 4.3: *Schematic view of Lecce test stand gas system.*

4.2.2 Power System

A multichannel system for High Voltage (HV) and Low Voltage (LV) supply has been setup in order to provide power to the detector and to the front-end electronics. Moreover each read-out strip panel have an independent front-end threshold that must be set via a low voltage signal.

Thirty six high voltage channels are fed by a CAEN SY1527 power supply mainframe equipped with six CAEN SY1526 boards (six channels each). Each gas volume of the modules under test is connected to a single high voltage supply for a maximum of 32 channels, while the 16 gas volumes of the trigger chambers are served by the last four voltage lines through home-made high voltage splitters. The high granularity allow to control for each gas volume under test the current supplied from the CAEN, and via ADC to read-out on the shunt resistor the current that flow inside the gas volume.

The high voltage system is remotely controlled, using OPC Server Technology [56], that allow the DCS to generate complete configuration and control of the HV system. An hardware kill signal is sent to the mainframe by the gas system in case of abnormal flow or abnormal mixture composition.

The RPC front-end electronics is powered by 20 (LV) supplies generating -5.1 Volts. The current absorbed by each power supply is measured using a multi-ADC channels PCI card hosted and read out from the DCS PC. To minimize the cable length the LV power supply are positioned laterally to the test stand into two dedicated patch panels. Each power supply is connected to 4 strip panels (2 ϕ and 2 η) on the side of an RPC modules.

On the same patch panel used for the LV power supply are also installed 4 DAC which supplies the voltages defining the threshold of the RPC front-end electronics. They are connected to the chambers with cables less than 2 m long in order to minimize signal attenuation. The thresholds of the trigger RPC modules are usually set to a fixed value for all strip panels.

4.2.3 The Data Acquisition System

The Data Acquisition system (DAQ) is based on VME modules designed an built at INFN of Lecce electronic service (Latch)[57]. Latch module provide a sampling of input signal at regular step of 15 ns using a 32 bit FIFO memory for a total depth of 465 ns. Each module allow to red-out 96 channel in three independent section (bank). For each bank an ECL fast or signal is available. Latch module status is set and controlled through "stop" and "clear" signal that manage the acquisition process. The entire system is read-out via VXI. The hardware of the DAQ system is made by 75 Receiver [58], which provide to terminate the output signal, lodges in 5 crates and 50 latches lodged in three different crates. All the crates are located in a single rack.
The connection between Detector-Receiver-Latch are realized with about 750 flat cables with different number of channel and different length in order to diminish the total length. The total system is capable to read up to 4736 channels. The VME crates are read-out by a PCI-MXI board, located on the PCI bus of the DAQ dedicated computer, and three MXI-VXI board, located on each VME crate. The DAQ software has been designed, written and realized with the LABView package software[59] which allows to generate automatically a Graphical User Interface modifiable according to the necessities of the users (see fig.4.4).

The program is subdivided in four different sections: *Configuration, Run,*

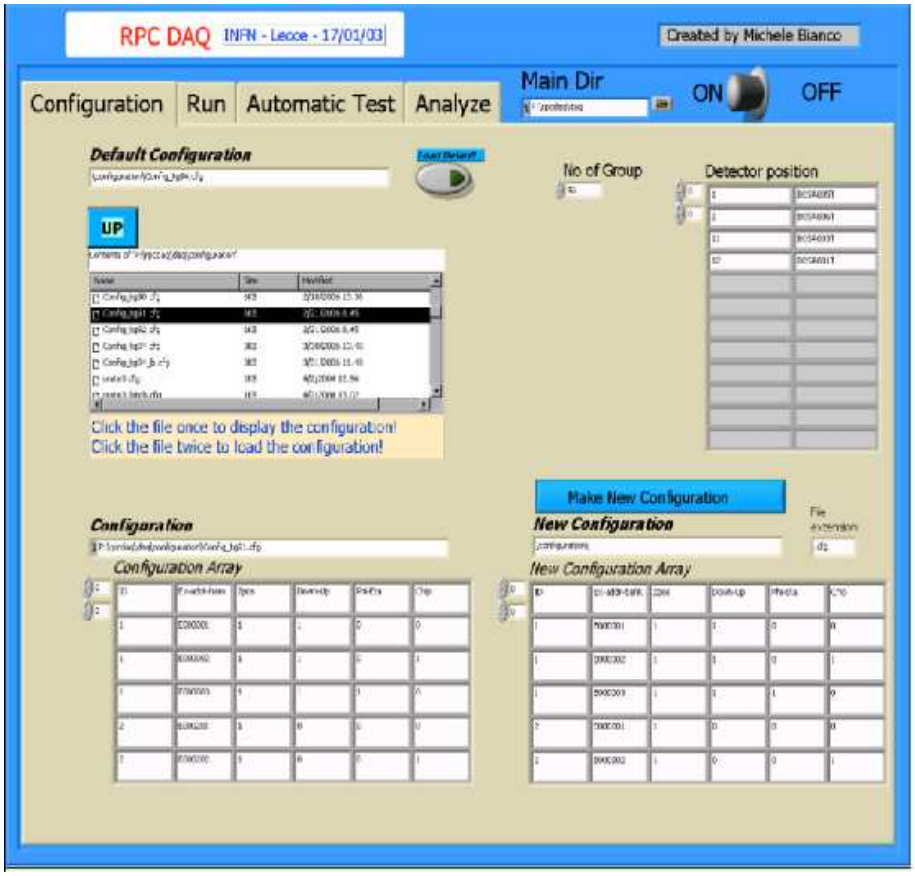

Figure 4.4: *Graphical User Interface of the DAQ of the ATLAS RPC test stand in Lecce .*

Automatic Run and Analize each one with a specific task. The *Configuration* section allow to choose the right hardware configuration or if it is not present it allows to generate a new configuration. In the second section, *Run* , the user set all parameters that characterize the data taking (*Number of events, type of trigger, comment about setup, etc...*) and can start the data taking. The *Automatic Run* section just display the condition of the detector during the automatic run controlled by the DCS system. The last section, *Analize*, allows a fast data analysis, producing an event display (see fig. 4.5) and few other general plots and histograms about the detector behavior.

During the data taking the DAQ provide to collect and organized two

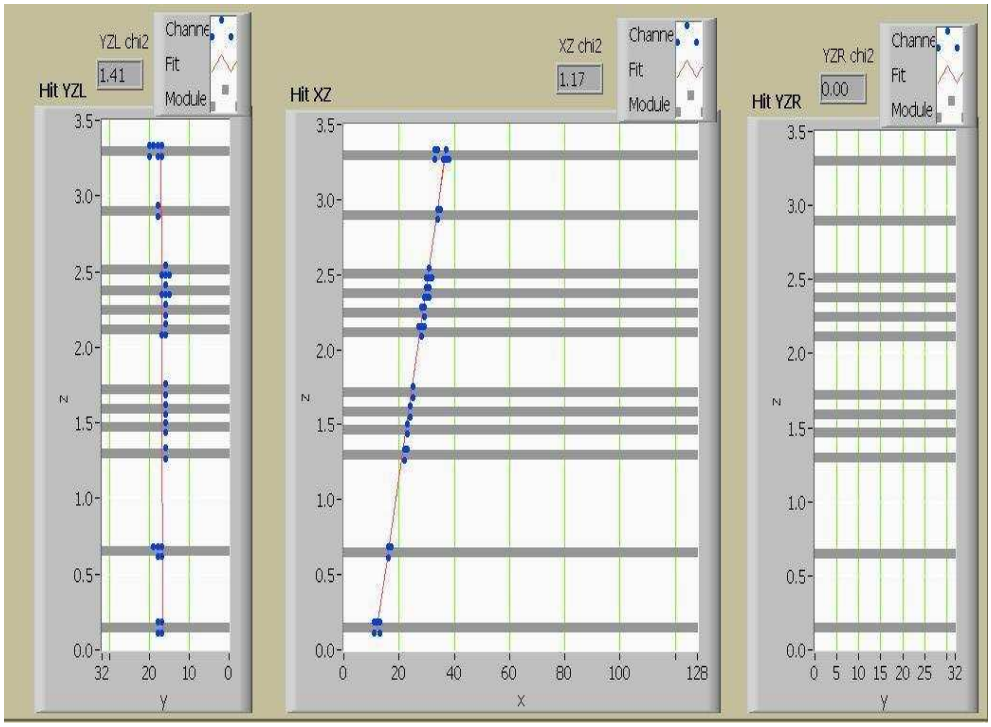

Figure 4.5: *On-line event display generated by the DAQ. The three side of read-out are shown, blue dots represents the RPC hits and a simple straight line is overimposed.*

types of data cosmic RPC event and DCS event: the first one is used to perform the unit test the second one used to monitor all the chamber and environmental parameters.

All data are written in a binary file and for each data taking period (run) is generated a log file. All files are temporary stored in a folder on a distributed file system (AFS) where also the DAQ program is installed. At the end of each run the data file is automatically copied on the ATLAS Group file server, and the main information (header) of the run are inserted in an ATLAS MySQL Remote Database to be used later for the automatic offline analysis.

4.2.4 The Detector Control System

The aim of the DCS is to allow the user to set and monitor all parameters that determine the response of the detector (HV, Low Voltage, FE Threshold, currents etc..). Moreover the DCS have to monitor all the environment parameter that can modify the detector response (Atmospheric pressure, Temperature and Humidity). The DCS runs on 2 separate computers connected together through TPC IP and in AFS system, one of them manages the gas flow and the ADCs and DACs serving the left side of the test station, the second one communicates and controls with the HV power supply and manages the ADCs and DACs on the right side

Like the DAQ, the DCS program has been developed with the LABView package which allows the direct interface with all the installed hardware.

The DCS is made two separate programs but communicating each other. One is devoted to control only the gas system and the other manages all the rest of system (HV, LV,threshold and reading of currents, pressure and temperature probe, etc) used by the teststand.
An important task of the DCS software is the management of the automatic procedures for data acquisition: an generic sequence of runs can be set, and the DCS can setup the DAQ configuration to provide the correct execution of the loaded sequence. This high level of automation of the run control software makes possible to collect the whole data sets and sequences required for the unit certification without human intervention.

4.2.5 Trigger

Given the test station geometrical configuration, the removal of a very low momentum cosmic ray particles due to the use of the iron absorber. the rate of cosmic rays impinging on the test stand is about 50 Hz.

The available read-out hardware provides a limited DAQ bandwidth which would imply an acquisition rate of 4-5 events/second in case of full data recording (144 latch bank matrices). Since in a typical cosmic event only part of the matrices bear a signal (48), by applying zero suppression and by reading only a limited set of temporal bins (6, for a total time window of 90 ns) the total cosmic ray rate can be sustained by the system.

Cosmic ray tracks are selected by a hardware trigger logic followed by a more refined on-line selection. The "first level" hardware trigger logic is realized with NIM modules. For each view (η and ϕ) the *fast-or* signal of the

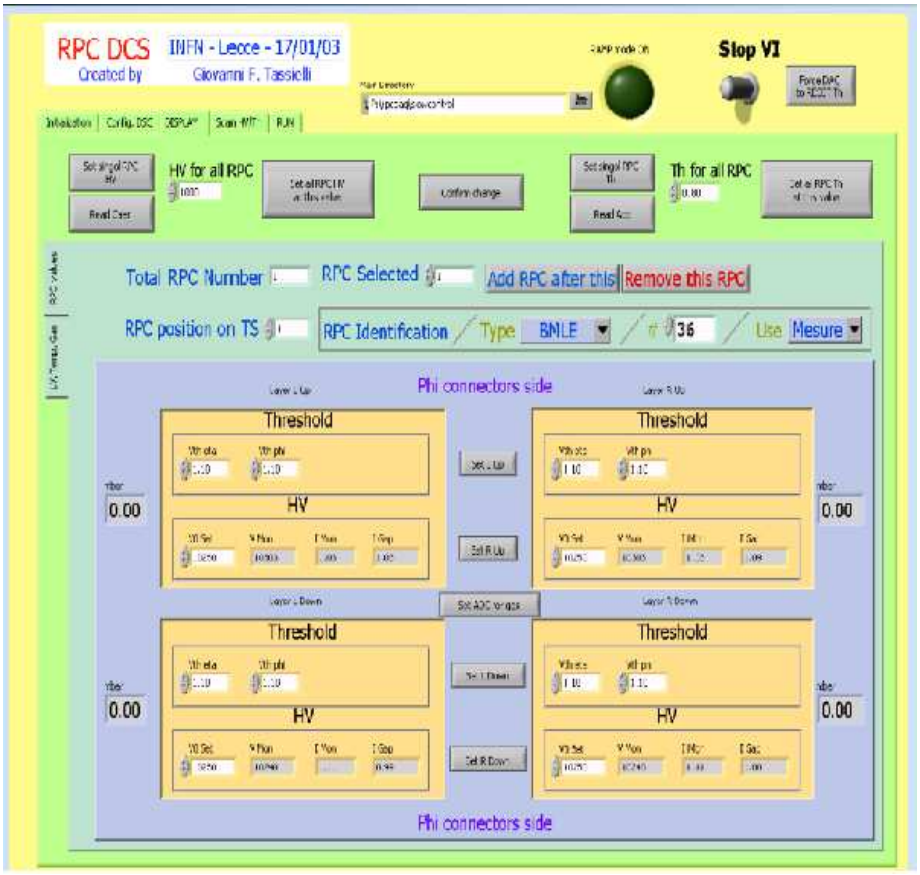

Figure 4.6: *GUI of the DCS of the ATLAS RPC test stand in Lecce.*

banks reading out strip panels of the same trigger chamber are logically OR-ed after ECL-NIM level conversion. This corresponds to 4 prompt signals per view and the coincidence of all these signals defines the first level trigger. This choice allows to have a uniform cosmic ray coverage also in presence of a trigger chamber with a moderate number of dead channels. If for each view the total number of trigger chamber banks containing at least one hit is in the allowed range (N_{min}, N_{max}), all the banks are read-out and the events is recorded. N_{min} and N_{max} are chosen according to different requirements on the tracks crossing the station in order to reject events with high hit occupancy due to showering cosmic rays or to correlated pick-up noise.

4.3 Offline Analysis

Offline analysis of the collected data is performed using a C++ Object Oriented framework. Cosmic ray tracking is accomplished by a OO pattern recognition and fit program developed to this purpose.

The offline program reads and decodes the test stand data, checks data integrity, performs time and space clusterization of the RPC strip hits, applies the desired geometry transformation and alignment parameters (reading from networked database) to the decoded digits.
First step in the offline work is the clusterization. For multiple adjacent hits in time a single hit with a time equal to the first hit in the cluster is selected. Following hits can be related at signal repetition or reflection, in this way very rapid hits suppression is performed. More important is the space clusterization. At adjacent hits in space a cluster with the right geometric position in the test stand frame is associated.

The flow is then transferred to few different tasks which take care of monitoring all the relevant RPC variables, the DCS information and display the events.

For each panel many plots on detector response are built. The most important are collected in a file were at each read out panel a single page is dedicate, which it contain: the hits repetition in time (time cluster size), the strips profile, hits time distribution, the hits multiplicity, the cluster multiplicity and the cluster size. Fig.4.7 shows an example of this page.

Summary plots of *hit multiplicity*, *cluster multiplicity*, *cluster size* and *hit repetition rate* as a function of the read out plane in the test stand are also inserted in the first page of the monitor file (fig. 4.8). In this way eventually a read out panel which present same problems can be immediately identified.

Bidimensional hit histogram relative at each gas volume under test are inserted at the end of the file. An hits is added to the histogram if η and ϕ strips are present at the same time taking into account signal propagation time in a single event. In this way hot spots inside the gas volume or noisy strips can be easily found (see fig. 4.9).

A parallel task perform similar operation on data coming from the DCS events embedded in the raw data. Plots of the environmental parameters and of the main detector parameters are built and included in a dedicated file. Fig. 4.10 shows examples of this plots.

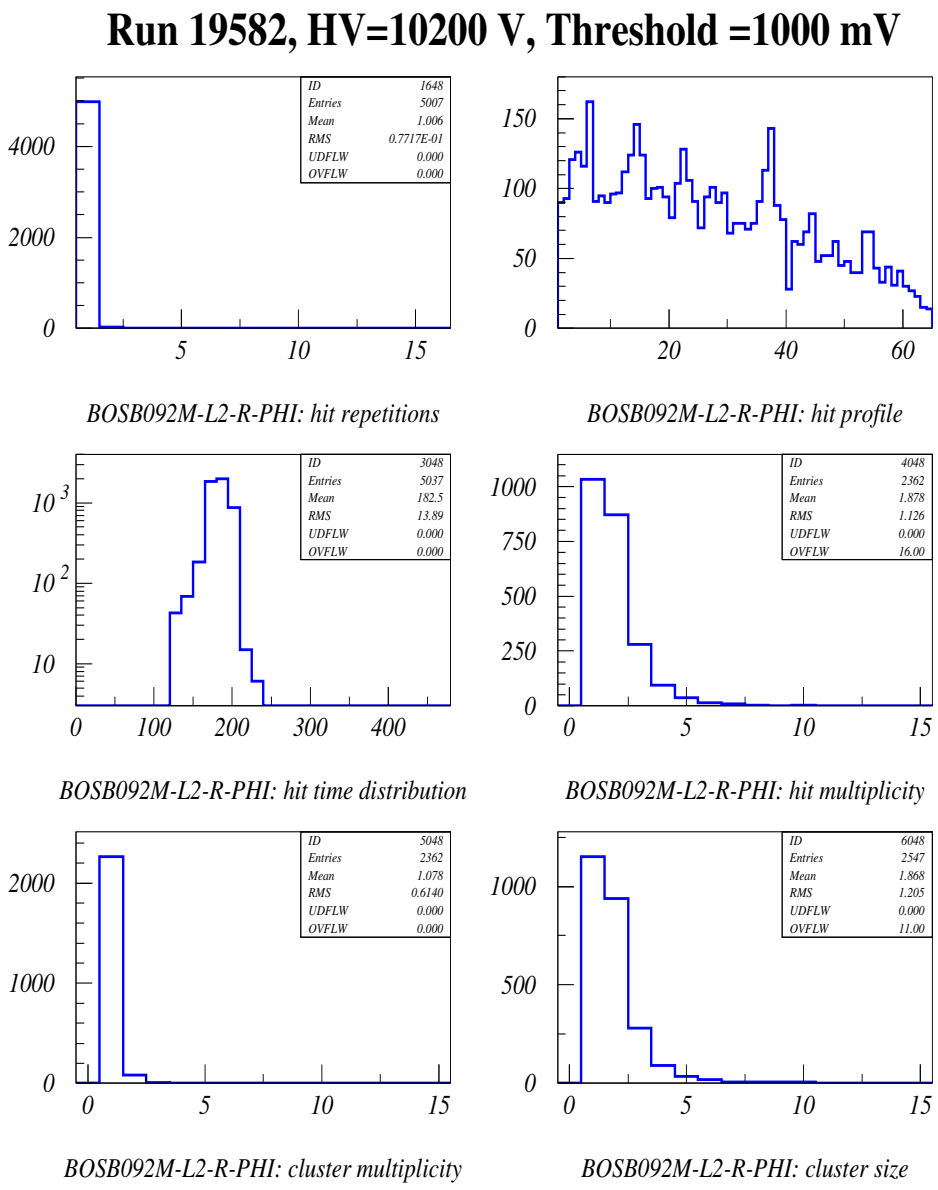

Figure 4.7: *Fundamental monitor plots relative to a single panel, collected into the read-out monitor file.*

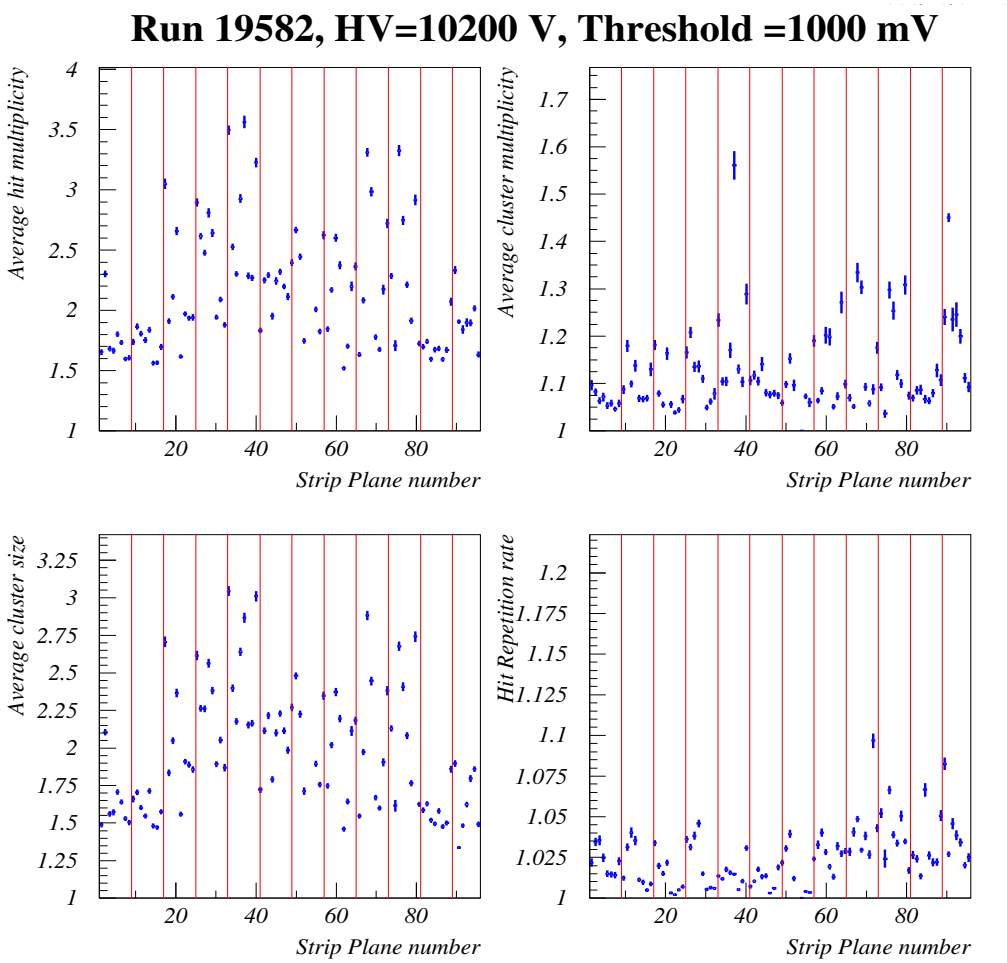

Figure 4.8: *Summary monitor plots collected into the read-out monitor file.*

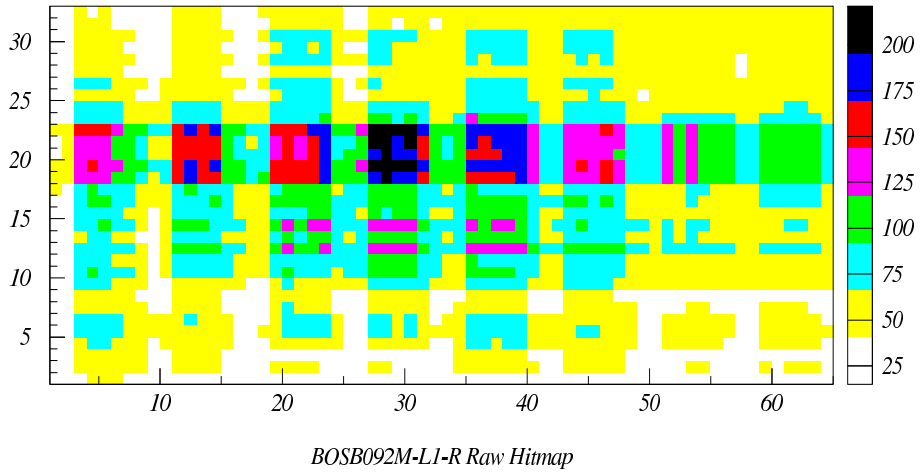

Figure 4.9: *Bidimensional hits distribution, a set of six noisy strips can be observed in the central position.*

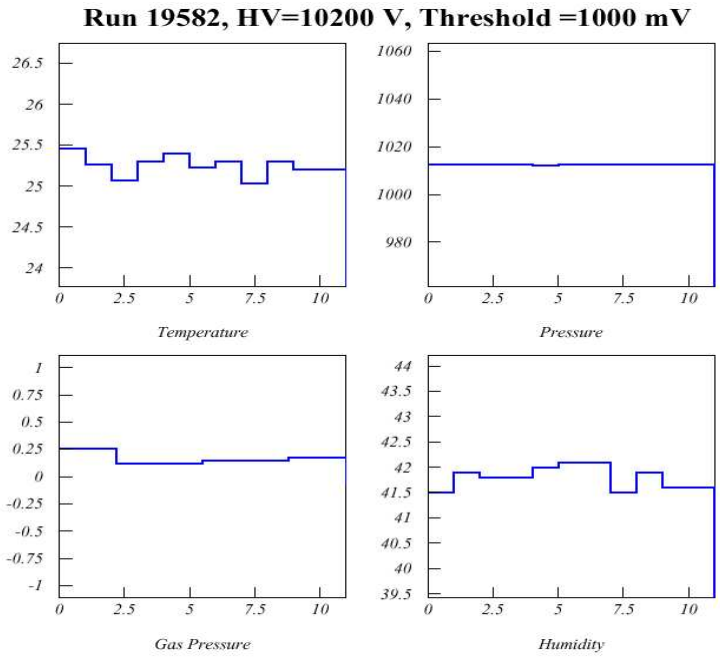

Figure 4.10: *Environmental parameters as function of data acquisition time in absolute scale (Data relative at a single run).*

At the end of the monitor operation a pattern recognition algorithm and track fitting procedure is performed. From the trigger units, three panels with only a cluster are selected and straight tracks candidate (in both η and ϕ projections) are built. At this point the track candidate is extrapolated on the other trigger chamber panels and hits intercepted in a confidential window are added at a the list of track cluster candidates. At the end all selected cluster are added to the track and fitted.
Track reconstruction for bidimensional efficiency plot (*radiography*) use all read-out plane in the test stand to construct the track. A detailed monitor on the tracks quality is performed. Distribution of hits in tracks, χ^2 and pulls of the tracks are made and stored. Moreover in order to check the uniformity of cosmic rays acquired distribution of reconstructed track slopes and impact parameter are built. All these information (see fig. 4.11 and fig. 4.12) are added at the *efficiency file* which collect all information on RPC efficiency performances.

Typical track resolution achieved by the test stand is about 10 mm. An example of residual distribution is shown in fig. 4.13.

The tracks are then extrapolated to the RPC modules being tested to measure the local efficiency and other parameters of interest as the cluster resolution and sizes, noise etc..
To compute the read out plane efficiency for each event the reconstructed track is extrapolated on the plane under test, if a fired strip is find in a small region ($\pm 1 strips$) around the strip selected by the track then the plane is declared efficient, cluster not related to reconstructed track are defined "noisy". A gap is defined efficient if for an extrapolated track at list one of the two read out plane of the gap is efficient or in other words the gap efficiency is the or of the efficiency of its relative strips plane. The electronic efficiency is then the ratio between the gap efficiency and the read out plane efficiency. If the electronic efficiency of a strip is below of 70% the strip is defined a *dead strip*. A list of dead strip is made with this criteria and stored in the MySQL DB.
Simultaneous distribution of the efficient cluster size, noise cluster size and the distribution in space of the noisy cluster are performed. Moreover the position of the panel respect to the test stand frame is calculated using the residual distribution. A gaussian equation is used to fit the residual distribution, mean value is related to the relative panel position while the spread of the distribution represents the resolution of the panel. Is this a very useful feature because is possible to insert the obtained mean value

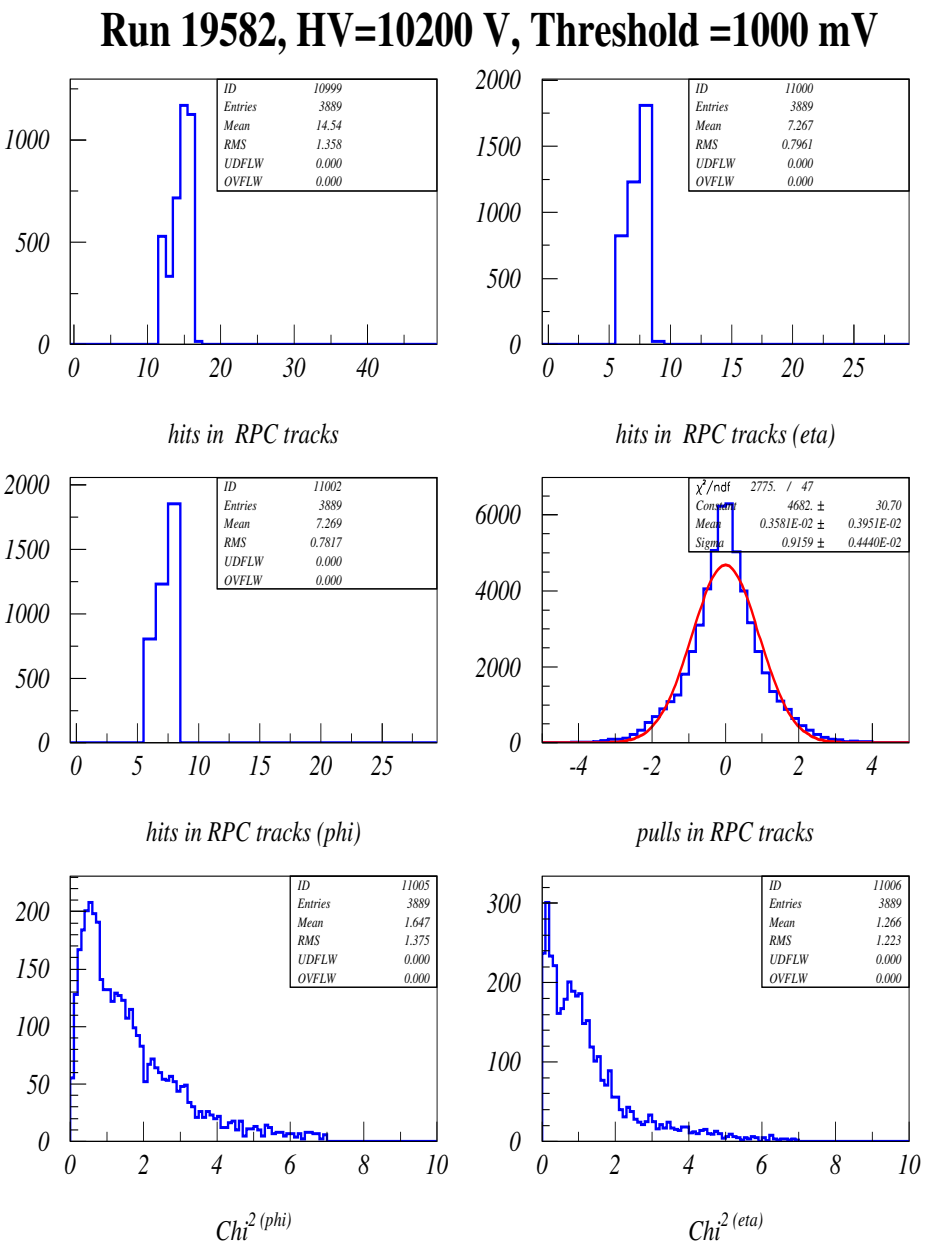

Figure 4.11: *Tracks quality monitor: number of hits in track, χ^2 and Pull distribution are plotted.*

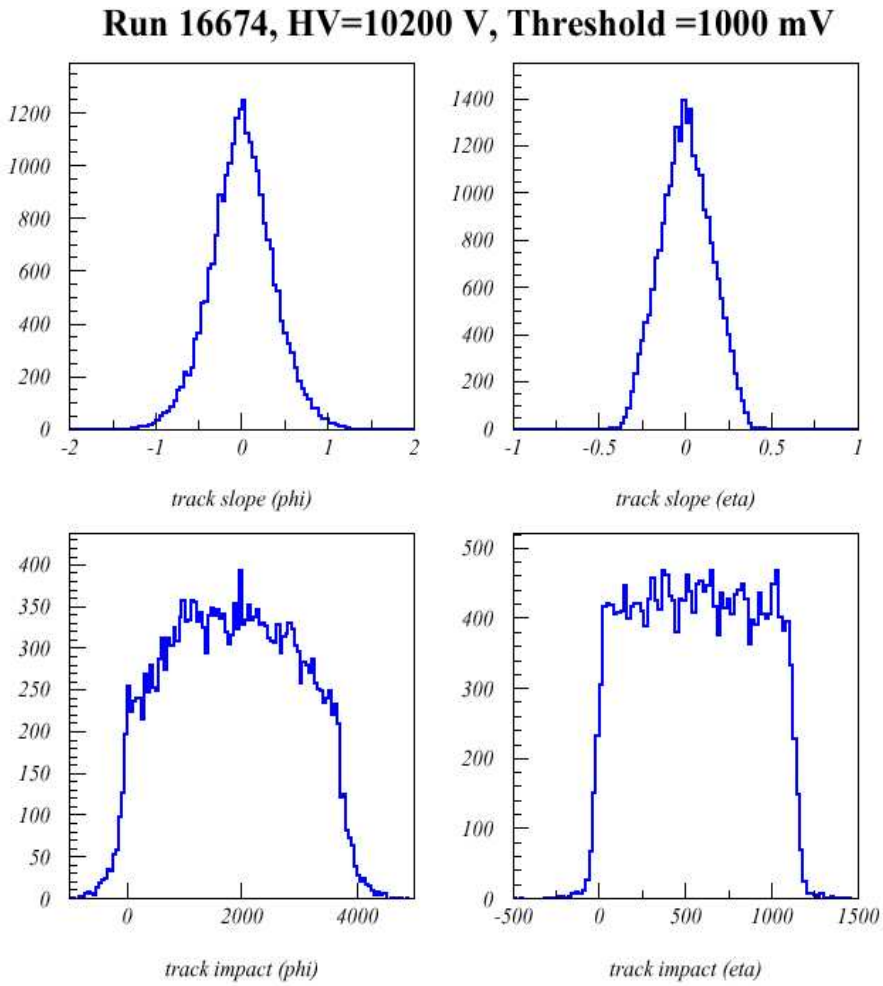

Figure 4.12: *Track slopes and impact parameter for both ϕ and η view for a single run.*

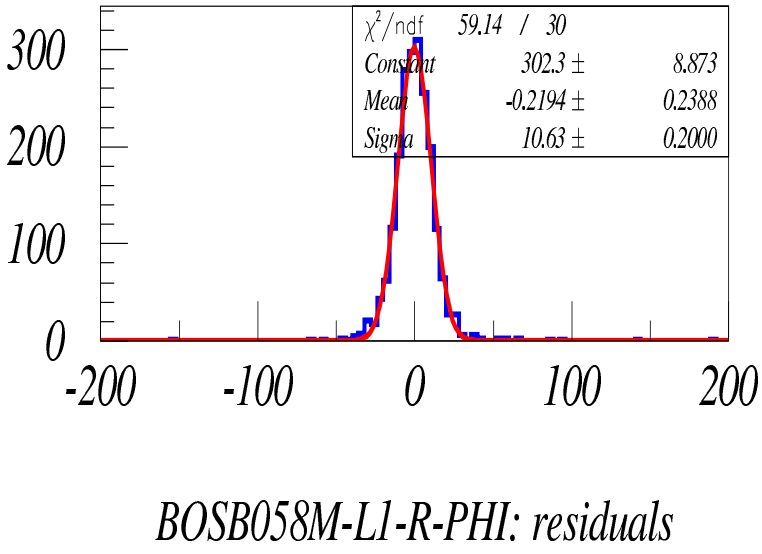

Figure 4.13: *Track resolution on a strip panel under test.*

in a dedicate database to correct the selected initial theoretical geometry and correctly align pack chamber. This allows with an iterative mechanism, to minimize the residual obtaining the right plane position and the right efficiency measurement. At the end of data taking all data of each group of test are reanalyzed with the best geometry obtained (in a single step given the DB organization of the runs).
Dedicated task provide to collect all this information and create a dedicate page for each panels under test in the *efficiency file* (see fig. 4.14).

As for the monitor summary plots are inserted at beginning of the efficiency file. Plane, Gas volume, electronic efficiency, average value for size of efficient and noisy cluster, mean value of residual distribution and resolution size are plotted as a function of read out plane. Fig. 4.15 and 4.16 shows an example of this summary: gas volumes and read out planes with problems can be easily identified from this page.

This framework is reliably working, with minor interventions and improvements, since almost one year, in automatic mode. About 10^8 events have been processed at a speed of about 300 events/sec on a 3GHz Pentium IV Linux machine running Red Hat 7.3.

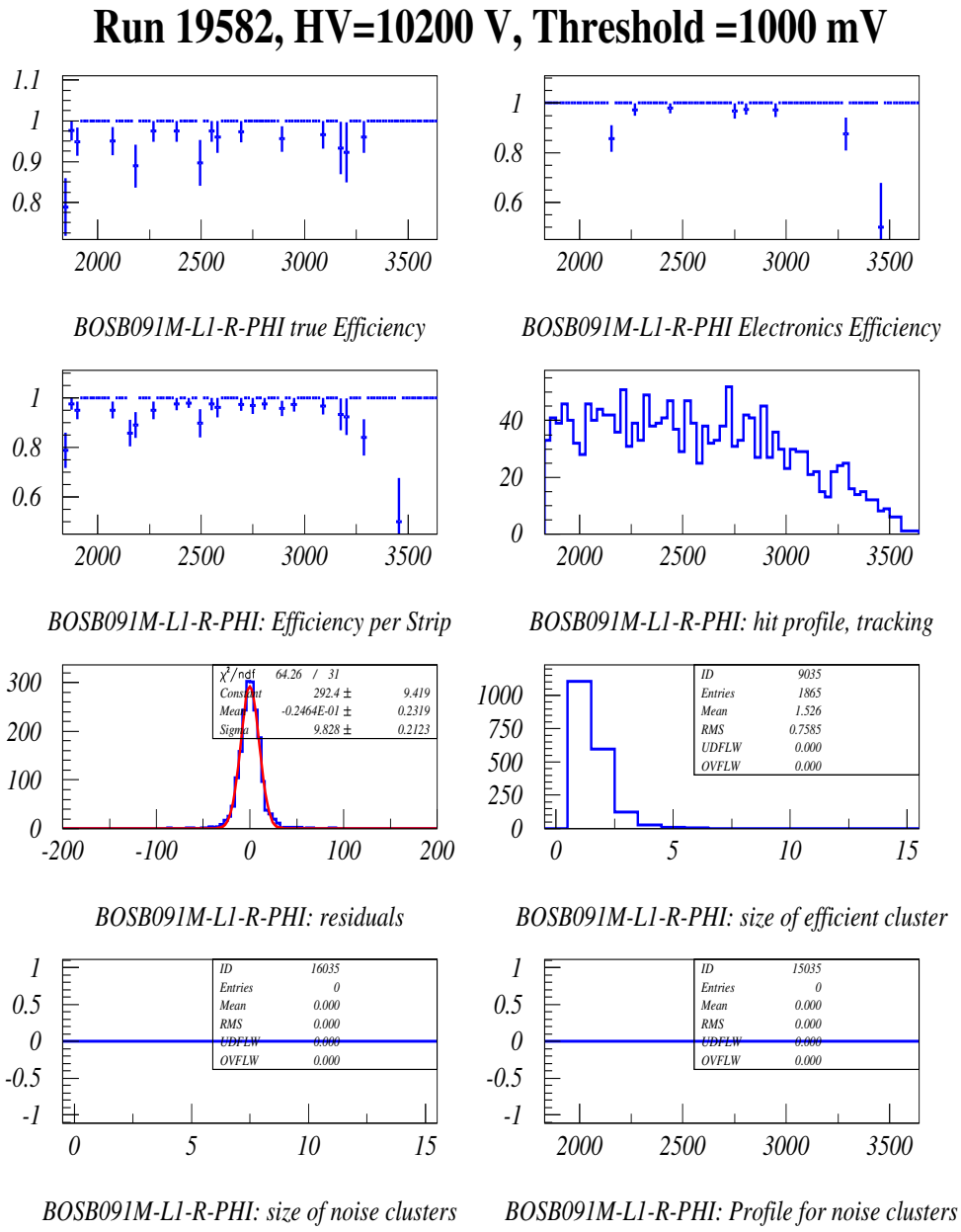

Figure 4.14: *Standard page for efficiency file relative to a single panel.*

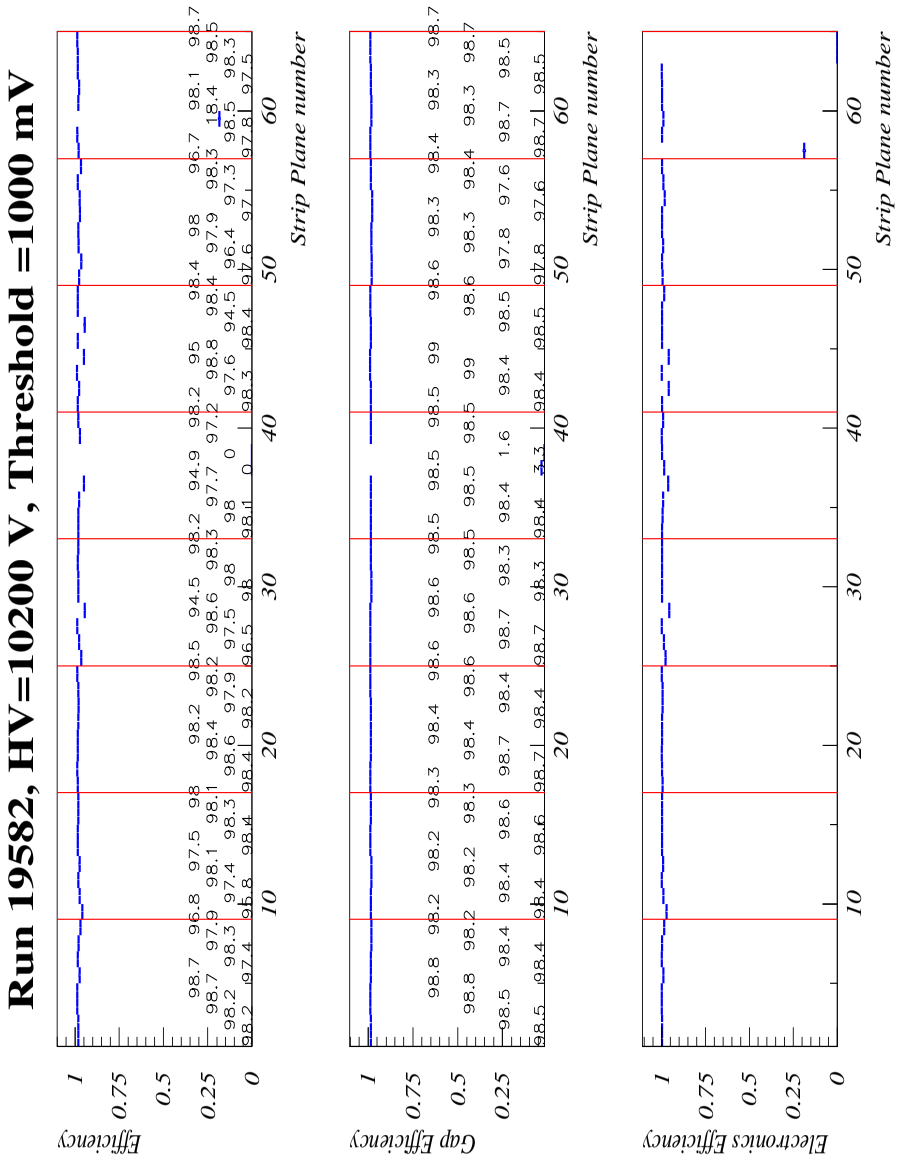

Figure 4.15: *Summary plots in efficiency file, from top: Panel efficiency, Gas Volume efficiency, Electronic efficiency.*

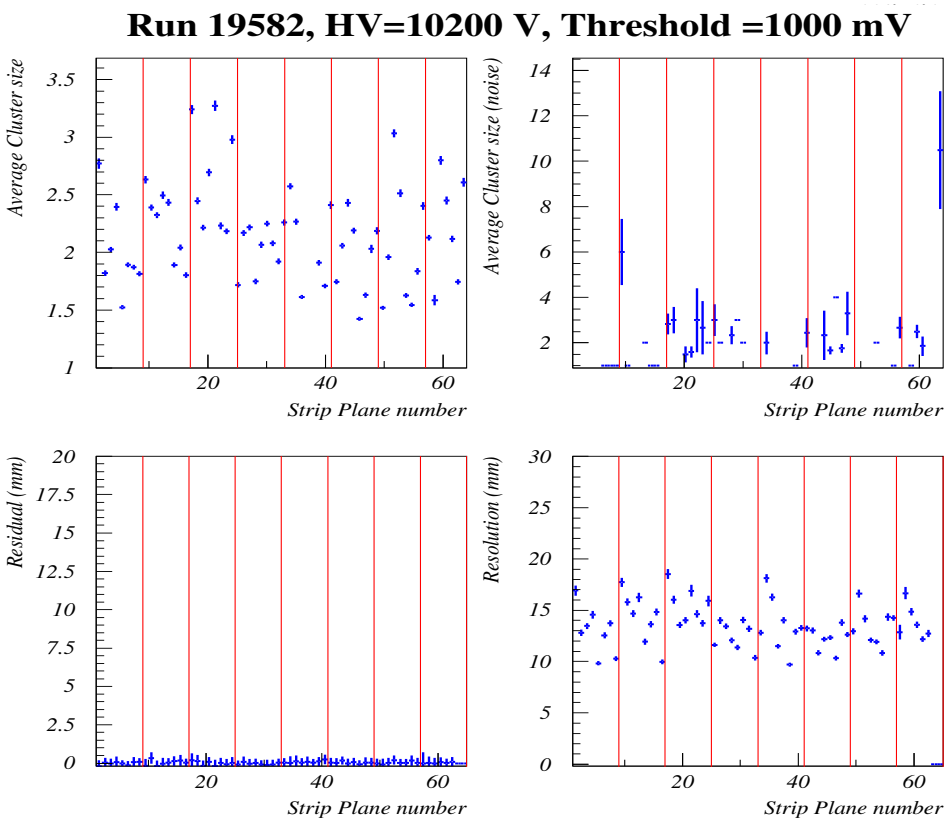

Figure 4.16: *Summary plots in efficiency file: Efficient cluster size, Noisy cluster size, Residual and Resolution.*

4.4 Test Performed

4.4.1 Data Taking

Data Taking is divided in short runs, each one characterized by a set of parameters as trigger/run type (cosmic, noise, threshold or high voltage scan), RPC module identifiers, threshold and high voltage setting parameters. The whole test procedure takes about 24 hours per group starting after about two days of gas flowing. The gas is flushed in the modules at relatively slow speed, about one gas volume exchange every 2 hours, in order to ensure a laminar flow. During this preliminary phase the high voltage connectivity to the electrodes is checked by measuring the inter-electrode capacitance, the front-end current absorption is measured, and the front-end channel connections are verified by an electrical pulse test procedure. The high voltage is applied with a slow ramp-up (about 2 V/s) given the large capacitance of the system in order to have a smooth chamber HV conditioning. About 220 runs are acquired for each group of test for a total data acquired of about 3 Gigabytes. Usually 20 runs are dedicated to front end checks with pulser test, 50 run are dedicate to I-V characterization, an equal number to efficiency measurements, 20 for the noise measurements and the remaining on the radiography. More than 300 GBytes of data during 18 months of test have been collected at the Lecce test stands. Finally the automatic measurement sequence starts and lasts about one day. The test ends with the chamber gas leak test, performed independently for each layer, consisting in monitoring the gas volume differential pressure for about 2 hours. Sensitivity is of the order of 10^{-4}mbar $\cdot$ liters/sec

During all the data taking the environmental parameter are constantly monitored as shows fig. 4.17.

4.4.2 Quality Assurance tests

The use of a database make it possible to directly access the runs belonging to a particular sequence (e.g. a plateau scan, or a scan of single rate measurement vs. high voltage). When a sequence of runs finishes, a unix daemon starts processing the results of all these runs, automatically building a series of information relative to the sequence (e.g. the RPC efficiency vs. HV or I-V current).

The quality assurance of an RPC module is achieved with a series of

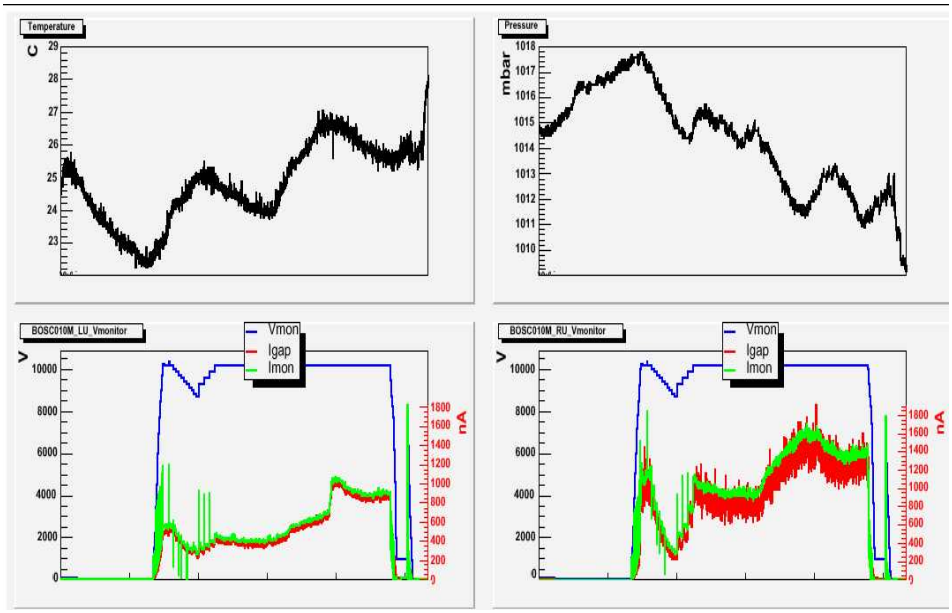

Figure 4.17: *Historical trend of environmental parameters and HV and gas volume current during a complete data taking.*

accurate measurements and tests intended to verify the correctness of the assembly and detector performance. The results of this procedure are stored in an on-line database. They represent the very first full chamber characterization and allow to extract important information monitoring the assembly line giving useful feed-back for possible improvements. In addition, in case of chamber malfunctioning or bad detector performance, the module is repaired and, if necessary, defective parts are substituted.

The quality assurance procedure consists of main certification tests and subsidiary control tests. Main tests are represented by: current versus high voltage curves, chamber efficiency and single rate counting versus high voltage and front-end voltage threshold curves and finally a "radiography". Following the test sequence adopted, first test performed is the measurement of the characteristic current vs voltage (I-V) curve. For each gas volume, via ADC is read-out the current that flow inside the gap (dark current) and directly from the CAEN is read out the current supplied from each HV

channel. We fitted the I-V curves with the function:

$$I_{gap} = \frac{V}{R_{gap}} + I_0 e^{(\frac{V}{V_0})} \tag{4.1}$$

where the fit parameters R_{gap} and I_0 can be, respectively, interpreted as the gap volume ohmic resistance and the average primary current emitted from the cathode, and the fit parameter V_0 is related to the effective gas amplification. The same equation is used to fit the value of the current distributed by the power supply, in order to check at any voltage eventually difference between the two value. Fig 4.18 shows the I-V curve for a typical ATLAS RPC gas volume.

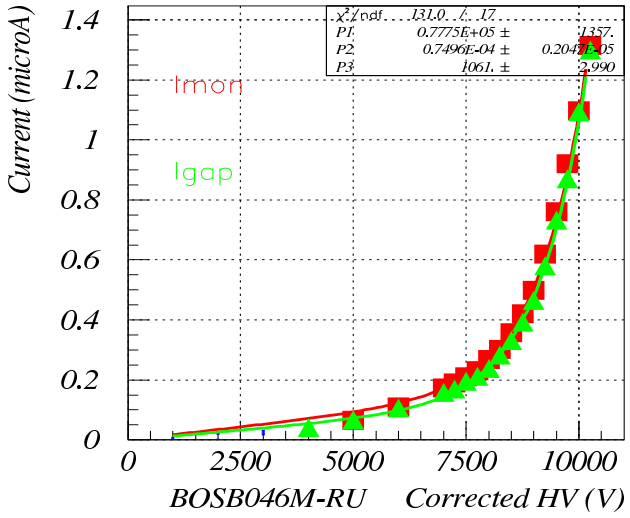

Figure 4.18: *Characteristic I-V for a ATLAS RPC gas volume.*

After that, measurements dedicated to the read-out plane and gas volume efficiency are performed. For front-end threshold between 800 and 1200 mV HV scan is performed and the efficiency is evaluated. The obtained curve are fitted with the following equation:

$$\varepsilon = \frac{\varepsilon_0}{1 + 81^{\frac{V_{50} - V}{\Delta_{10}^{90}}}} \tag{4.2}$$

where ε_0 is the efficiency reachable for infinite value of HV, V_{50} is the HV value for which the read-out plane or the gas volume reach the half value of maximum efficiency reachable and Δ_{10}^{90} measure the HV difference between the 90% efficiency and 10% efficiency point. At the same time measure of size of the efficiency cluster are performed. In this way a scan of cluster size versus HV at different threshold are made. The following equation is used to interpolate the obtained curve:

$$CS = CS_0 + CS_1 \times e^{\frac{HV}{CS_3}} \tag{4.3}$$

An example of efficiency curve and cluster size versus HV, at fixed front end threshold, are shown in fig. 4.19.

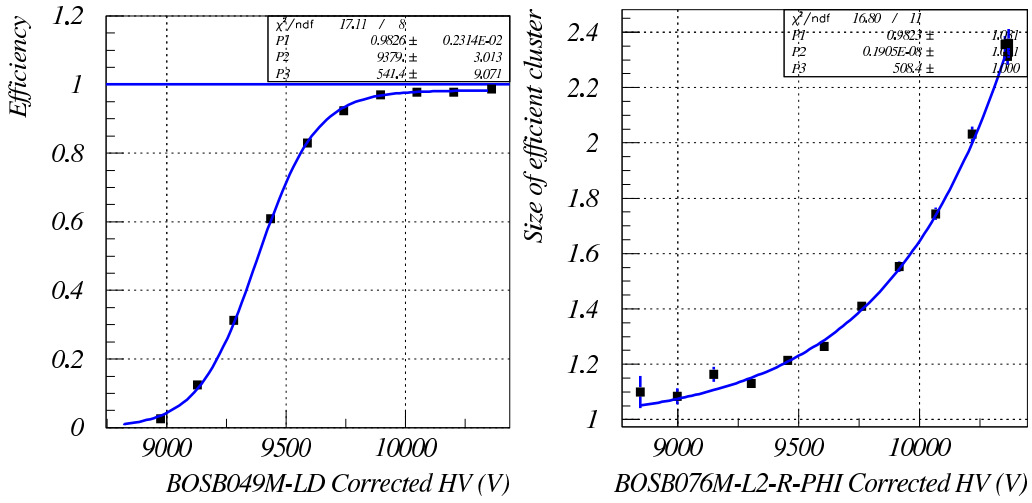

Figure 4.19: *Efficiency curve and cluster size as a function of high voltage.*

Measure of single counting rate are performed at different HV for the usual front-end threshold. The noise is plotted as a function of applied HV and the data are fitted with the following equation:

$$Noise = N_0 + N_1 \times e^{\frac{HV}{N_3}}. \tag{4.4}$$

In order to exclude local inefficiency, bidimensional efficiency plot (radiography) of each gas volume are realized. About two million of event

are needed to perform this measure on a RPC standard unit. Fig. 4.20 show an example of gas volume radiography. The dots of low efficiency are due to the grid of polycarbonate spacers which define the size of the gap.

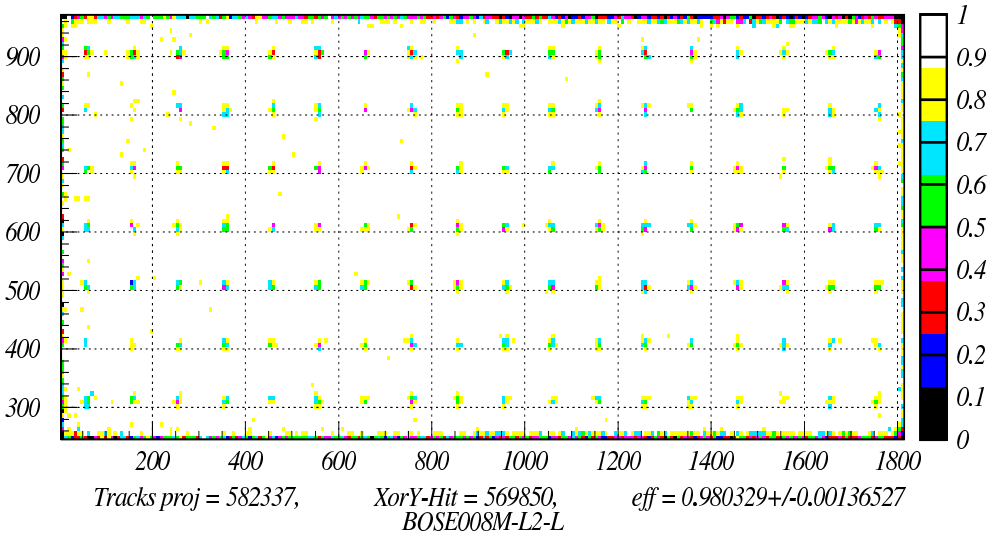

Figure 4.20: *Gas volume bidimensional efficiency.*

In order to define detector properties, relatively at a single units, during the analysis phase about 300 fit are performed for a total of about 3000 fit performed on a single group of test. All the 9000 parameters resulting are systematically stored in a well defined database for single units and global analysis studies. Everything is performed in an automatic way through use of unix daemon.

An ATLAS RPC unit is accepted only if the average strip panel plateau efficiency exceeds 96% and all gap volumes of the unit have a plateau efficiency higher than 96.5%. A maximum of one dead channel per panel is accepted. At the working point all the gap currents should be less than 4 μA/m^2 and the maximum strip panel single counting rate should be 2 Hz/cm^2. Finally, local inefficiency spots should not be present in any of the gas volumes. Subsidiary control tests take care of response at pulser, gas leaks measurements, front-end current absorption and possible drift in time of the gas volume leakage current. Finally all RPC modules passing this test protocol are certified and sent to CERN to be integrated with the rest of the ATLAS muon spectrometer detectors.

4.5 Results Presentation

All the parameters of the fits previously illustrated are automatically inserted in a MySQL database. It is composed by 17 table each one with a specific item. Two of them collect record relatively to the file acquired one from DAQ and one from DCS, information on run type, data of acquisition and main detector working parameters are stored. One table is dedicated to the alignment, position of RPC unit and relative read out panels are stored. The remaining 14 table are dedicated to fit parameters storage. In particular as we will see in next chapter similar table are used to store same fit parameters coming from different calibration. More than 310000 record with about 750 entries are stored for a total of 56.6 MBytes of data. The MySQL database has allowed the statistical analysis of the whole test results that will be discussed in next chapter. Fig. 4.21 shows the DB home page where the 17 table and number of their record are listed.

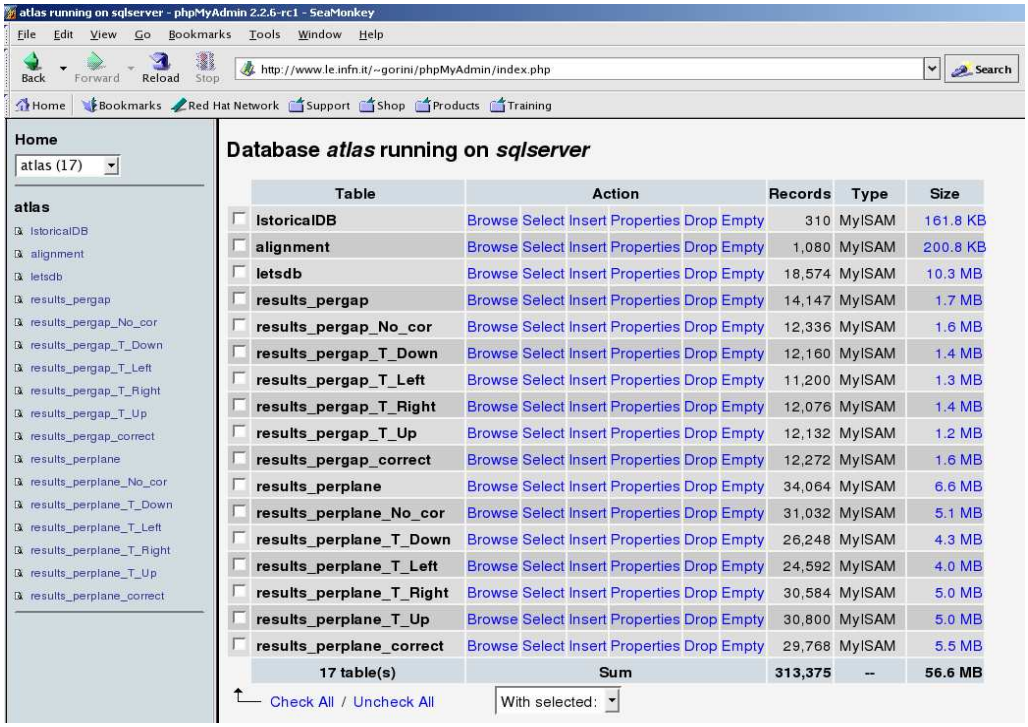

Figure 4.21: *Lecce RPC tests and results database home page.*

To allow an easily consultation of all histogram and plot produced, a simple web site based on php code has been realized (*www.fisica.unile.it/∼malice*).

Three separate sections compose the web site. The first indicates the history of the detector, since the production to the delivery to CERN.

The other two sections are organized for test group. First of these contains information run by run. All the histograms related at a single run are stored, and a graphic summary of all of them is converted in a format which can be easily accessed through dynamic web pages created accessing database information. Second one contain all plots results from the detector performance analysis which will be described in next chapter.

Chapter 5

Results of ATLAS RPC tests in Lecce

5.1 Introduction

The data analysis of the ATLAS RPC tested at the Lecce facility will be discuss in this chapter. The large sample of chambers tested allows, for the first time, precision measurements of all parameters that characterize the detector. The detector performance as a function of HV and Front-End threshold was studied, moreover the dependence of the detector parameter from the temperature and pressure was analyzed. Further scope of this work is to define a working point for each detector useful for the operation in ATLAS detector. Not all 380 detector, of 23 different typology, tested in Lecce were used for these studies, but only the 204 BOS in order to have an uniform sample. This study takes advantage of MySQL database used to store the results of each test performed on each detector. The choice to fit all measurement performed with analytic curves and to store the result parameters allows us to extrapolate the characterizing parameters (*efficiency, cluster size, noise, dark current, etc...*) for all possible HV value.

5.2 High Voltage Correction for Temperature and Pressure

The RPC is a gaseous detector operated at atmospheric pressure. For this reason, variations of environmental parameters can modify the gas gain and the relative detector response. In particular this is mainly due to the variation of reduced field (E/p). To maintain a stable gas gain, is necessary modify the applied high voltage to correct such as to contrast the variation induced by change of pressure and temperature. In order to have confrontable test results for measurements performed at different Pressure (P) and Temperature (T) is necessary to rescale the HV applied at gas volume. So first analysis done regards the parameters dependence from these environmental variables.
At Lecce test stand we decided to no correct on line th HV for T e P while applying the know correction during the data analysis. In the test phase, and at the start of the global data analysis, to renormalize the HV was used the following "standard" formula [60]:

$$HV_{eff} = HV_{app}\frac{T}{T_0}\frac{P_0}{P} \quad , \tag{5.1}$$

where HV_{eff} is the effective HV seen by the detector while HV_{app} is just the applied HV, T and P are the temperature and pressure of the gas, that in our case correspond to the atmospheric temperature and pressure and T_0 and P_0 are reference temperature and pressure chosen to be: $T_0 = 293.15^0 K$ and $P_0 = 1013$ mbar. This formula makes the obvious correction that came from the ideal gas equation. To assure an effective calibration for P and T, different parameter were plotted as function of P and T. In particular the V_{50} value (see eq. 4.2) used to indicate the HV at which the detector reach the 50% of the maximum efficiency, was studied. We choose the V_{50} parameter to perform these studies because it very sensible to the environmental variation. After a correct calibration, this quantity should be independent of the environmental parameters, being it in principle, a parameter only dependent by the gas mixture, the detector gap size and front-end threshold. The V_{50} distribution for each test group was computed, and the main value, its error and the relative T and P, were used to fill the final graphs. An evident dependence of the V_{50} parameter from T and P was found, indicating a non correct calibration, fig. 5.1 and then a necessity for a more detailed formula. Fits

are not very good due to many systematic effect which are not taken into account.

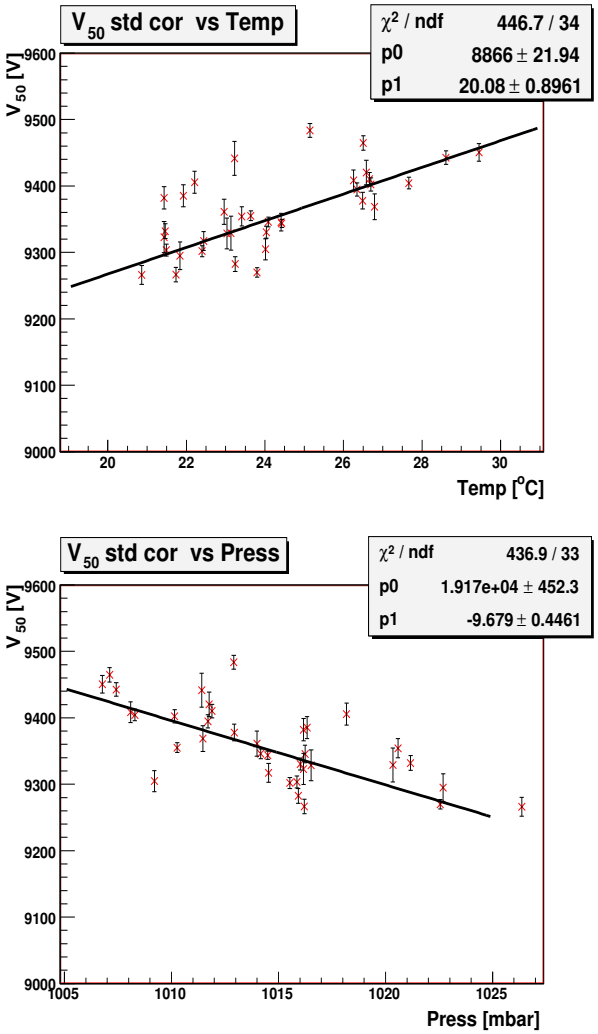

Figure 5.1: *Dependence of V_{50} from Temperature and Pressure, HV corrected for T and P with standard formula eq. 5.1*

To this purpose all the test data fit were reproduced, without any high voltage correction in order to study the natural behavior of the parameter as a function of T and P. This imply the reprocessing of the whole test station

data which takes about a week. All fit parameters were stored in new tables of the same database containing the parameters obtained with standard formula corrected HV. This new data shows, as expected, that the RPC reach the top efficiency and then its V_{50} value at a lower HV for increasing the temperature and decreasing the pressure, fig. 5.2.

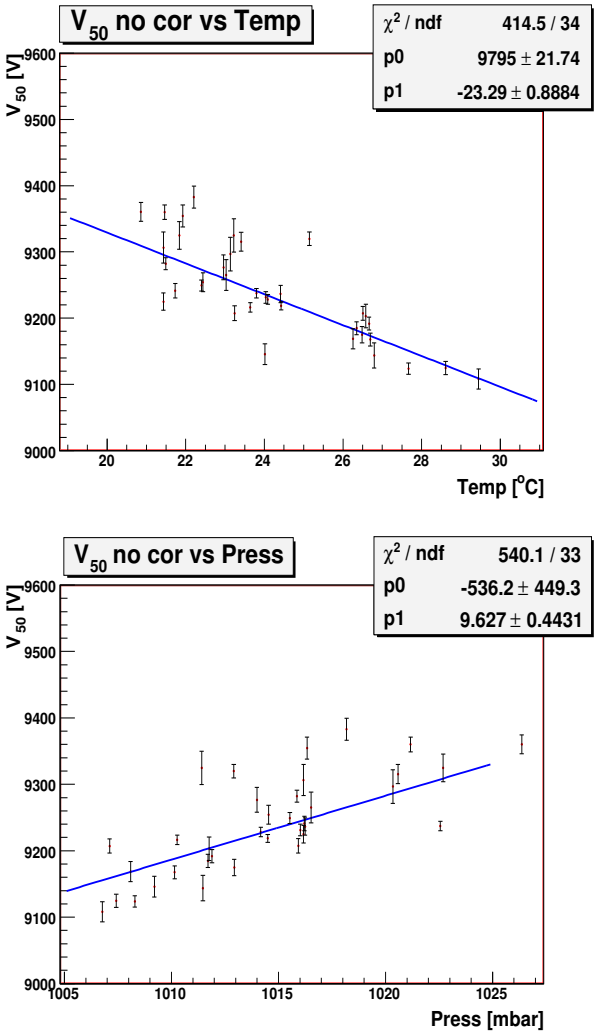

Figure 5.2: *Dependence of V_{50} from Temperature and Pressure, no HV correction for T and P.*

Looking at the previous plots, we can deduce that in our data the effect of the standard correction is an overcorrection and a new calibration making our data independent from T and P is needed.
The eq. 5.1 can be rewrite in the following way:

$$HV_{eff} = HV_{app}\frac{T}{T_0}\frac{P_0}{P} \Rightarrow HV_{eff} = HV_{app}\left(\frac{T_0+\Delta T}{T_0}\right)\left(\frac{P_0}{P_0+\Delta P}\right)$$

$$\begin{aligned} HV_{eff} = HV_{app}\left(1+\frac{\Delta T}{T_0}\right)\left(1-\frac{\Delta P}{P_0+\Delta P}\right) \cong \\ \cong HV_{app}\left(1+\frac{\Delta T}{T_0}\right)\left(1-\frac{\Delta P}{P_0}\right) \end{aligned} \tag{5.2}$$

given that for our data $\frac{\Delta P}{P_0} < 10^{-2}$. In this way, the HV is formally written as a function of the variation of T and P. If we assume that the T and P are related with the HV variation through proportional factor α and β different by the unity one can write the eq. 5.2 as follow:

$$HV_{eff} = HV_{app}\big(1+\alpha\frac{\Delta T}{T_0}\big)\big(1-\beta\frac{\Delta P}{P_0}\big) \tag{5.3}$$

the factor $\frac{\alpha}{T_0}$ and $\frac{\beta}{P_0}$ can be substituted with $\alpha`$ and $\beta`$, then one obtains the following empirical formula:

$$HV_{eff} = HV_{app}(1+\alpha`\Delta T)(1-\beta`\Delta P) \quad . \tag{5.4}$$

With standard formula α and β parameters were fixed at 1 and $\alpha`$ and $\beta`$ values were: $\alpha` = 1/293.13 = 0.0034$, $\beta` = 1/1013 = 0.00099$. To extract the$\alpha`$ and $\beta`$ parameters two different subsample were chosen : the first one, was made by all test groups having an average value of temperature, during the efficiency measurement in the range $22.5C < T < 23.5C$ while the second one by all that groups which have the average value of pressure $1011mbar < P < 1015mbar$. These value were chosen for the high number of test group in these range and because they were very near to the references value. Due to the relatively close range we can respectively consider T and P constant and look at the V_{50} behavior versus the other parameter P and

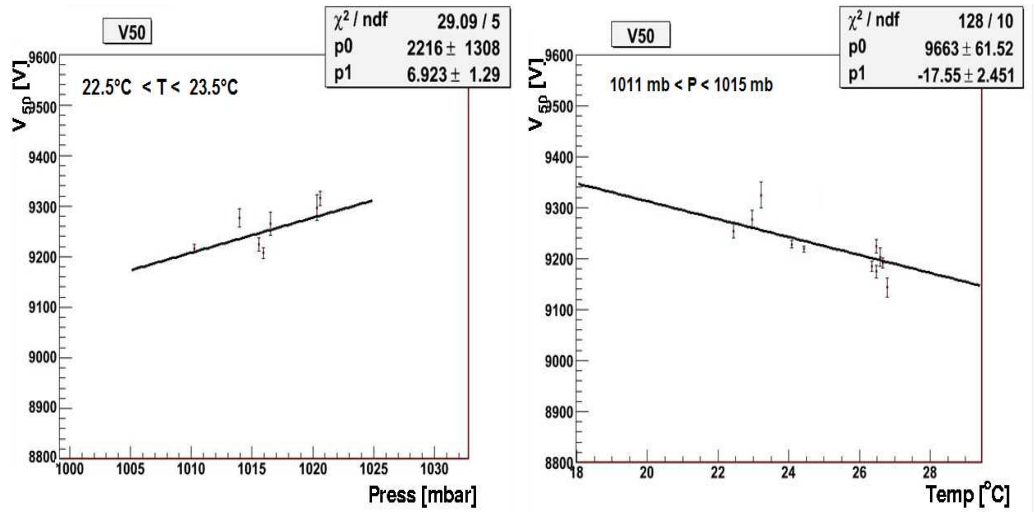

Figure 5.3: *Dependence of V_{50} from Temperature and Pressure at Pressure (right) and Temperature (left) constant.*

T. The results are shown in fig. 5.3.

The parameters relative at the slope of the fits, $\alpha' = 0.00175$ and $\beta' = 0.007$ were inserted in the eq. 5.4 and an empirical formula for the calibration of our data was obtained:

$$HV_{eff} = HV_{app}(1 + 0.00175\Delta T)(1 - 0.007\Delta P) \quad . \tag{5.5}$$

As cross-check the study has been repeated for different range of P and T obtaining similar results.
Is interesting to compare the equation obtained with our data, with the relative standard formula. If we consider the large error that affect our results, we can said that the value obtained for β' is compatible with the previous, but this is not true for α'. No specific explanation of this result has been found up to now, different hypothesis are under investigation, in particular correlation between temperature e pressure.
At this point all HV values were corrected using eq. 5.5, reprocessing again all the data. The relative fit parameters were stored in a dedicate database tables. Finally the same plots were made with the data corrected for T and P with the empirical formula. As results from the fig.5.4 the V_{50} shows

no dependence from temperature and pressure indicating that the empirical formula is sufficient to remove any dependence from these environmental parameters.

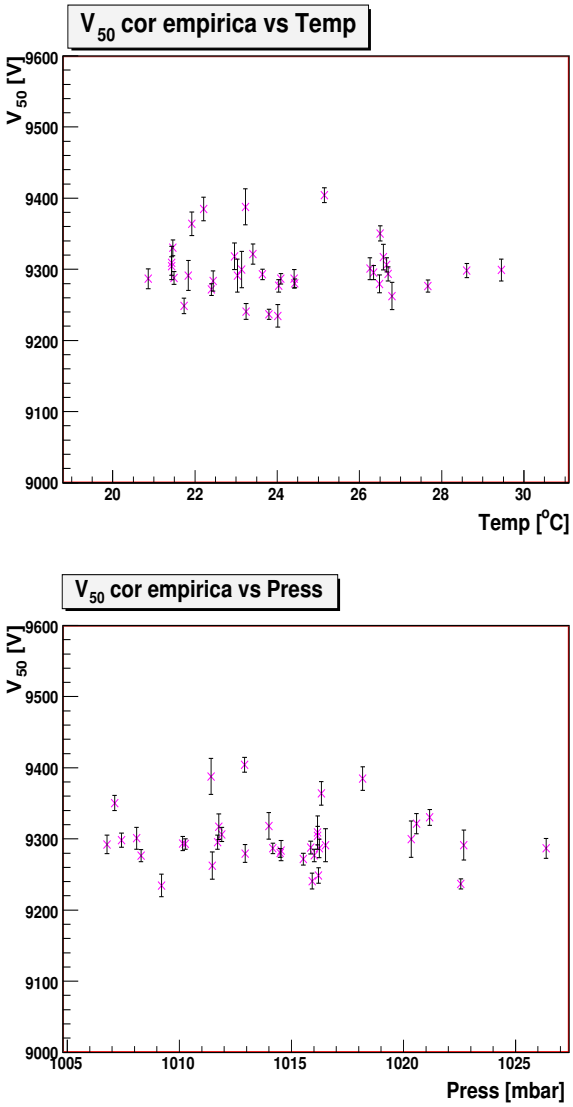

Figure 5.4: *Dependence of V_{50} from Temperature and Pressure, high voltage corrected with the empirical formula (5.5).*

All the results that will be shown in the following of this chapter have been obtained with data corrected with the eq. 5.5.
Differently from the top efficiency and V_{50}, the V_{10}^{90} parameters do not shows any dependence from the temperature and pressure. This is due to the fact that the V_{10}^{90} is a difference of two high voltage point, and the difference remove all the effect.
Some small effect due to an eventual difference of test temperature at V_{90} and V_{10} could remain but it is of the order of a few volts compatible with the error of our measurements.
Fig. 5.5 show the V_{10}^{90} as a function of pressure without (left) and with (right) T and P correction, no evident difference appear. The same results is obtained plotting the V_{10}^{90} as function of the temperature.

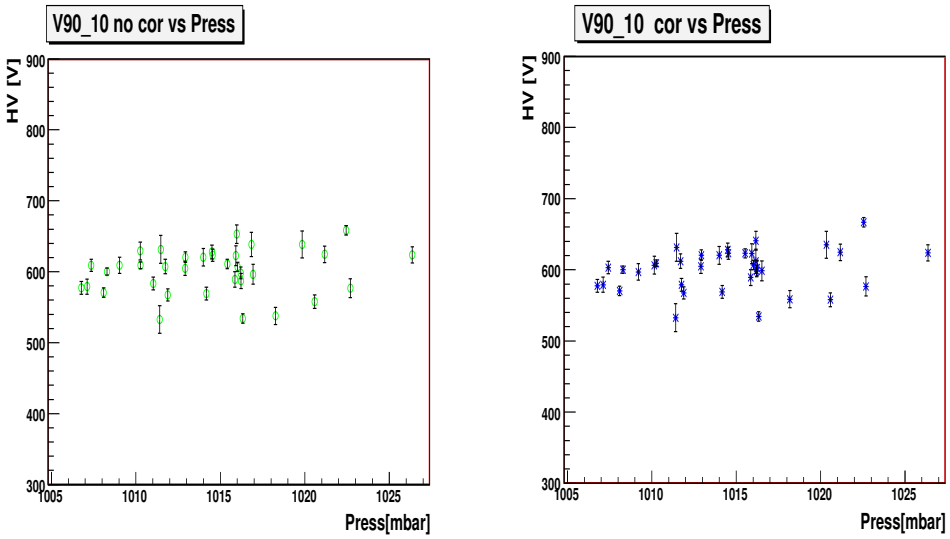

Figure 5.5: *Dependence of V_{10}^{90} from Pressure without P and T correction (left) and with empirical correction (right). No evident difference appear. Same results is obtained studying the behavior of V_{10}^{90} as a function of the temperature.*

5.3 Gas Volume Efficiency, Electronic Efficiency and Plane Efficiency

As explained in chapter 4, a gas volume (gap) is declared efficient if in correspondence of an extrapolated track, on the active volume, at least one of the two strips (η or ϕ) produces a signal removing in such a way most of the electronic inefficiency given that the two η and ϕ signals are due to the same avalanche. The efficiency of each gap was measured as function of HV at five different front-end threshold (800 mV$\leq V_{th} \leq$1200 mV).
As already said in eq. 3.2 the physical threshold V_{ph} is directly related to a negative voltage V_{th} applied on the front-end discriminator. From now when we will use the "threshold" term, we indicate the absolute V_{th} value, then at lower V_{th} will correspond an high value of V_{ph} and viceversa.
The ε_0 in eq. 4.2 denote the maximum efficiency reachable by the single gap for an infinite value of HV. For infinite HV the top efficiency value (ε_0) is strongly dependent from the front-end efficiency that depend on the V_{th}. Fig. 5.6 shows the electronic efficiency distribution at $V_{th} = 1000$ mV for each η and ϕ panels and the electronic efficiency as a function of V_{th}.

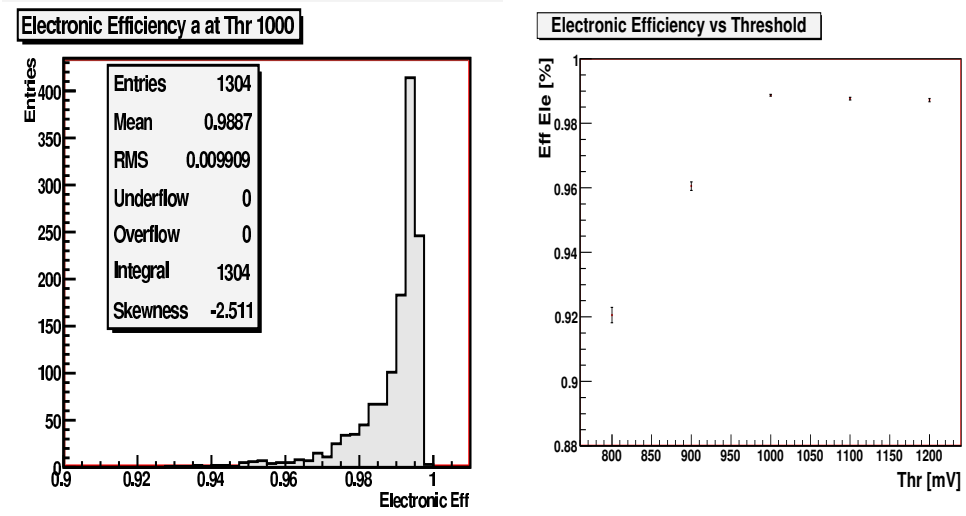

Figure 5.6: *Electronic efficiency for $V_{th} = 1000$ mV (left) and electronic efficiency vs V_{th} (right).*

The electronic efficiency increases rapidly from 800 mV to 1000 mV reaching a plateau value. Its average value is very close to one and the tail at lower values is due to the presence of few dead channel in some read-out panel.[1]
The gap efficiency, extrapolated at infinite value of HV as function of V_{th} increases with the front-end threshold as shown in fig. 5.7. Its important to note fig. 5.7 that at $V_{th} = 1000$ mV the average value of all BOS gas volume efficiency is about 98.4% well above the 97% request by ATLAS and only 5 gas volume have an efficiency belove 97% (5 on $652 < 1\%$). Gas volume with efficiency below 96.5 have been rejected.

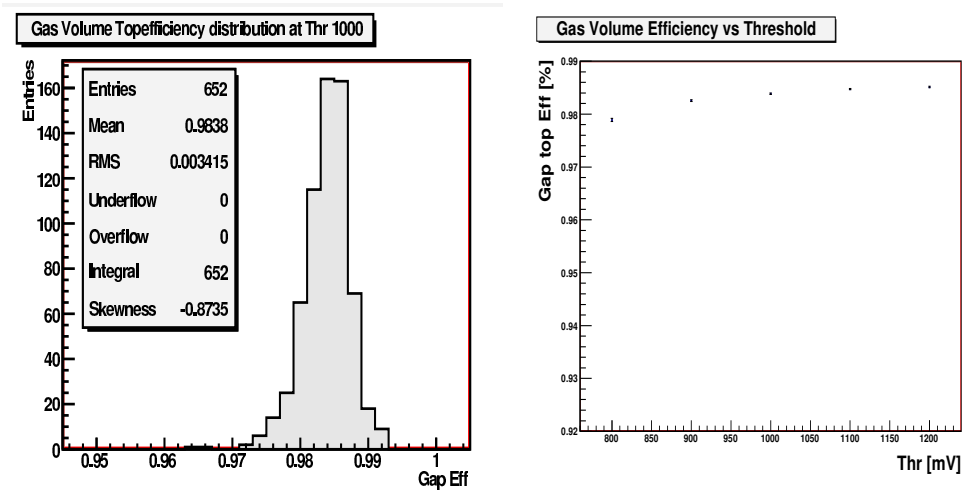

Figure 5.7: *Gap efficiency distribution at $V_{th} = 1000$ mV (left) and dependence of the average gas volume efficiency from the V_{th} (right).*

The real plane efficiency will be the product of the gas volume efficiency times the front-end electronic efficiency. No difference between η and ϕ panels have been found. Fig. 5.8 and fig. 5.9 shows the general trend of gas volume and plane efficiency as function of V_{th} for different HV value.

[1] One as to consider that a dead front-end channel contribute to $\sim 3\%$ for η strip panel and for $\sim 1.5\%$ for ϕ panel.

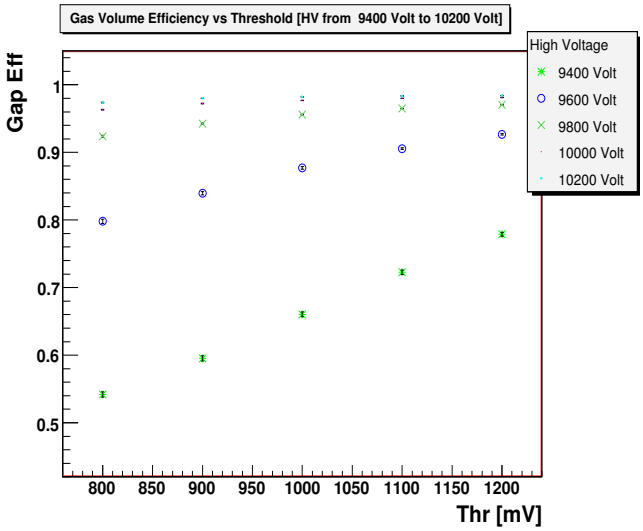

Figure 5.8: *Average gas volume efficiency as a function of V_{th} for different HV value.*

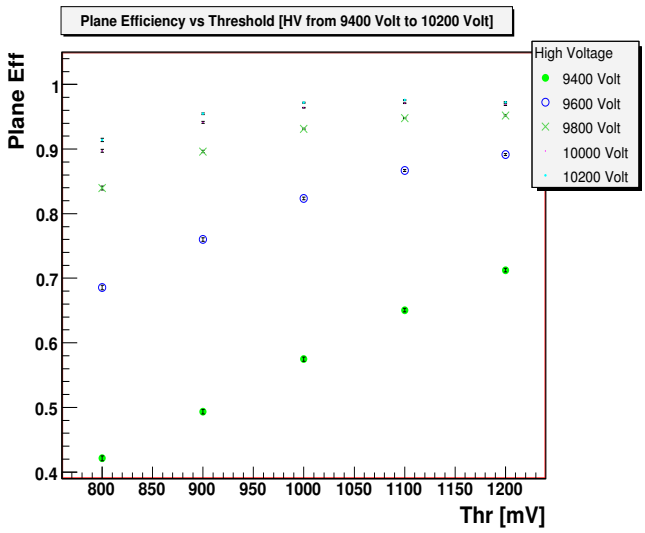

Figure 5.9: *Average strip panel efficiency as a function of V_{th} for different HV value.*

5.4 Cluster Size and Noise as a Function of Front-End Threshold

The *Cluster Size (CS)* and *Noise* (or single counting rate) are quite relevant parameters for the RPC operation. Due to the charge sharing (and eventually to cross talk) some time a single discharge in a gas volume induces charge in more than one strip that are collected in a cluster (see §4.3).

From the ATLAS requirements, the average cluster size, should be preferentially lower than 1.5 [61]. As the gas volume or panel efficiency, the cluster size is strongly dependent from the applied HV and front-end threshold. The cluster size of a single strip panel, at fixed V_{th} and as function of HV, was parameterized with the eq. 4.3. Distribution of CS for each front end threshold have been plotted for different possible HV. Beside of the average value,it is very important to check the shape of the CS distribution in order to verify the absence of abnormal distribution tails, due to multiple counts generally due at front-end electronics problems (i.e. cross-talk) rather than to the normal avalanche discharge in the detector. Fig. 5.10 show the CS distribution for all BOS strip panels at $V_{th} = 1000$ mV and HV = 9900 Volts (left) and the CS behavior as a function of front-end threshold for differences high voltage (right).

Due to the different number of front-end electronic board installed on η and ϕ read-out plane the effective threshold seen by the panels is slightly different moreover an additional film of PET interposed between the gas volume and the η panel reduce the electrical coupling, producing a small differences in detector response. In particular at fixed V_{th} the effective threshold V_{ph} applied on η panels is little higher than effective threshold applied on η producing an average CS value lower than ϕ (see fig. 5.11).

Dedicated measurements were performed in order to study the Random Noise (single rate counts) behavior. To avoid uncorrelated trigger signal is necessary to have a level of noise as lower as possible, in particular its must be lower than the expected cavern background ($10 Hz/cm^2$), from ATLAS requirements its maximum value is fixed at $2 Hz/cm^2$ [61]. As expected also the noise is strongly dependent from the HV applied at the gas volume and the front-end threshold. The same procedure used for the CS was adopted to study the behavior of the single rate counts. Noise distribution for all panels was made at different threshold and HV, and the study were performed on η and ϕ panels separately. For the same arguments explained for the CS also

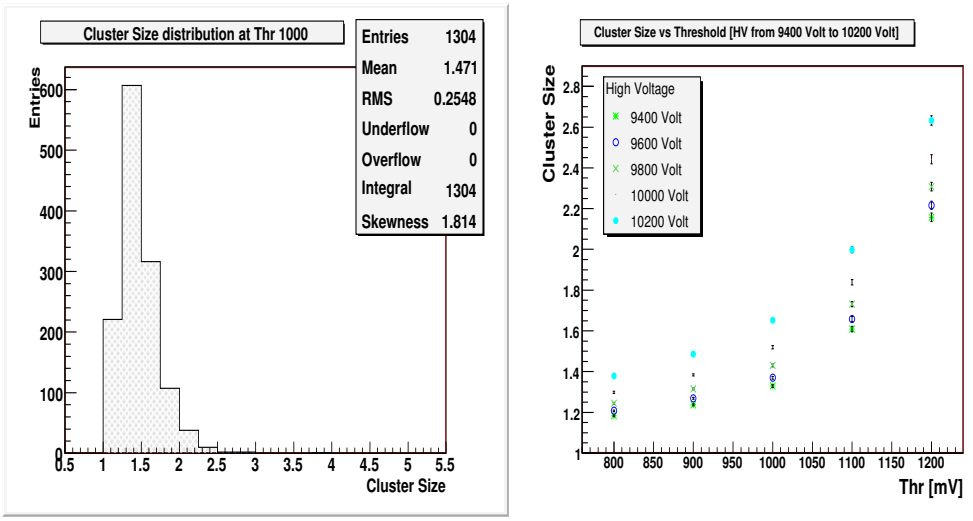

Figure 5.10: *Cluster Size distribution at HV =9900 Volts and* $V_{th} = 1000\ mV$ *(left) and average Cluster Size as a function of* V_{th} *for different high voltage values (right).*

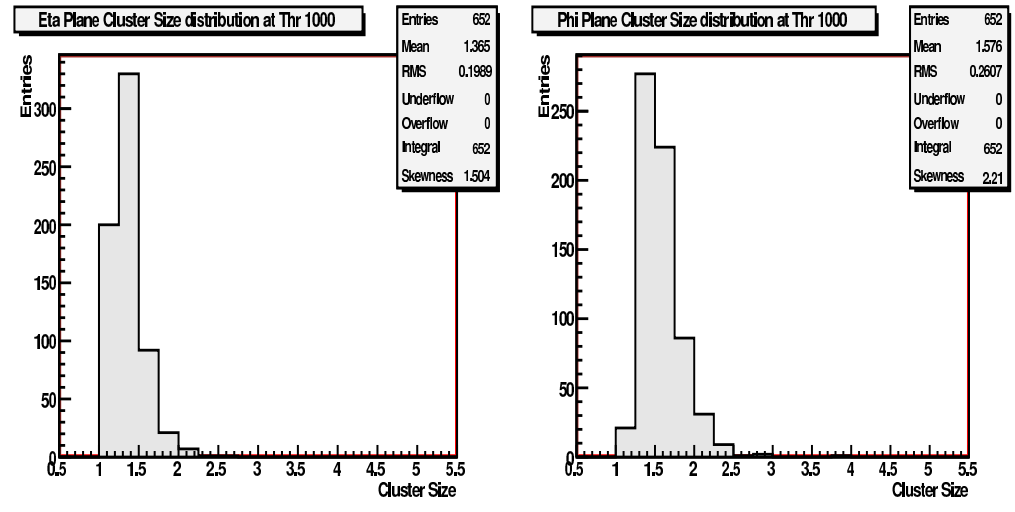

Figure 5.11: *Cluster Size distribution for* η *(left) and* ϕ *strip planes (right) at HV =9900 Volts and* $V_{th} = 1000\ mV$.

for the noise the η and ϕ shows a different behavior (see fig. 5.12), the ϕ plane are noisier than the η panels.

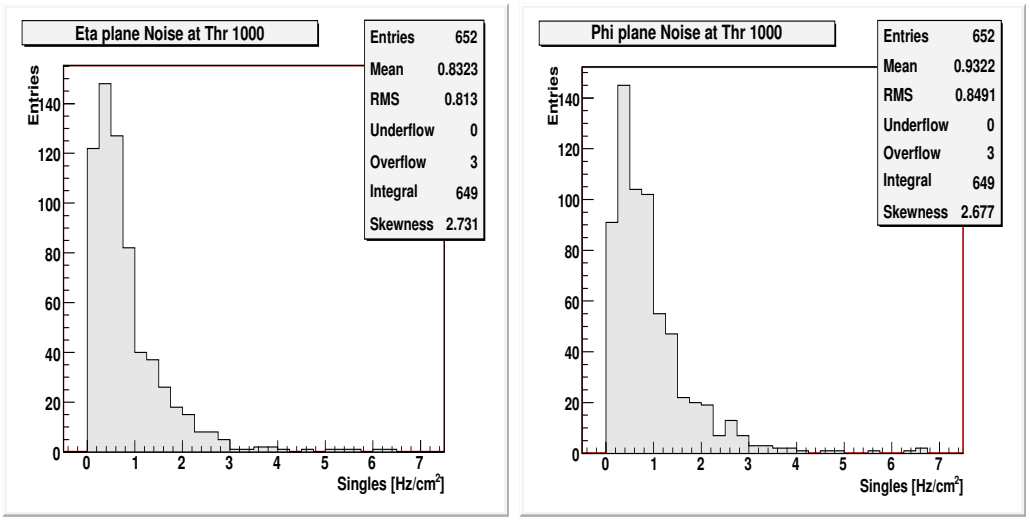

Figure 5.12: *Single rate counts (Noise) distribution for η (left) and ϕ plane (right) at HV =9900 Volts and $V_{th} = 1000\ mV$.*

Fig. 5.13 shows the noise distribution for all BOS panels at $V_{th} = 1000$ mV and HV = 9900 Volts (left) and the noise behavior as a function of front-end threshold for different HV (right).

Detector noise is also correlated at the detector dark current, more details will be given in next paragraph.

5.5 Current and Noise as function of Temperature

A variation of temperature produces a variation of gas gain modifying the development of the avalanche in the detector. Beside of this effect that interest the response in efficiency, a variation of temperature produce a variation of bakelite and polycarbonate spacers resistivity and this modify the detector dark current and random noise. Fig. 5.14 (left) shows the dark current average value at 9900 V for each test group as a function of temperature. Even if HV values have been renormalized with the empirical

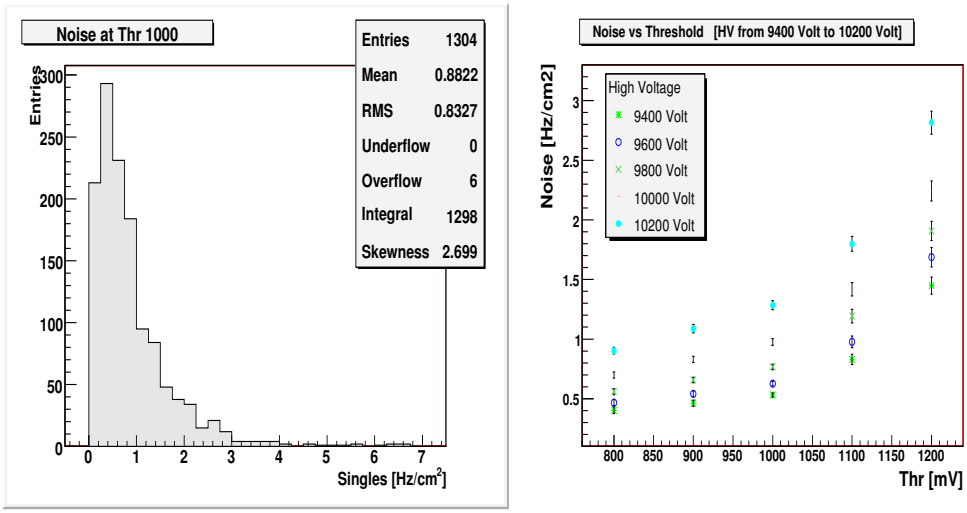

Figure 5.13: *Noise distribution at HV =9900 Volts and* $V_{th} = 1000$ *mV (left) and average Noise as a function of* V_{th} *for different HV value (right).*

formula, nevertheless a strong dependence of temperature is still clearly visible. Random noise could be interpreted as a counting due to the dark current that flow inside of the detector not correlated with the passage of a particle. For this reasons, as we expect, the distribution of the average noise value versus temperature, related at each test group shows the same behavior of the current distributions (fig. 5.14 (right)).

Due to the possibility to modify and control the temperature using air conditioners of our test stands a dedicate test was performed to better understand this phenomena [62] [63]. Only four standard ATLAS RPC unit with the usual test stand trigger were used in this test.

The test stand internal temperature was changed from about 20 ^{0}C to about 30 ^{0}C and back again in about 15 hours, taking data with cosmic rays. In Fig. 5.15, the dark currents of the four gas volumes, composing an ATLAS RPC unit, are shown versus the average measured temperature. There is a clear hysteresis in the gas volume currents which disappears several days after the thermal cycle.

In order to explore the impact of temperature on quantities related to the RPC inner surface quality, we performed a high voltage scan at the lower and at the higher temperature conditions reached, taking data with random

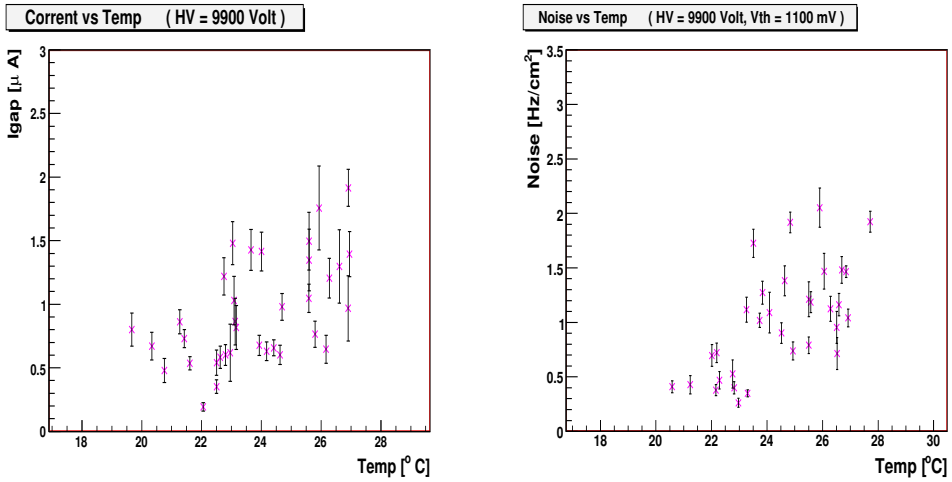

Figure 5.14: *Current vs temperature (left), Noise vs temperature (right) HV=9900 Volts and* $V_{th} = 1100\ mV$.

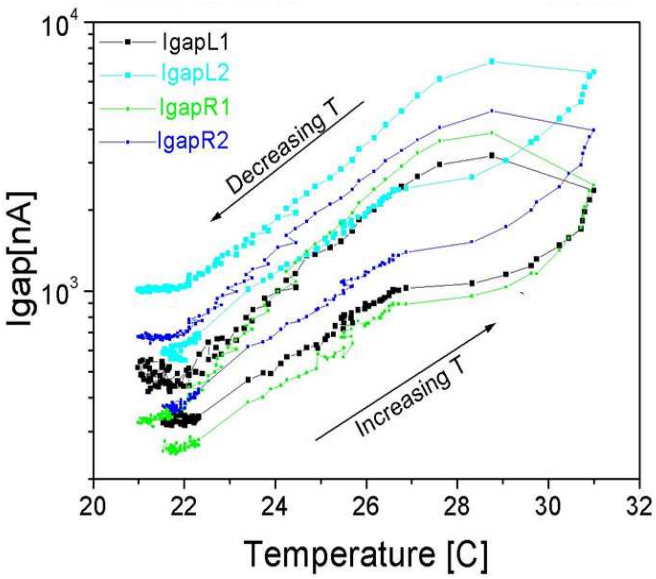

Figure 5.15: Gas volume currents evolution of one test RPC versus temperature during the thermal cycle of about 15 hours.

triggers (noise rate). This allowed us to measure the current vs voltage (I-V) and noise rate characteristics at the two extreme temperature values. The fits were performed with the usual formula eq. 4.1 and eq. 4.4. In particular from eq. 4.1 one can identify the total current as the sum of two separated contributions *ohmic* I_{ohm} and *amplification* I_{amp}. Fig. 5.16 shows the dark current and random noise for one of gas volume under test.

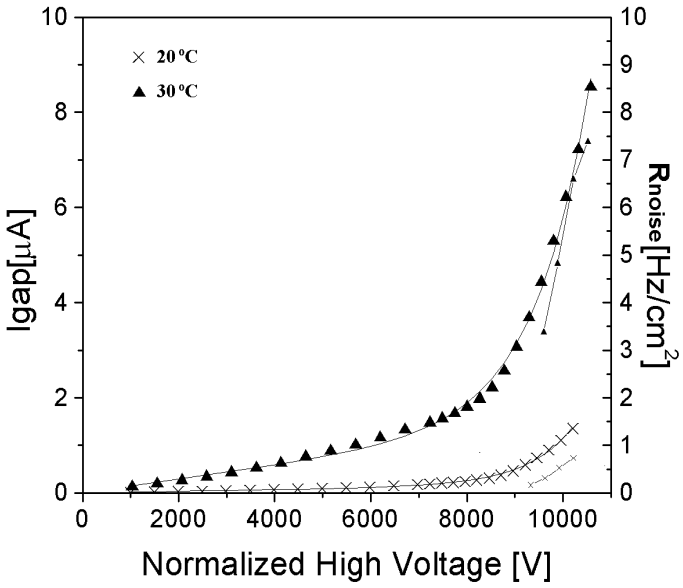

Figure 5.16: I-V (large symbols) and noise (small symbols) of one gap at two different temperatures. The superimposed curves are fit to the data.

From the analysis of all 16 gas volume tested a significant increase of both components of the current I_{ohm} and I_{amp} was observed, together with a large statistical spread among gas volumes. The strong temperature dependency of the gas volume ohmic resistance is likely related to a change in resistivity of the polycarbonate spacers and edges frame. Instead, the strong temperature dependency of the exponential components of the current is mainly due to a change in the parameter I_0, which is related to inner surface electrode quality and resistivity. The parameter V_0, instead, is not much affected by the surface quality and resistivity, but mostly by the gas gain.
The surface radiography performed with the random noise, fig. 5.17 shows that the increasing of the noise is not due to a localized point but is an

effect distributed on the entire detector surface. That is due to the changed dielectric property of the bakelite .

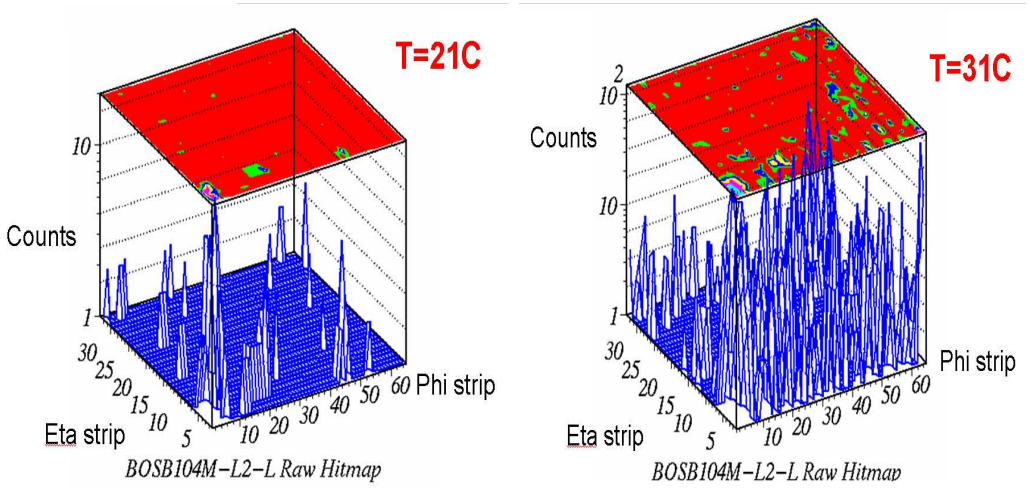

Figure 5.17: *Noise distribution in gas volume at* 21^0C *(a) and* 31^0C *(b).*

In order to better understand the dependence of noise rate from the the dark current, the noise rate R_{noise} was plotted as a function of the exponential components of the current per unit surface relative to a high voltage scans at low and high temperature (fig. 5.18). An approximate linear dependency between the dark current and the noise rate can be inferred.

This can be simply understood by assuming that the exponential part of the current is due to electron clusters produced from the cathode surface which get multiplied by the intense electric field up to avalanche saturation [64]. Each simple saturated avalanche is detected as a noise signal from the strip read-out panel. Following this over-simplified picture, we have extracted an average saturated avalanche charge of about $Q_s = 34.5$ pC by interpolating the plot with the formula

$$I_{amp} = Q_s R_{Noise}. \tag{5.6}$$

The estimated Q_s value is pretty much in agreement with the study described in [64]. During all these measurements the detector efficiency was constantly monitored and no degradation of the performance was observed. Noise rate and dark current vary exponentially with temperature, where a variation of

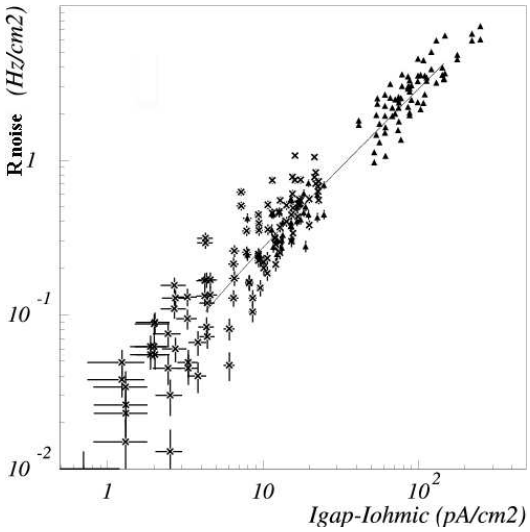

Figure 5.18: Scatter plot of all strip panel noise rate versus the corresponding gas volume current (ohmic part subtracted) of all chambers at different high voltages (9300 V, 9600 V, 9900 V, 10200 V) and at two different temperatures (20 ^{0}C crosses and 30 ^{0}C triangles). A linear fit is superimposed on the plot.

about 10^0C results in an increase of about a factor of 4 in both quantities as observed in the first general plot (fig. 5.14), within the temperature range studied.

5.6 HV Working Point Definition and its Properties

After the installation in the ATLAS Muon Spectrometer the RPC detector will be connected to the HV distribution system. Due to obvious cost reasons, each HV channel will provide HV supply at group of gas volumes variable between 12 and 24. For this reason will be necessary to set the HV such as to assure a good efficiency for all gas volume connected at each single HV channel. To this aim it is important to define and find an adeguate working point (V_{WP}) for each of the BOS chambers. The V_{WP} is same way a parameter which define the best operating voltage of the detector once fixed the threshold, ensuring the highest efficiency compatible with physics

requirements on cluster size, single rate counting and currents.

We have chosen our V_{WP} definition in the following way: *the voltage at which the gas volume reaches a fixed percentage of the top efficiency* (*i.e. from 96% to 99%*). Fig. 5.19 shows the HV distribution for V_{WP} fixed at 99% of top efficiency ($V_{th} = 1000$ mV).

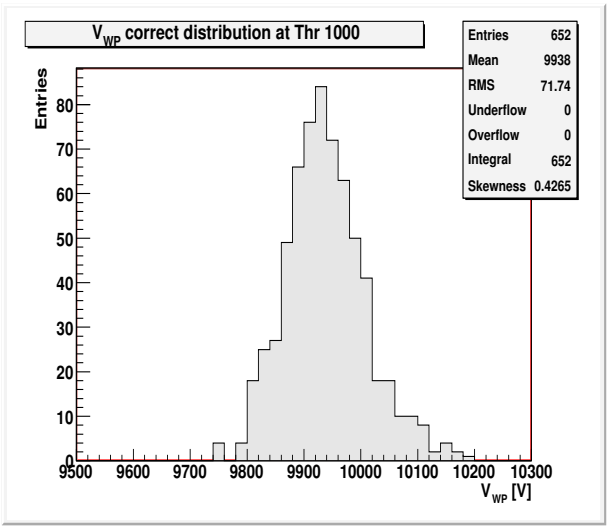

Figure 5.19: *Distribution of the V_{WP} (defined at* 99% *of top efficiency, $V_{th} = 1000$ mV).*

If it were possible to apply at each gas volume its own V_{WP} then the relative gas volume efficiency distribution will be simply the top efficiency distribution multiplied for the coefficient chosen to fix the V_{WP} . But if are forced to use the same HV value for all gas volume (or groups of gas volume as foreseen in ATLAS), the average value obtained from the distribution of HV has to be used.

Fig. 5.20 shows the distribution of the gas volume efficiency obtained applying at each single gas volume its V_{WP} (left) and applying at all gas volume the same HV (average of HV for V_{WP} distribution) (right). As expected the spread of the efficiency distribution obtained using only a value of V_{WP} for all gas volume is higher than the spread of the efficiency distribution obtained using for each gas volume is own V_{WP}.

Once computed the V_{WP} value for each gap, all relevant quantities that characterize the detector have been plotted for 800 mV $\leq V_{th} \leq$1200 mV,

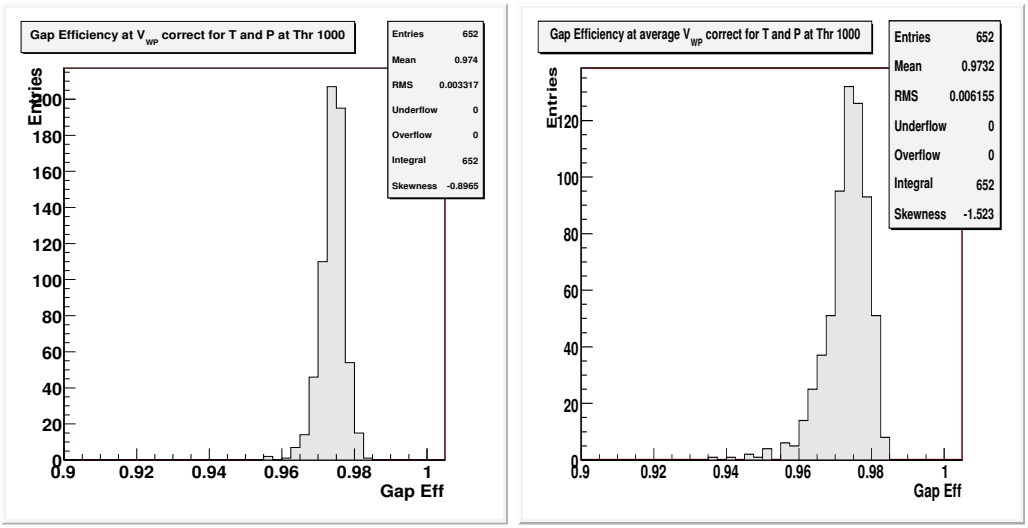

Figure 5.20: *Gas volume efficiency distribution obtained applying at each gas volume its V_{WP} (left) and applying the average value of HV V_{WP} distribution ($V_{th} = 1000\ mV$ (right)).*

at that particular value. Particular attention was put at the *Front-End Electronic Efficiency, Cluster Size Random Noise and dark current*. The results shows that the V_{WP} decrease linearly increasing the V_{th}, (see fig.5.21 (left)). The gas volume efficiency increase rapidly, reaching a plateau at about $V_{th} = 1000$mV (see fig. 5.21 (right)) as well as the electronic efficiency (see fig. 5.6). Moreover, even if the V_{WP} decrease linearly with the threshold, the Cluster Size and Random Noise increase almost exponentially see fig. 5.22.

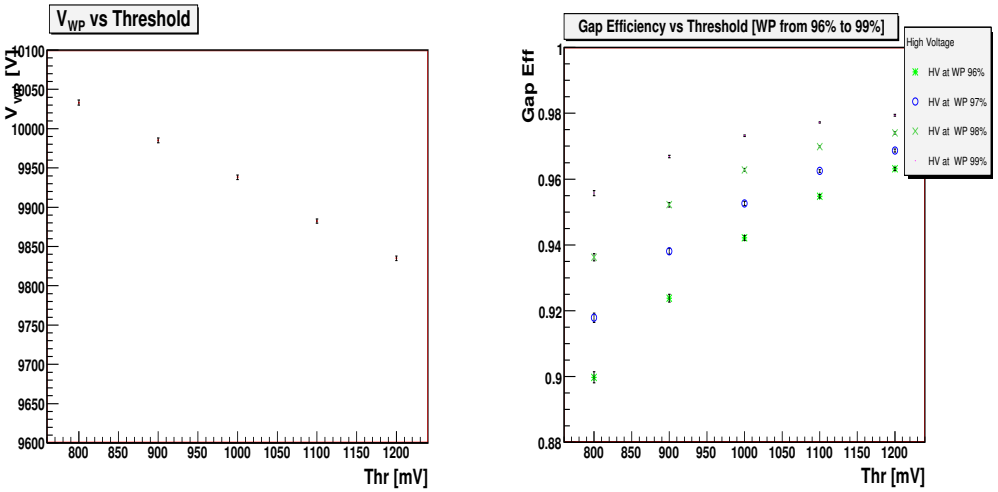

Figure 5.21: *Dependence of V_{WP99} from the threshold (left), Gas volume efficiency vs V_{th} for $V_{WP96} \rightarrow V_{WP99}$ (right).*

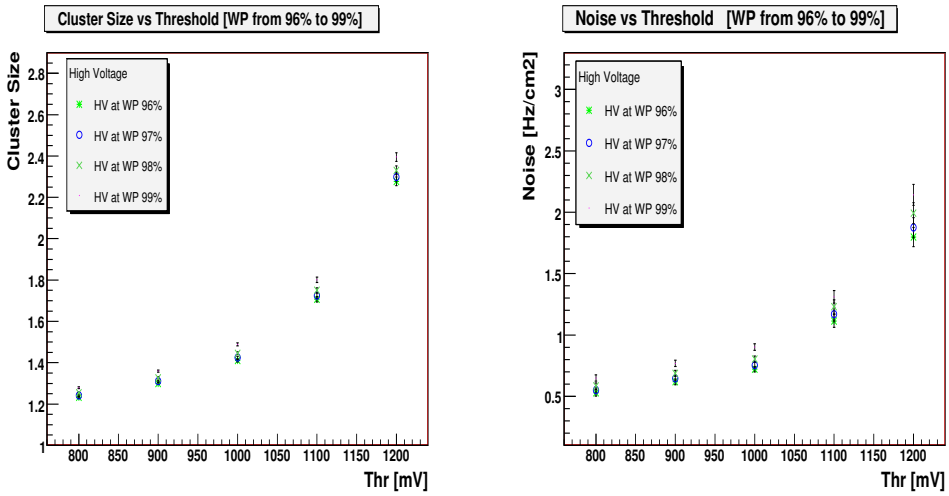

Figure 5.22: Cluster Size vs V_{th} (left) and Random Noise (right) for $V_{WP96} \rightarrow V_{WP99}$

In tab. 5.1 are listed all parameters studied as a function of the percentage of top eff and front-end threshold.

% Top eff	V_{WP} *(Volts)*	V_{th} *(mV)*	*Gap Eff.(%)*	*Clus. Size*	*Noise* (Hz/m^2)	*Current* $(\mu A/m^2)$
96%	*9829*	*800*	*94.2* ±0.1%	*1.3*	*0.6*	*0.41*
	9786	*900*	*94.3* ±0.1%	*1.3*	*0.6*	*0.40*
	9742	*1000*	*94.5* ±0.1%	*1.4*	*0.7*	*0.39*
	9689	*1100*	*94.4* ±0.1%	*1.7*	*1*	*0.37*
	9644	*1200*	*94.5* ±0.1%	*2.2*	*1.4*	*0.36*
97%	*9872*	*800*	*94.8* ±0.1%	*1.3*	*0.6*	*0.42*
	9828	*900*	*95.1* ±0.1%	*1.3*	*0.7*	*0.41*
	9784	*1000*	*95.3* ±0.1%	*1.4*	*0.7*	*0.40*
	9730	*1100*	*95.3* ±0.1%	*1.7*	*1*	*0.39*
	9684	*1200*	*95.4* ±0.1%	*2.25*	*1.5*	*0.37*
98%	*9932*	*800*	*95.6* ±0.1%	*1.3*	*0.6*	*0.44*
	9887	*900*	*96.1* ±0.1%	*1.3*	*0.7*	*0.43*
	9841	*1000*	*96.3* ±0.1%	*1.4*	*0.8*	*0.42*
	9786	*1100*	*96.3* ±0.1%	*1.7*	*1*	*0.40*
	9741	*1200*	*96.4* ±0.1%	*2.3*	*1.5*	*0.39*
99%	*10030*	*800*	*96.7* ±0.1%	*1.3*	*0.7*	*0.48*
	9985	*900*	*97.1* ±0.1%	*1.4*	*0.8*	*0.45*
	9938	**1000**	**97.3 ±0.1 %**	**1.5**	**0.9**	**0.44**
	9882	*1100*	*97.4* ±0.1%	*1.8*	*1.1*	*0.43*
	9835	*1200*	*97.4* ±0.1%	*2.3*	*1.7*	*0.41*

Table 5.1: *Main RPC parameter, for different WP and different front-end threshold* V_{th}.

Comparing all results shown in Tab. 5.1 with the ATLAS requirements (Gas Volume Efficiency > 96%, Cluster Size< 1.5 and Noise< $2Hz/cm^2$) the optimal working point can be set as V_{WP99} resulting in average HV = 9938 Volts at V_{th} = 1000 mV. The average value of dark current distribution, at the V_{WP} chosen, normalized on the detector surface is about $0.44\mu A/m^2$ and that also fits the ATLAS requirements (see fig.5.23).

As already done for V_{50} to ensure a complete independence of V_{WP} from temperature and pressure the behavior of V_{WP} versus these environmental

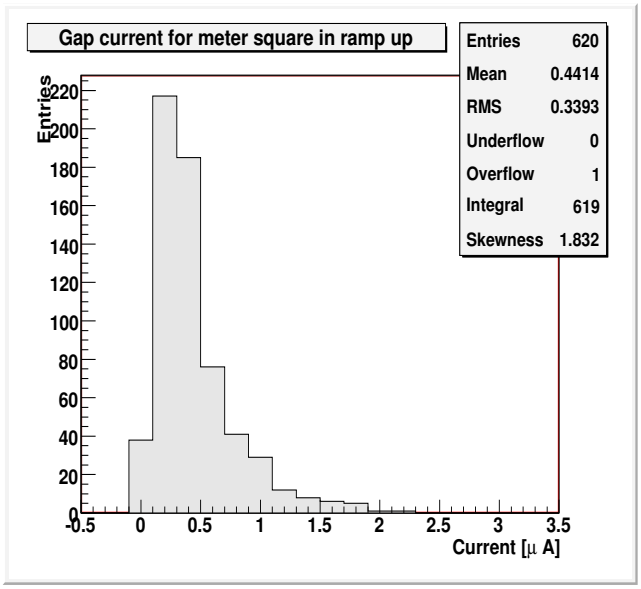

Figure 5.23: *Dark current distribution at V_{WP99} chosen, normalized on the detector surface.*

parameter has been studied. For each test group the average V_{WP} was calculated with: no correction, "standard" correction and the empirical correction. In fig.5.24 (left) is plotted the V_{WP} calculated with any correction and the "standard" correction as a function of temperature: we find the analogous trend obtained with the V_{50}. Beside fig.5.24 (right) the V_{WP} corrected with the empirical formula is plotted, any dependence appears. The same exercise was repeated to verify the any dependence from pressure fig.5.25 showing again that also V_{WP} has been made independent of pressure.

Is interesting to see how the V_{WP} distribution changes changing using different correction for T and P. If no correction is adopted, fig. 5.26 (left), the mean value of the distribution is about 9865 Volts and its RMS is 96.2 Volts. If we correct our data with the standard formula, then the distribution, fig. 5.26 (right), move up to an average value of 9999 Volts and its RMS becomes 85.2 Volts, this is consisting if we remember that the standard correction produce an overcorrection.

Finally if we adopt the empirical correction the average value of the V_{WP} distribution becomes 9938 Volts and its RMS 71.7 Volts (fig.5.27).

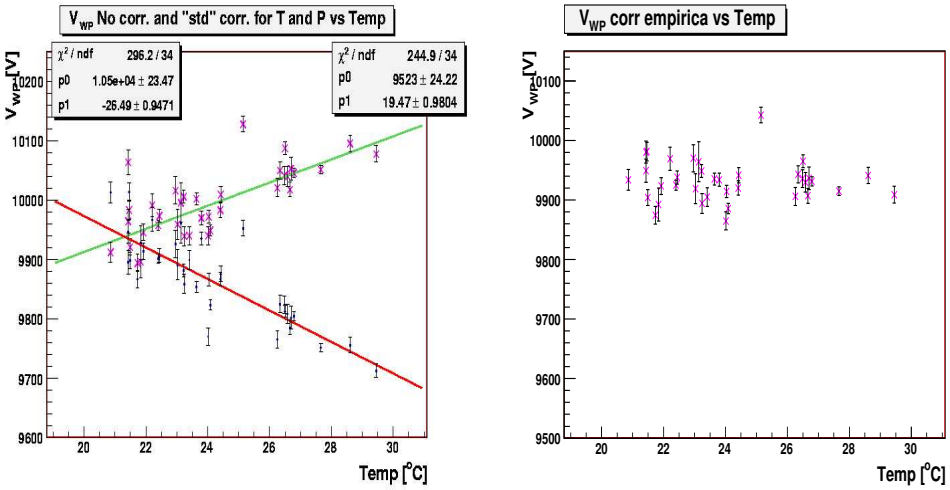

Figure 5.24: V_{WP99} vs Temperature with no correction and "standard" correction (left) and with empirical correction (right).

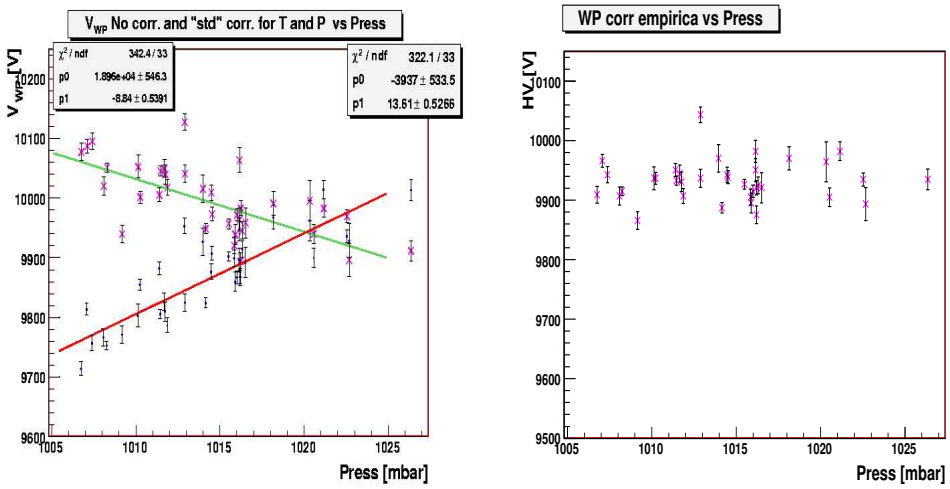

Figure 5.25: V_{WP99} vs Pressure with any correction and "standard" correction (left) and with empirical correction (right).

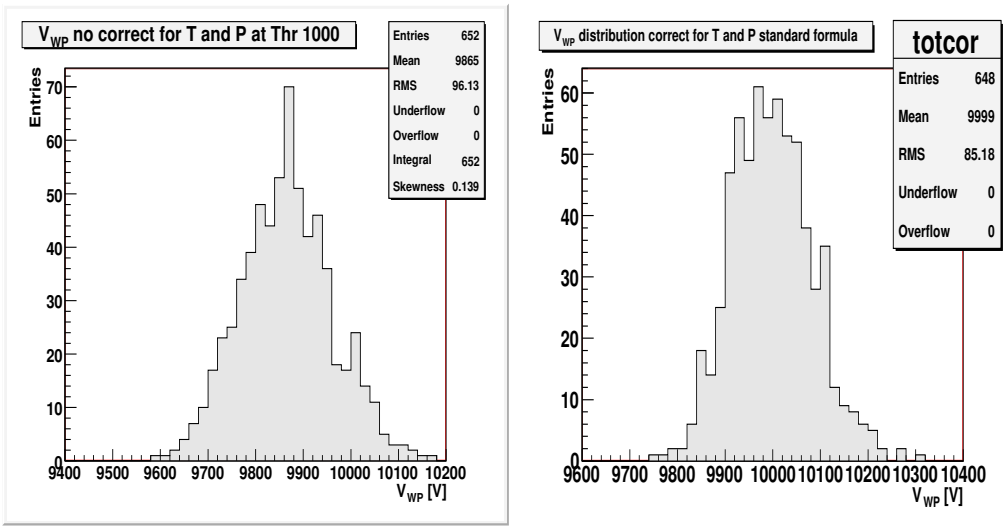

Figure 5.26: V_{WP99} distribution $V_{th} = 1000$ mV with no correction for T and P (left), and "standard" correction for T and P (right).

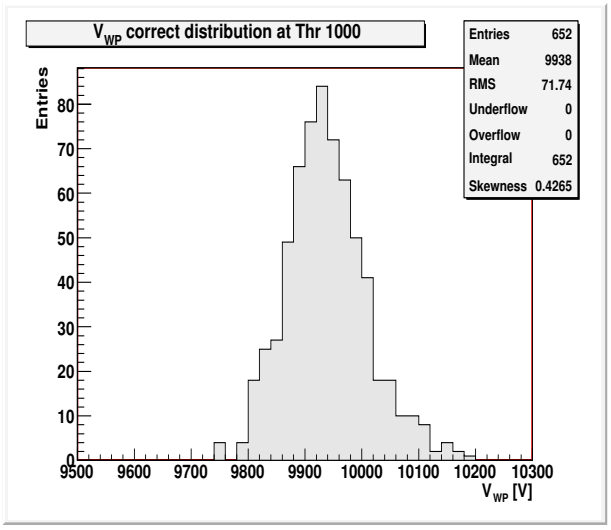

Figure 5.27: V_{WP99} distribution $V_{th} = 1000$ mV HV with empirical correction for T and P.

The spread has diminished again and now is probably only due to the dimension spread of the gas volume. Spacers, which define the gap width were built with a spread of 15 μm on the 2 mm total width. This is in agreement with a variation induced on the electrical field to about 70 Volts, in good agreement with the RMS of our distribution.

5.7 Conclusion

A systematic ATLAS RPC characterization was given using for the first time a very large sample of detectors. The main properties of the detector have been extensively studied, the results showed that the RPC produced fulfill the ATLAS requirements. In particular noise, cluster size and currents are under control.

A dependence from temperature and pressure has been found, and specific correction at the data has been obtained for the first time. The nature of this particular behavior is under investigation.
Moreover extensive study of detector response for large temperature variation was performed finding sensible increase of the dark current with temperature due both to the ohmic and to the multiplicative components of the current-voltage characteristics. In addition, a clear correlation is found between the multiplicative component of the dark current and the noise rate. This can be interpreted as due to a saturated avalanche regime where the saturated charge scales only linearly with the applied electric field. A low temperature of operation is preferable in ATLAS, in order to keep dark currents and noise rate as low as possible. Nevertheless, since in the ATLAS experiment a beam related background of about 10 Hz/cm^2 is expected, aging phenomena will likely be dominated by this noise component more than high temperature effects.

Finally a working point for all the Barrel Outer Chamber of ATLAS has been defined and extensively characterized. This is useful step for the ATLAS commissioning phase.

Chapter 6

RPC test with cosmic rays in the ATLAS experiment

6.1 Introduction

Since June 2006 the muon ATLAS community was involved in the muon spectrometer commissioning with cosmic rays. During the first phase 6 muon stations of the apparatus, in the so called sector 13, were instrumented in order to do a pre-commissioning exercise as close as possible to the final detector configuration. This was the first opportunity to check in final configuration the complete read out chain, the developed software tools and to study the detector response performance in final configuration. We put our attention to the RPC detector. First of all, the correct trigger cabling was checked, to do this the official ATLAS software and specific software tools was used. Moreover to perform RPC efficiency measurements, a standalone reconstruction program, using only the RPC detector, were realized. In this chapter will be illustrated the status of the RPC detector of the ATLAS Sector 13, the data taking, the standalone software and the first measurements performed with the test carried out in November and December 2006.

6.2 Sector 13 set-up

The first exercise of data taking was carried out with three BML and three BOL stations of sector 13 which corresponding to six muon trigger towers. As

already said in chapter 3, two kinds of barrel sector are defined in the ATLAS muon spectrometer: Large and Small sector and sector 13 is a Large sector located between the ATLAS feet (in the lower part of the detector). Each trigger tower consists of three-half stations: Inner, constituted by only MDT chambers, Middle, constituted by a MDT chambers 'sandwiched' between two RPC chambers and Outer, made of an MDT and a RPC chambers. Due to the position in muon spectrometer and their function in trigger selection, the RPC chamber are called: BML/BMS confirm, BML/BMS pivot, BOL/BOS confirm. In this configuration there were 72 read out panels (36 η and 36 ϕ) and 36 gaps.
Fig. 6.1 shows a BML station assembled at the BB5 facility at CERN[65].

Figure 6.1: *Assembled BML muon station before installation on the apparatus. BM stations are made by two RPC planes with the MDT chamber 'sandwiched' between.*

The muon stations used in this test are located in side A ($z > 0$) and are the first three from the interaction point in η. Fig. 6.2 shows the setup used during the data taking and its location in the apparatus.

The RPC were read-out by 48 CMA, in this setup only one Sector Logic boards controls and collects data from CMA's realizing two independent muon trigger sector logics, each one with three projective trigger tower along the beam line. In order to increase the cosmic ray rate the trigger spatial

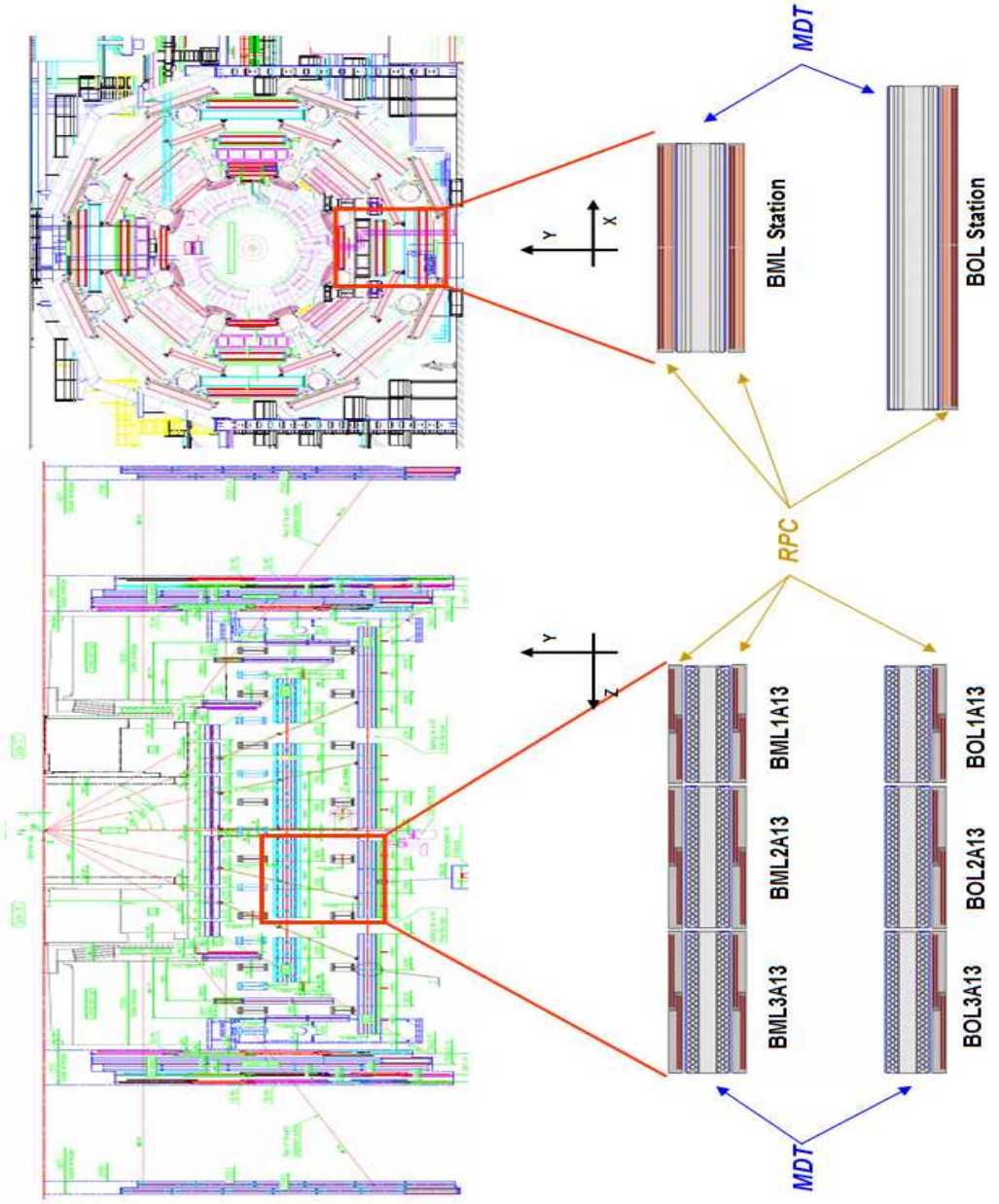

Figure 6.2: *Location of sector 13 muon stations instrumented for November-December 2006 taking.*

coincidence window, was set to the maximum value allowed by the CMA's cabling. Different trigger combinations were tested, (*single and combined views*) and different majority coincidence (*2/4, 3/4 of Low Pt station*). The most relevant data were acquired with the trigger generated with both views in coincidence and a majority of 2/4 on Low Pt.

6.3 Data Taking in Sector 13

6.3.1 Auto Trigger Strategy

Scope of this work is to measure in unbiased way the performances of a detector that has to generate the trigger signal. If one wants to measure the efficiency of RPC without bias, one have to separate the RPC layer that take the trigger decision from the layer that one wants to measure efficiency. In order to do this we decided to perform the measurements in two different runs where alternatively only three of six layers of each tower generate the trigger and are used in tracking, the remaining three layers are studied. The time required for the data taking is duplicated but it allow to perform extensive studies with the certainty to not introduce biases. In order to reduce the track extrapolation error only one of two layers of each RPC chamber was used to generate the trigger each time. Fig.6.3 shows the trigger configuration during the efficiency measurements.

6.3.2 Data Taking

In order to perform a complete study on RPC behavior several set of runs were taken. Due to the limited time and the hardware setup not in a final configuration, some measurements were not performed on all the detector, although the data were enough to define the status of the apparatus tested. The description is made for a single tower, although the data was taken on all six towers at the same time.

- Run to test and verify electronics and read-out system.
- High voltage scan: layers $J1_{lowpt}/I1/J1_{highpt}$ from HV = 10000 Volts to HV 8900 Volts, front end threshold V_{th} = 1000 mV. Trigger setup: $J0_{lowpt}/I0$ majority 2/4 η and ϕ view in logical end, HV = 9800 Volts V_{th} = 1000 mV .

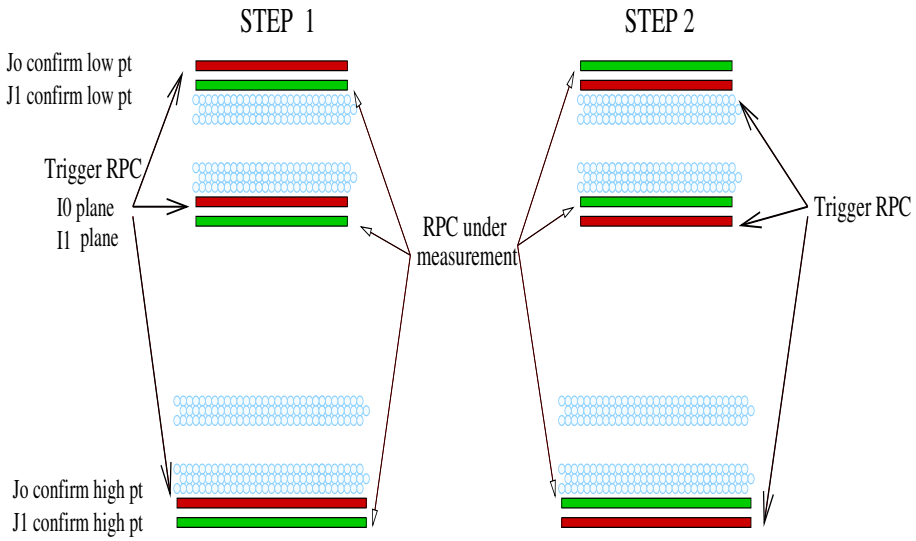

Figure 6.3: *The two trigger configuration during the efficiency measurements. RPC in red are used to trigger and to reconstruct tracks in green are the RPC under test. J0/J1, I0/I1 symbols are used to distinguish the six plane in the trigger system.*

- High voltage scan: layers $J0_{lowpt}/I0/J0_{highpt}$ from HV = 10000 Volts to HV 8900 Volts, front end threshold V_{th} = 1000 mV. Trigger setup: $J1_{lowpt}/I1$ majority 2/4 η and ϕ view in logical end, HV = 9800 Volt V_{th} = 1000 mV.
- High voltage scan: all six layers HV = 10000 Volts to HV 8900 Volts, front end threshold V_{th} = 1000 mV. Trigger Random.
- V_{th} scan: all layers at HV = 9800 V_{th} from 1200 mV to 800 mV.Trigger setup: $J1_{lowpt}/I1$ majority 2/4 η and ϕ view in logical end, HV = 9800 Volts, V_{th} change as the layers under test. (Due to the limited time on hand this measurement was not repeated on the complementary layers.)

Before data taking a preliminary phase was needed to verify and setup the hardware electronics. In particular to calibrate in time all the coincidence matrices. Trigger timing calibration are very important since the trigger performance are directly related to the CMA synchronization. The data

taken phase, extended for more than one week was entirely dedicate to acquire the data needed to characterization the RPC detector.
In this pre-commissioning exercise due to electrical connection problems some channels on two different planes were unplugged and the front-end thresholds of other three planes were fixed at $V_{th} = 800$ mV.
As for the test stand was important to make our data independent from temperature and pressure. For the CERN data we decided to choose as reference point: $T = 20^0C$ and $P = 980$ mbar which correspond to standard environmental conditions in the experimental cavern. All measurements described in this work were performed at these reference temperature and pressure value, so no correction to the applied HV was necessary.

6.4 ATLAS Offline Software: ATHENA

The Athena framework [66] is an enhanced version of the Gaudi framework that was originally developed by the LHCb experiment, but it is now a common ATLAS-LHCb project and is used by several other experiments including GLAST and HARP. Athena and Gaudi are realizations of a component-based architecture (also called Gaudi) designed for a wide range of physics data-processing applications. The fact that it is component-based had allowed flexibility in developing components that are specific to the particular experiment and better meets its particular requirements. In particular, by means of Job Option Service is possible to modify properties of Algorithms, Tools and Services. After data taking, file are stored in a CERN mass storage facility called CASTOR. With ATHENA is possible to retrieve directly the run files from CASTOR to analyze them.

A selectable set of algorithms can be chosen which operates on the data. In our case only the decoding is done. The results are output on a ROOT file (*root-ple*)[67]. By means of Job Option one can e choose the block of variables to store in the rootple output file. Since we are interested in RPC data we choose three class of RPC data object: *RPC_Raw_Data*, *RPC_Digits_Data* and *RPC_PRD_Data*. RPC_Raw_Data contain all informations directly read out from the detector hardware. Raw data hits are identify by Sector Logic, Pad, CMA, ijk (groups of channel in CMA) and front-end channels. The other RPC data object are reconstructed from RPC_Raw_Data using the Cabling Service and the Geo Model Service. Each single hit is converted in ATLAS coordinate: RPCStation, DoubletPhi, DoubletR, DoubletZ,

etc.. . RPC_PRD_Data are expressed in the same coordinate system of RPC_Digits_Data but they also provide to solve the ambiguity of ϕ strip generated by logical or-ing and hardware or-ing. May also provide to flag the detector hits and the trigger hits. The program described in §6.6, use the ATHENA rootple with RPC_PRD_Data block variable.

6.5 RPC Sector 13 Data Quality Control

Data quality control is the first step of the data analysis. In order to do this and to verify the raw data consistency dedicated software tools were developed (*root macro*).

6.5.1 CMA Timing

First of all the timing distribution of all CMA for each PAD were checked. The time distribution of the 192 input channels of each CMA were plotted with the time distribution of the 32 trigger output channels (see fig. 6.4). Timing of each CMA was adjusted by setting the extracted delay into pipelines while noisy channels were masked to allow optimal trigger selection.

6.5.2 Strip profiles, CMA and PAD control

Front-end channel response was checked looking to the strip profiles of each read out panel. Due to the CMA cabling overlaps and the or-ed strips in ϕ view the interpretation of the hit profile is not straight forward. As already explained in sect.3.4.3 some channels of the confirm plane are read out from different CMAs. Moreover wire or-ed ϕ strips on all planes are logical or-ed on the confirm plane. Since the read out system reads everything come from the detector in many cases to a fired single strips corresponds up to 16 occurrences in raw data. Fig. 6.5 shows an example of η overlap.

Overlap in η view is solved just sorting channels by CMA they belong.

For ϕ planes, due to the "logical" and "hardware" or-ing, beside the sorting is also necessary to require corresponding η strip to identify the right strips. The PRD produced by ATHENA perform all these operations. Is interesting to see how the number of hits is reduced with different operation. Fig. 6.6 (a) shows the profile produced by ATHENA for a generic ϕ plane

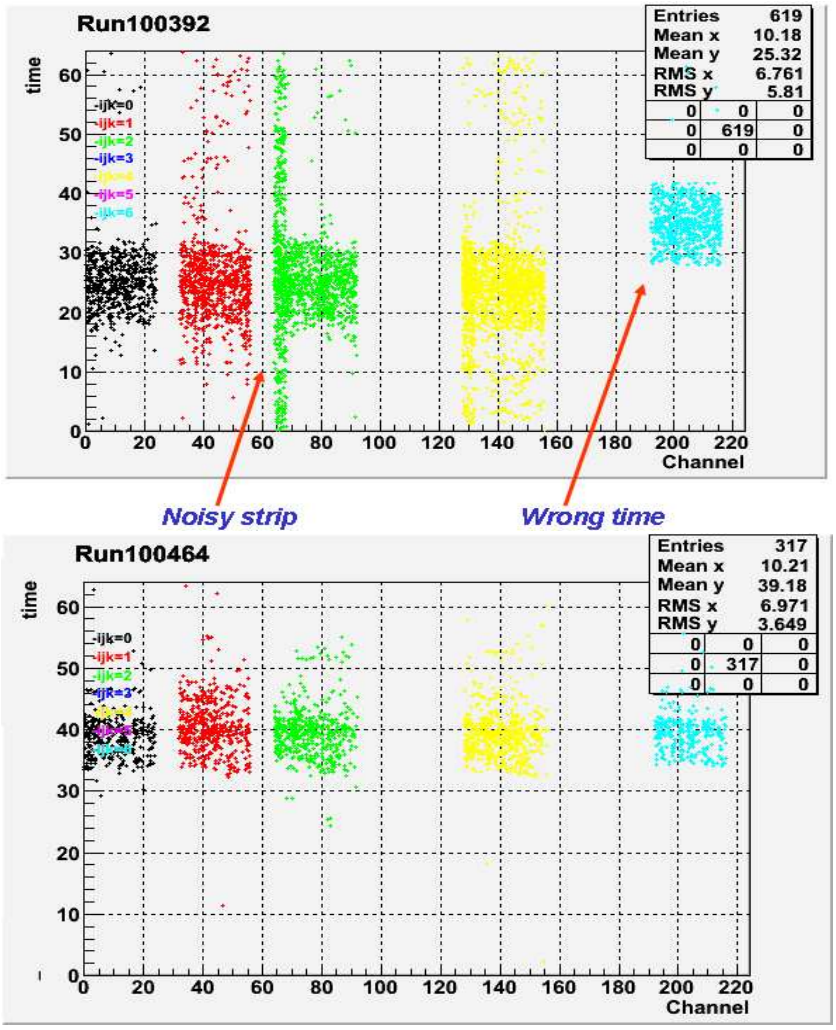

Figure 6.4: *Example of CMA timing before and after the time calibration and noisy channel masking.*

using RPC_Digits_Data (overlaps are still presents). In section (b) are used the RPC_Raw_Data, the channels are sorted by CMA but the logical and hardware or-ing are not yet solved. Section (c) shows the profile produced by ATHENA using RPC_PRD_Data, all or are solved but remain the overlap of CMA. Finally in section (d) a cluster profile obtained with the Reconstruction program, that we will present in next paragraph, is showed.

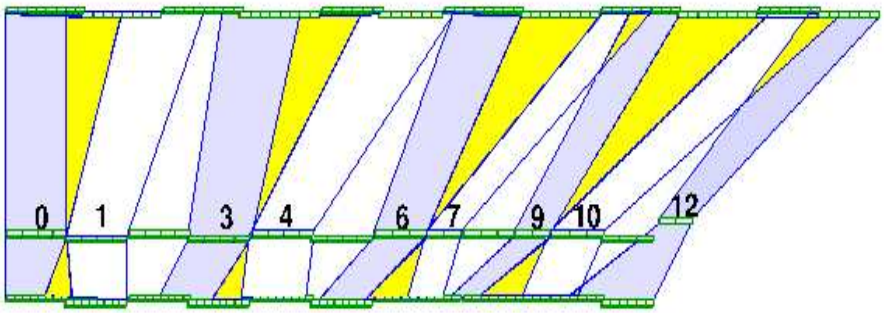

Figure 6.5: *Double counting (in yellow) in η plane due to the CMA overlap (not all the overlap are shown to make a clearer picture).*

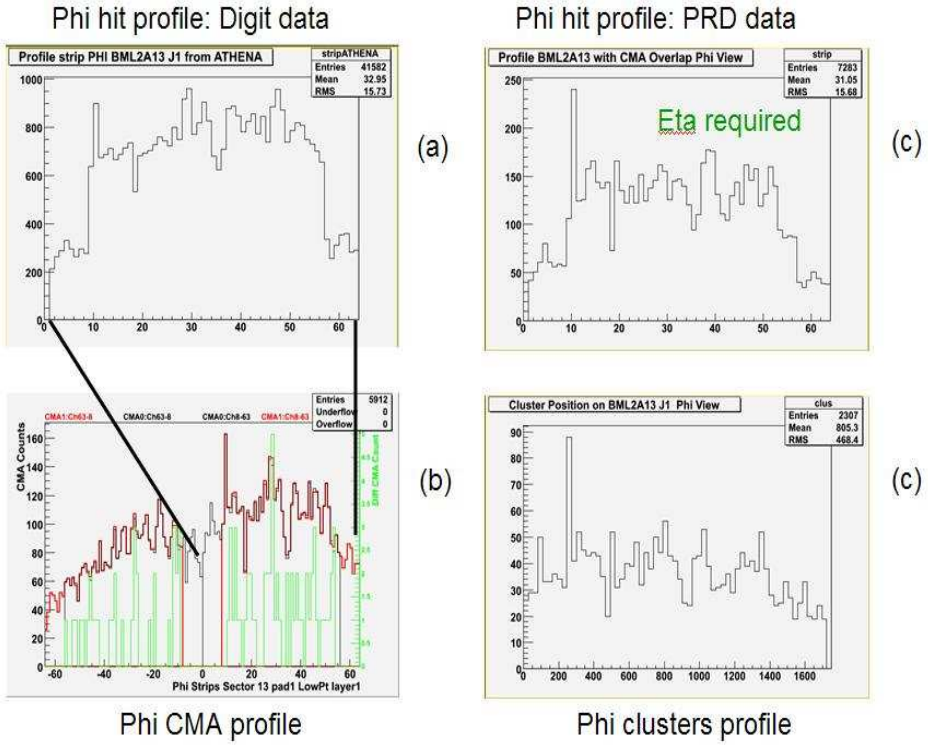

Figure 6.6: *Strip profile obtained RPC_Digit_Data (a), RPC_Raw_Data (b), and RPC_PRD_Data (c) and cluster profile (d). In plot (c) the different CMA are plotted in black and red and their different counts in green.*

With this technique a profile for all strips organized for strip plane and for CMA are realized. Even if only 6 on 384 trigger towers was tested, for each run 48 CMA profiles and 78 read out panels profiles have to be made.

In order to check the cable connections consistency for each PAD and for each layer, the correlation between the ϕ strips of a PAD with all the η strips of the sector logic is plotted (see fig. 6.7).

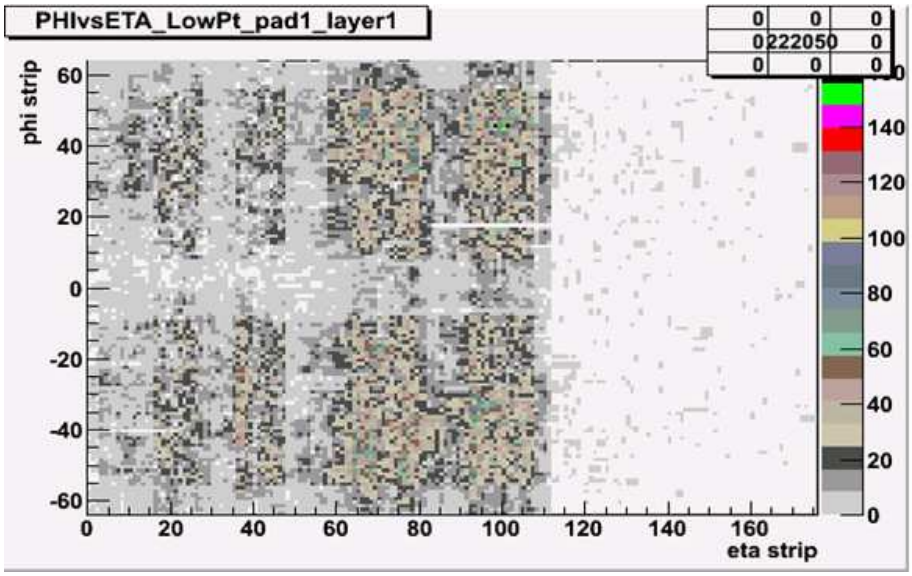

Figure 6.7: *η/ϕ spatial correlation for ϕ CMA of PAD 1 related to Layer 1 of low p_t.*

As we already explained in §3.4.3, the same channels are often split and read-out by CMA's of different PAD. Comparing the bidimensional plots of all ϕ CMA and all PAD related at the same layer, is possible to find possible mistakes in cabling or missing connection. Due to the logical or-ing often missing connections could not be identify from the CMA profiles. An example is shown in fig. 6.8 where the channels circled in red are read out by PAD 1 but are not read out by PAD 2 as should be according to the cabling scheme.

Finally hit correlation between adjacent layers in the same view are performed to check cabling swap, which can appear at two different hardware levels: at the detector front-end or at PAD input. Cable exchange on detector

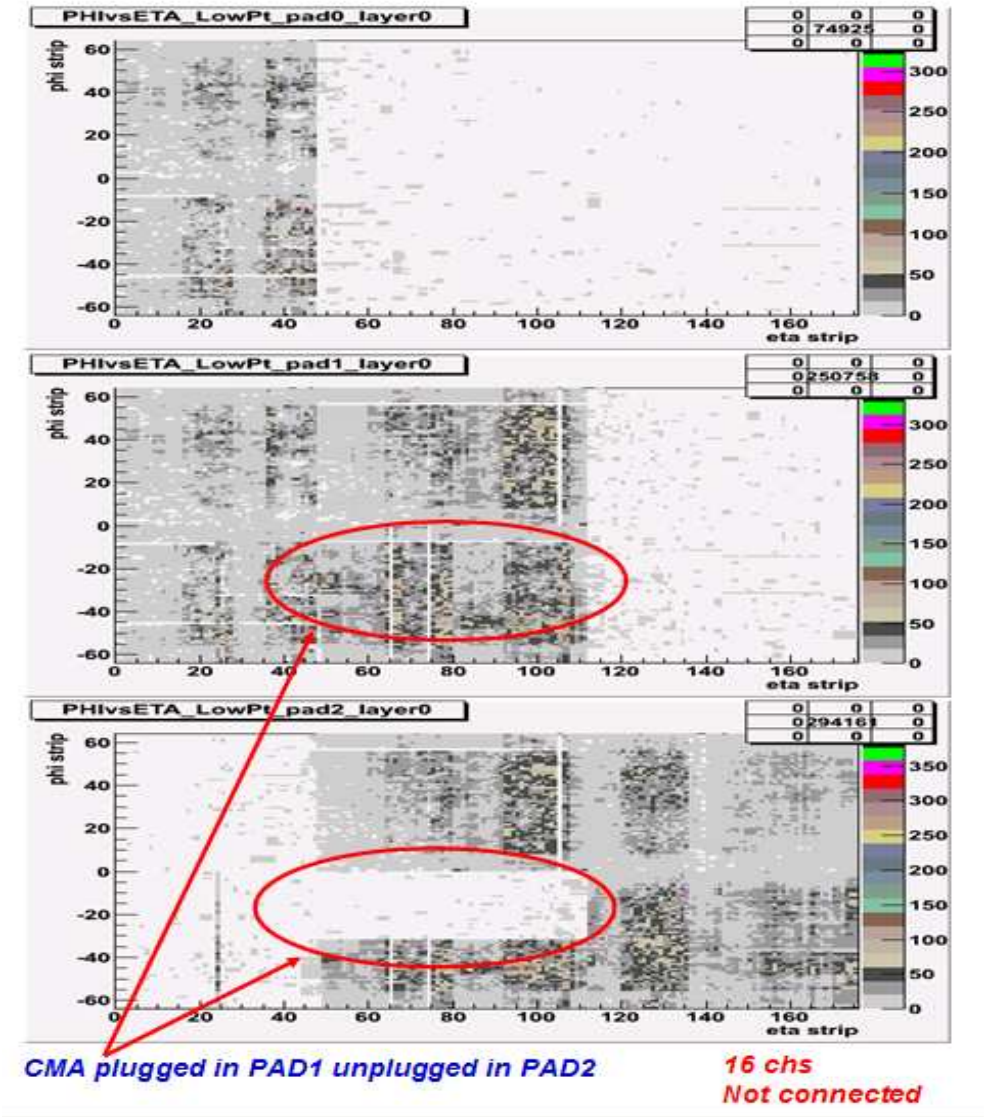

Figure 6.8: *Missing CMA in PAD input from adjacent trigger tower.*

front-end produce a well separate line because all hits that arrive at the PAD are exchanged while swap on PAD input usually generate both straight line due to a correctly cabled CMA and a separate line due to CMA with error in cabling.

Fig. 6.9 shows the two signature due to swap on the detector (plot a) and on the PAD input (plot b).

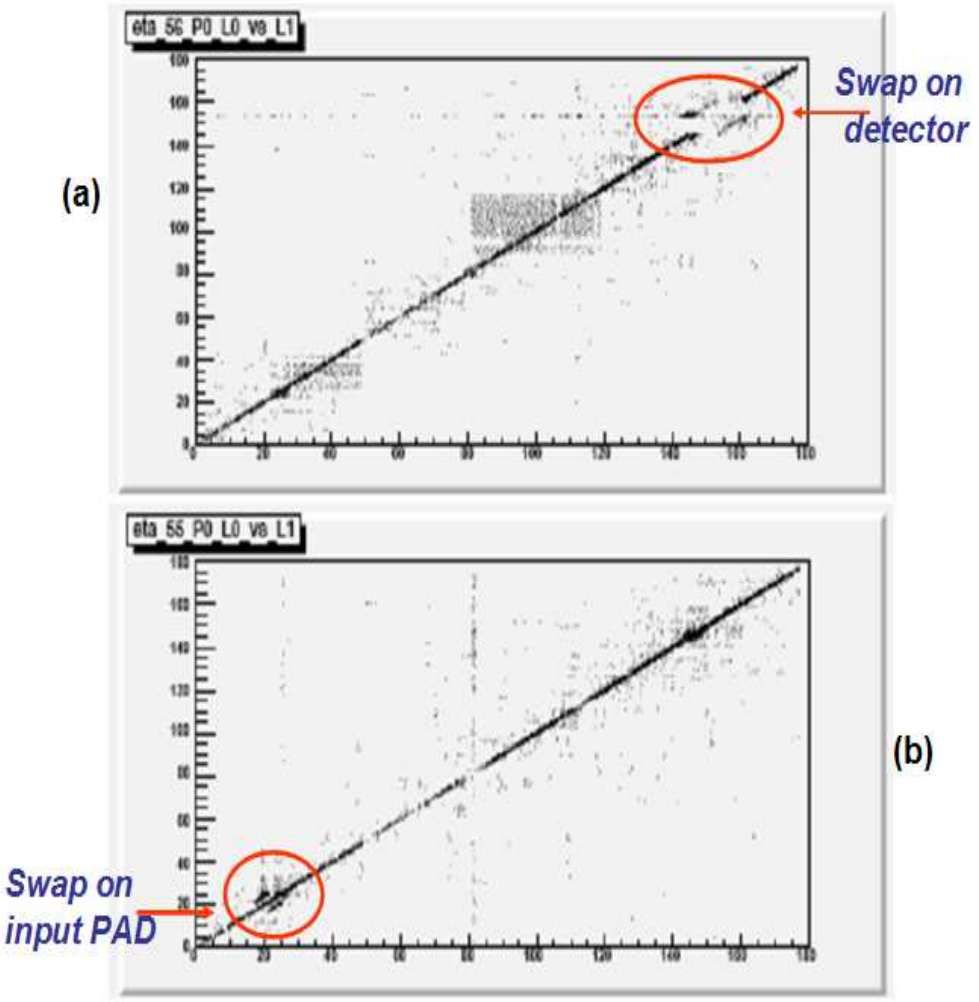

Figure 6.9: *Hits correlation between adjacent layers of the same view. Plot (a) shows a detector connector swap, while plot (b)shows a PAD connector exchange.*

6.6 A RPC Standalone track reconstruction program

An dedicated data analysis software was developed starting from a code [68] developed for the ATLAS test beam at H8 facility in 2004 [69]. It is written in C++ language and make use only of RPC hits. It is intended to be used during the detector commissioning phase, when each detector community have to test the detector independently by the entire experiment and a fast and manageable off line analysis is important. The standalone program works both on η and ϕ views. Reconstruction of the ϕ view is fundamental because only the RPC detector provide the ϕ coordinate and a full characterization in that view is necessary. A further step will be to cross-check the η tracks reconstructed with only the RPC with the one obtained with the MDT.
The software is divided in two separated parts. The first one contains the pattern recognition algorithm and provide the track Reconstruction, while the second one is dedicated to the efficiency measurements. Fundamental feature of this software is the possibility to remove up to 3 layer for each view to perform efficiency measurements in an unbiased way for each views.

6.6.1 The Pattern Recognition and Tracking Algorithm

The Reconstruction track algorithm can be summarized in the following steps:

1 Organization of RPC hits in a list for each layer and view.

2 Clusterization of RPC hits in space (adjacent strips are organized in cluster) and the correct error is assigned.

3 Building of segments between cluster of non adjacent planes.

4 Selection of straight lines and true clusters .

5 Fitting of track candidate and selection of final track .

The third and fourth point characterize the algorithm. The building of segments provide to realize line with clusters from two non adjacent layers, using the cluster coordinates previously calculated from hits coordinates. Fig.6.10 show a possible segment reconstruction in a typical event.

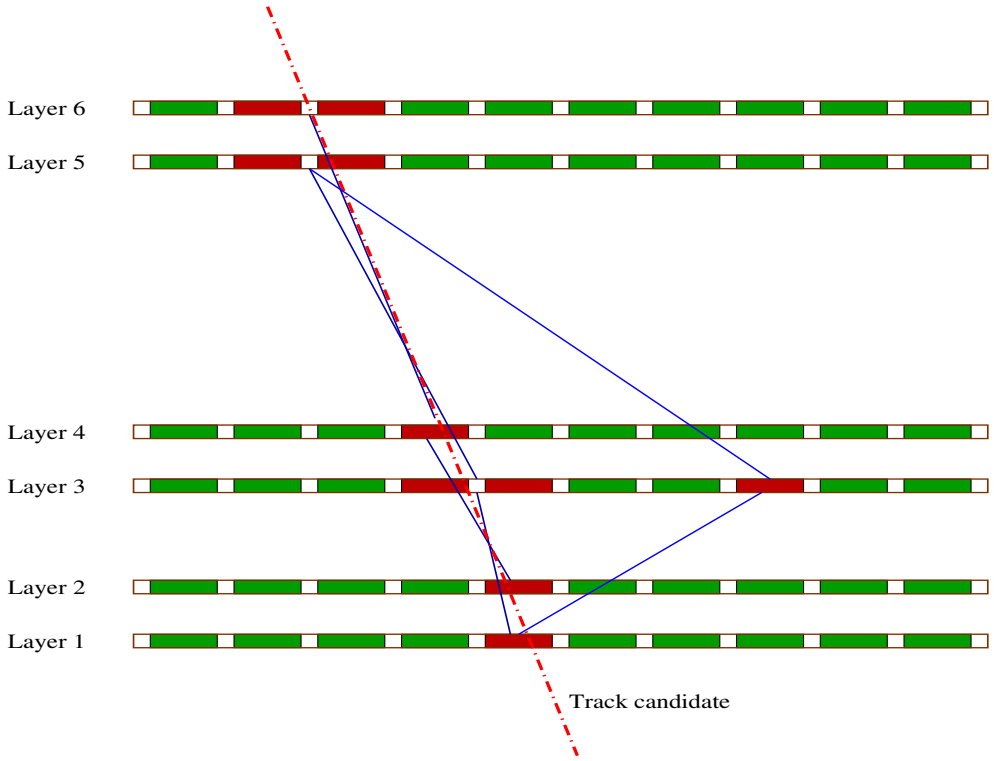

Figure 6.10: *Segment building between non adjacent layers in a typical event (Not all segment are drawn to make clear the image).*

Each segment is identified by its slope (α) and the its intercept (β) in the corresponding view. These quantities are used to fill a bidimesional histogram. The range of the histogram is chosen in order to fit the tower geometry with the slope and intercept distribution. From the tower geometry one can compute the minimum variation of the slope ($\delta\alpha$) and of the intercept ($\delta\beta$) using distance between the first and last layer (about 3 m) and the shortest strip pitch (26.5 mm): the bin width will be the ratio between the width of the α and β distribution and the minimum variation.
For each event all bins with more then one entry are selected and average α and β of that bin are used to obtain a straight line. Starting from this straight line, true clusters are selected. For each layer the cluster closest to the track impact point defined by the straight line is chosen up to a maximum distance corresponding to 3 times the extrapolation error. With all

the selected clusters a track fitting is performed assigning the correspondent error at each cluster candidate.
In principle one can expect as uncertainty of cluster position the value $\sigma = d/\sqrt{12}$ where d is the cluster dimension, but in this way the effective error results over estimate. In order to associate the correct uncertainty to the cluster position the efficient cluster size distribution of each panel was studied. The efficient cluster are only the cluster related at a track.

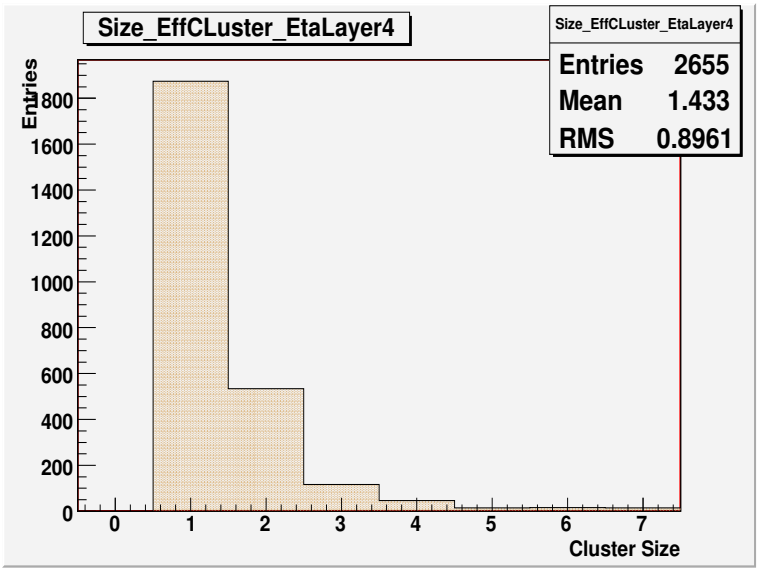

Figure 6.11: *Typical efficient cluster size distribution for RPC read-out panel in Sector 13.*

Let's first assume that cluster size > 2 is due to cross/talks, δ-rays or noise. Than one can assume the following: when the particle crosses a gap region well inside a single strip the induced charge which trigger the front-end threshold is completely distributed on a single strip. When a particle crosses the region between the two strips the charge is divided on two strips and both of them are fired. In a simple model one can assume that the size of the region in which one get two strips can be determined by the ratio of times one gets 2 strips over the total time one gets 1 or 2 strips clusters. This results in the following assignment for the C.S. 1 and C.S. 2 errors: cluster size 1 error is $\frac{d(P_1)}{\sqrt{12}}$ cluster size 2 error is $\frac{d(P_2)}{\sqrt{12}}$ where P_1 and P_2 are the probability of C.S. 1 and C.S. 2. In this way the error on a C.S. 2 is generally

smaller than C.S. 1. They will be equal for a sharing 50% of probability of cluster size and will be the opposite if C.S. 2 are more frequent than C.S. 1. Fig. 6.12 a schematic view of effective region underneath a strip producing cluster with size one and two.

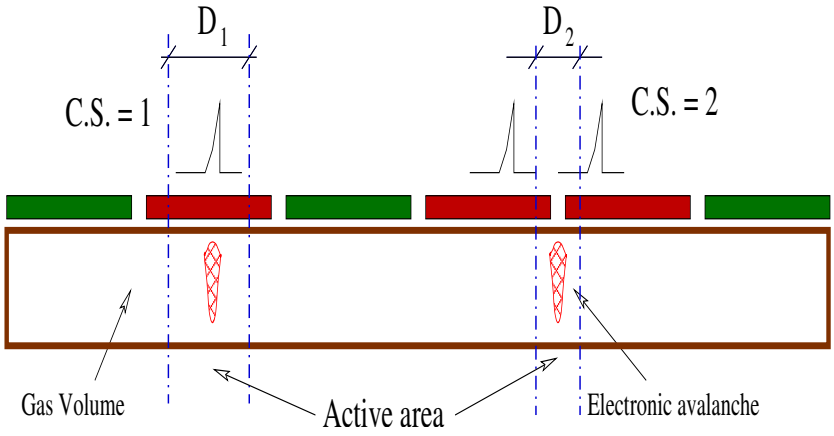

Figure 6.12: *C and region interested by the discharge for cluster size one and two.*

To choose the best track for each event the χ^2_{dof} ($\chi^2_{dof} = \chi^2/dof$) and the numbers of points in track are evaluated. For events with more than one fitted track, we choose the track with the smaller χ^2_{dof} and the maximum number of clusters. Track with $\chi^2_{dof} > 3$ are rejected.
Fig. 6.13 shows distribution of the χ^2_{dof} (left) and the number of points in the selected track (right) a for typical run. The peak at low χ^2 is due to the tracks made with clusters perfectly aligned due to the perfect geometry configuration (no alignment is made at this level) and track are very often perpendicular to the detector. The segmentation of the distribution of the number of point per track is explained by the presence of two different tracks typology: *Long Tracks* that go through all six RPC layers of the tower and *Short Track* that go through only the four layers of low pt station due to the simple 2/4 trigger chosen. The low percentage of tracks with three or five hits is clear indication of the high RPC efficiency.
All the reading, cluster, pattern recognition and fitting takes less than 20 ms/event.

Efficiency measurements are performed by fast algorithm according to the following steps:

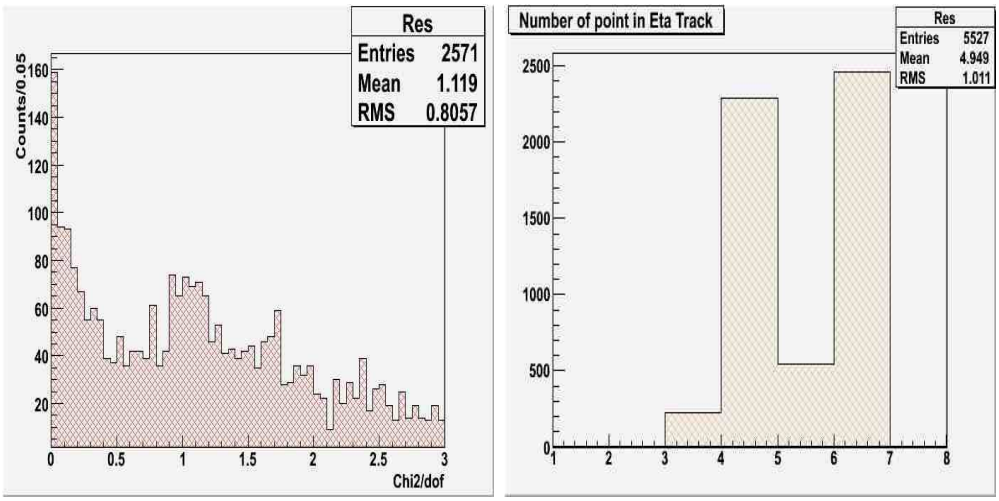

Figure 6.13: χ^2_{dof} *distribution and number of point per track in eta view for a typical run.*

- Good tracks are extrapolated on the plane under test.
- Only extrapolated point inside a fiducial area are considered.
- Planes are considered efficient if a cluster is present at maximum distance of a strip from the extrapolated point.

At the same time the size of the efficiency cluster is measured.

6.6.2 Efficiency determination

As we said in § 6.3.1 to perform unbiased efficiency measurements, only three plane for a time have been used to trigger and reconstruct tracks. Therefore it is very important to control the quality of the track obtained as a function of the noise and cluster size. It is necessary to avoid fake tracks which could introduce an under estimation of RPC efficiency. In order to ensure the selection of good tracks using only three hits, a study of plane efficiency as function of the number of hits in track as been performed.
In tab. 6.1 are listed the number of tracks reconstructed as function of the number of points in track and the obtained efficiency with the statistical error for a strip plane.

Point in track	N. of reconstructed tracks	Plane efficiency	Statistical error
5	2626	94.66	0.49
4	2895	94.61	0.49
3	2913	94.60	0.50

Table 6.1: Reconstructed tracks as function of the number of points in track and the relative efficiency for a strip plane.

As can be seen reducing the number of points used to reconstruct the track the number of reconstructed tracks increases. At the same time a small effect on the efficiency appear. The efficiency evaluated with track performed with 5 points is higher than the efficiency evaluated with tracks reconstructed with 4 and 3 points as expected. Probably same fake tracks were reconstructed, nevertheless the net effect on the efficiency is more than an order of magnitude smaller of the relative statistical error. For this reason, for our data, the error in the efficiency estimation due to the eventually fake tracks can be neglected.

Fig. 6.14 shows the χ^2_{dof} distribution for tracks made with only three points. The peak at zero is expected for χ^2_{dof} with $dof = 1$.

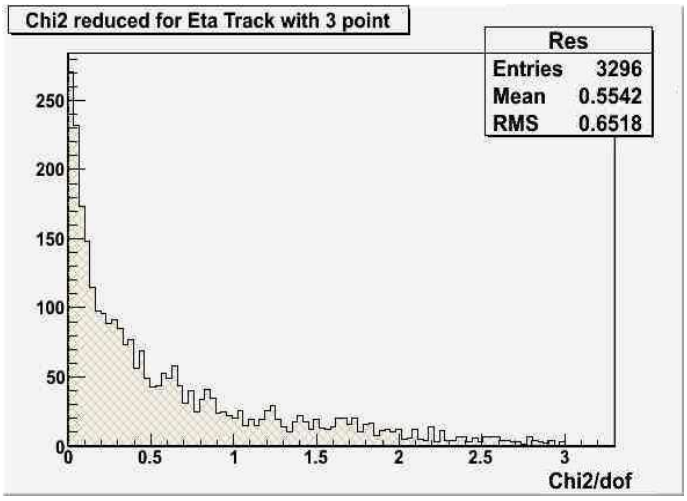

Figure 6.14: χ^2_{dof} *distribution for tracks reconstruct with three point.*

Residual distribution was extracted plane by plane for each view and monitoring of efficiency for tracking plane and plane under measurements was performed. Fig. 6.15 shows typical residual distribution for η and ϕ plane under measurements.

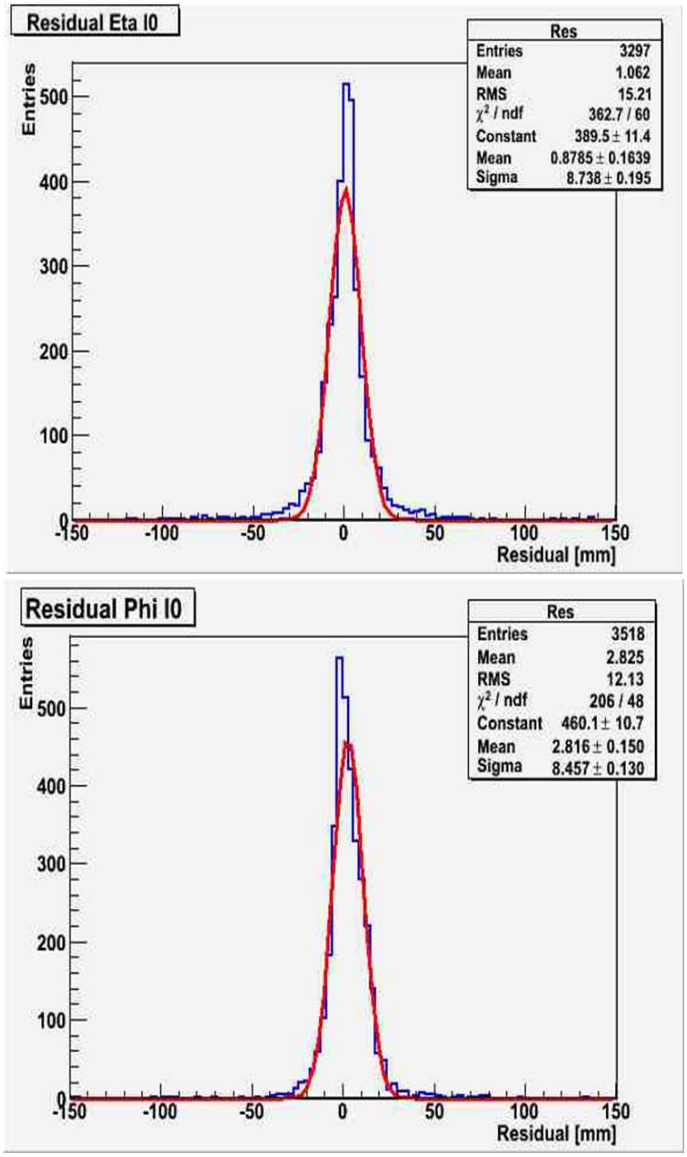

Figure 6.15: *Residual distribution for plane under test.*

Fig.6.16 shows an example of efficiency profile giving the efficiency strip by strip.

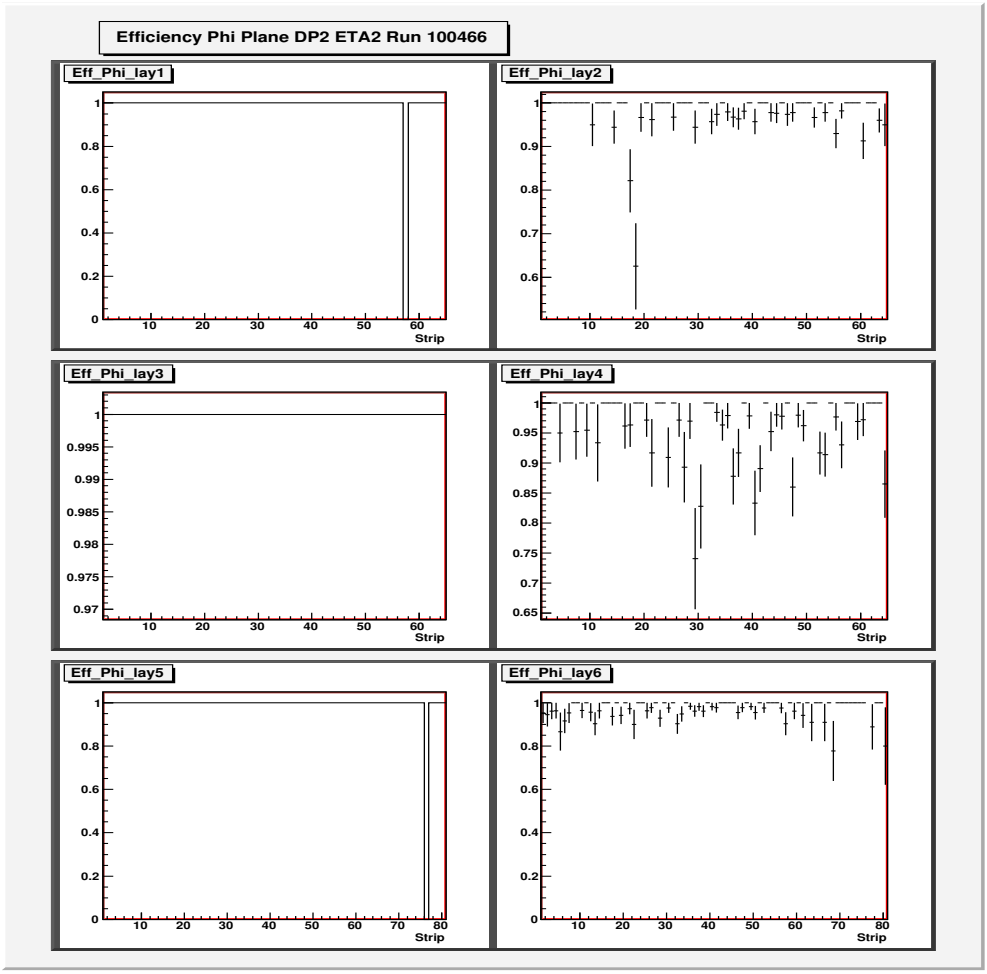

Figure 6.16: *Example of efficiency strip by strip for trigger plane (right) and plane under measurements (left).*

To check uniformity tracks distribution bidimensional plots of the track impact point have been made for all six tower under test (layer by layer). One of these is shown in fig.6.17, the non perfect uniformity is due to the trigger cabling which is designed for muon coming from the detector vertex and not for muon from cosmic rays.

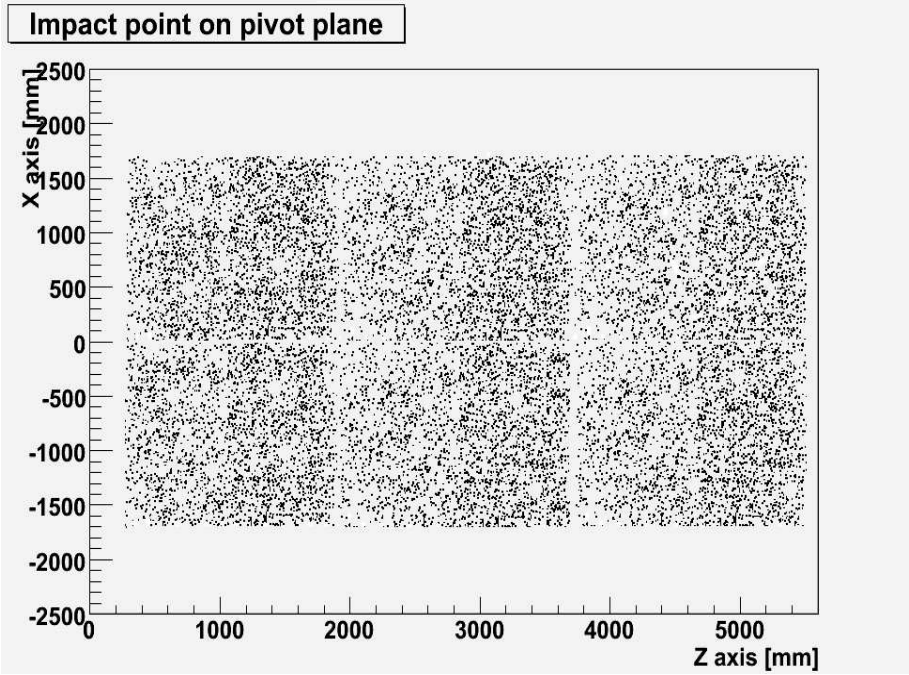

Figure 6.17: *Impact point distribution at pivot plane. The six tower are clearly visible.*

Due to the instrumented station position, most of the muons detected come from the shaft 1 (two shaft allow to carry down the ATLAS components, see fig. 6.18). The origin is evident in the distribution of the angular parameter of the reconstructed tracks in z view. As fig. 6.19 shows the average value of the distribution is not zero but is directly related to the main shaft position. Small fraction of muons came from the shaft 2 and contribute to the left tail of the distribution.

Extrapolating the tracks at surface the hole of the main shaft from which the cosmic rays coming is clearly evident in two dimension (see fig. 6.20).

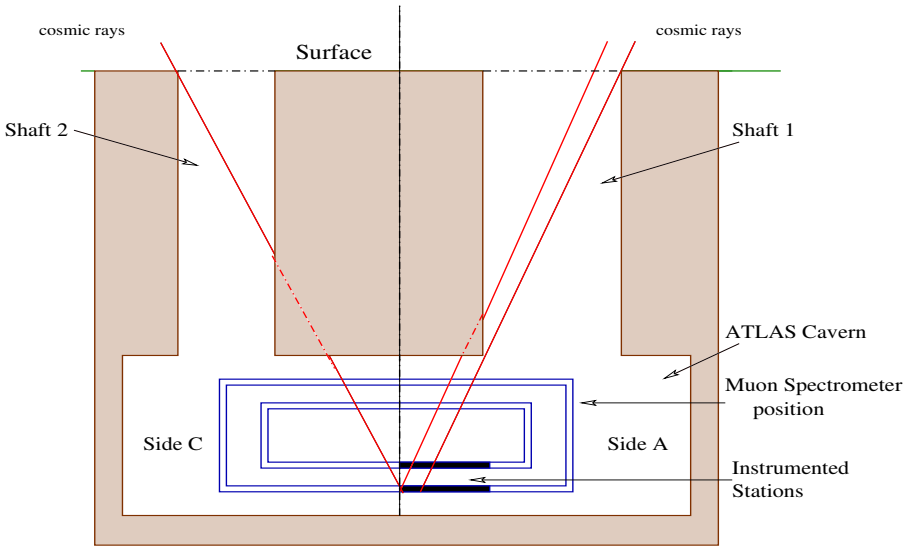

Figure 6.18: *Instrumented muon chamber position relatively to ATLAS shafts.*

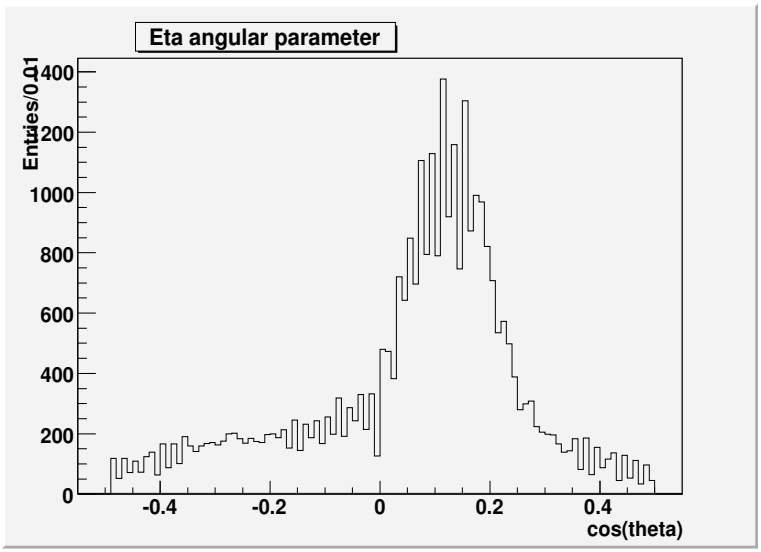

Figure 6.19: *Distribution of the angular parameter of the reconstructed tracks.*

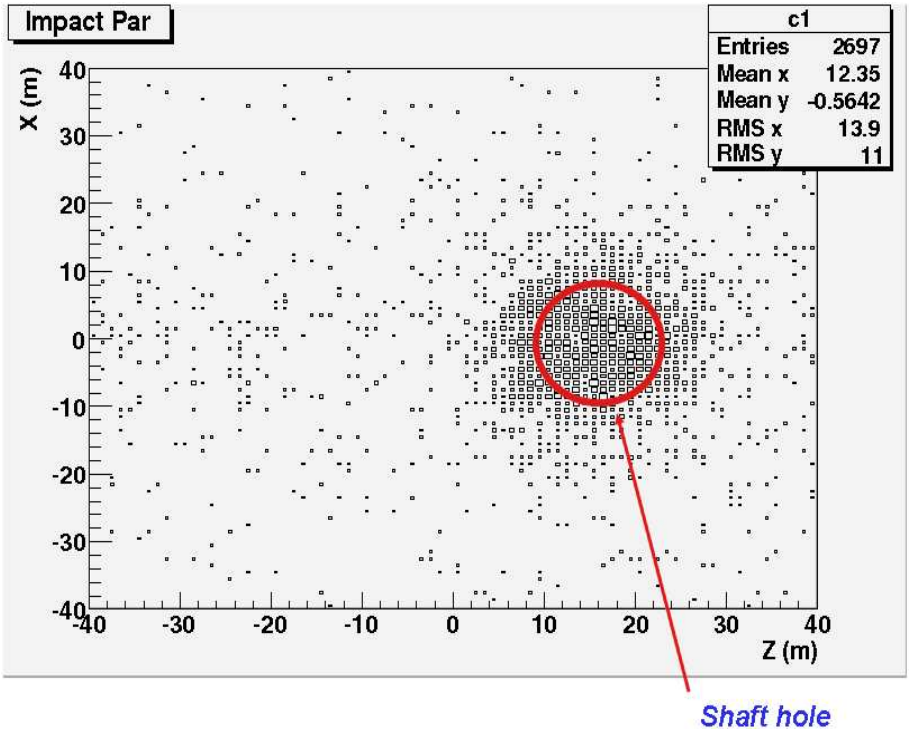

Figure 6.20: *Impact point extrapolated on surface level. The position of the shaft 1 hole is indicated by a red circle.*

6.7 Efficiency and Cluster Size measurements

Primary importance for the muon spectrometer is the efficiency of the trigger chambers. Efficiency of all 72 read out panel has been evaluated at different HV for a front-end threshold of $V_{th} = 1000$ mV. At the same time, for each HV applied, cluster size and the size of the efficient clusters was monitored. Fig.6.21 shows the size of the efficient cluster distribution for the six η planes of a single trigger tower at $HV = 10000$ Volts and $V_{th} = 1000$ mV .

As for the Lecce test stand the eq. 4.2 was used to fit the data; fig. 6.22 shows an example of efficiency curve obtained with Sector 13 data.

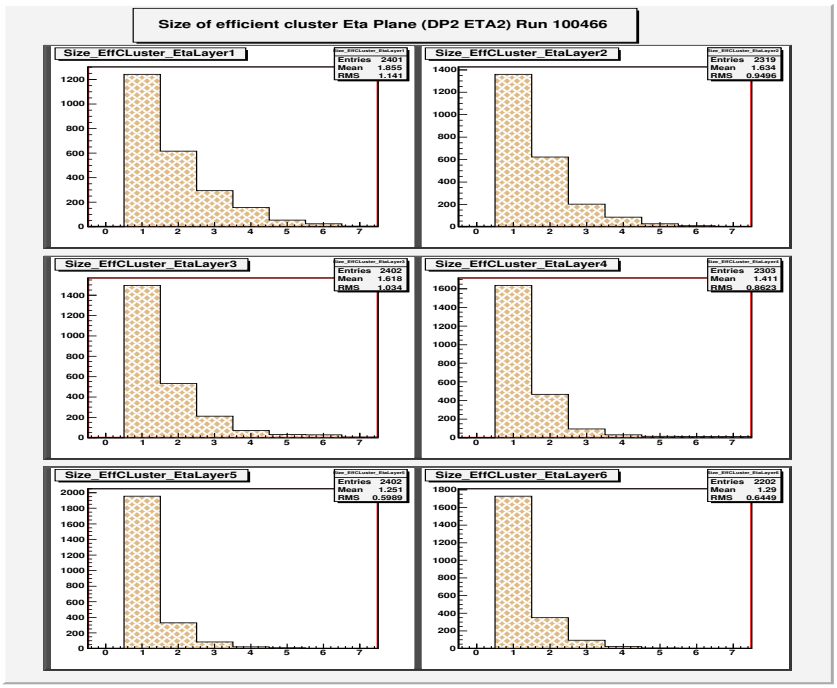

Figure 6.21: *Size of the efficient cluster distributions for η view of a single trigger tower .*

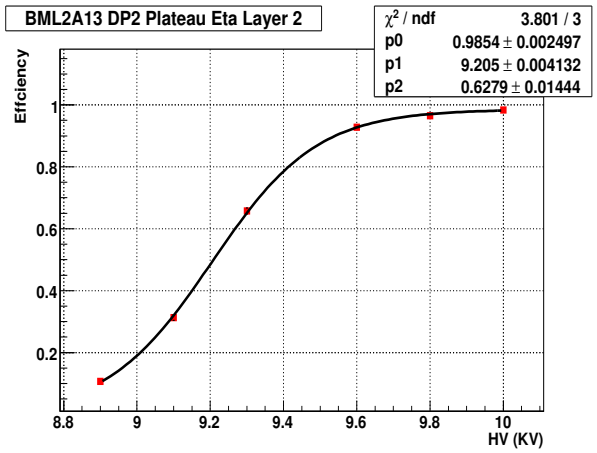

Figure 6.22: *Example of RPC plane efficiency curve as function of HV obtained with Sector 13 data.*

More efficiency curves and cluster size as function of HV are shown, an in fig. 6.23.

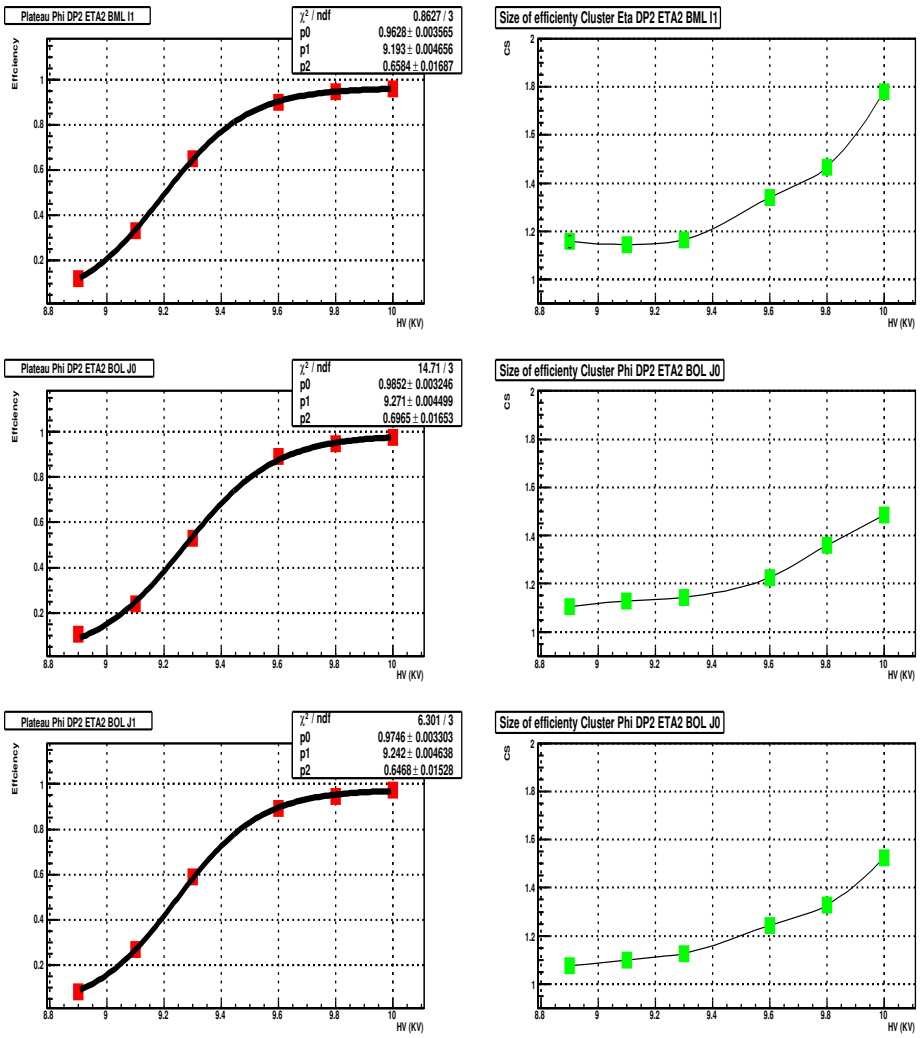

Figure 6.23: *Monitoring of efficiency and size of efficient clusters as function of HV.*

Fig.6.24 shows the top efficiency distribution at 9800 and 10000 Volts for all the 72 panels under test. Entries at low efficiency are relative to the plane with unplugged channels and low front end threshold. The fitted

average value of the distribution (without the panel at low efficiency) are respectively: 95.1 ± 0.2 for HV = 9800 Volts and 97.8 ± 0.1 for HV = 10000 Volts.

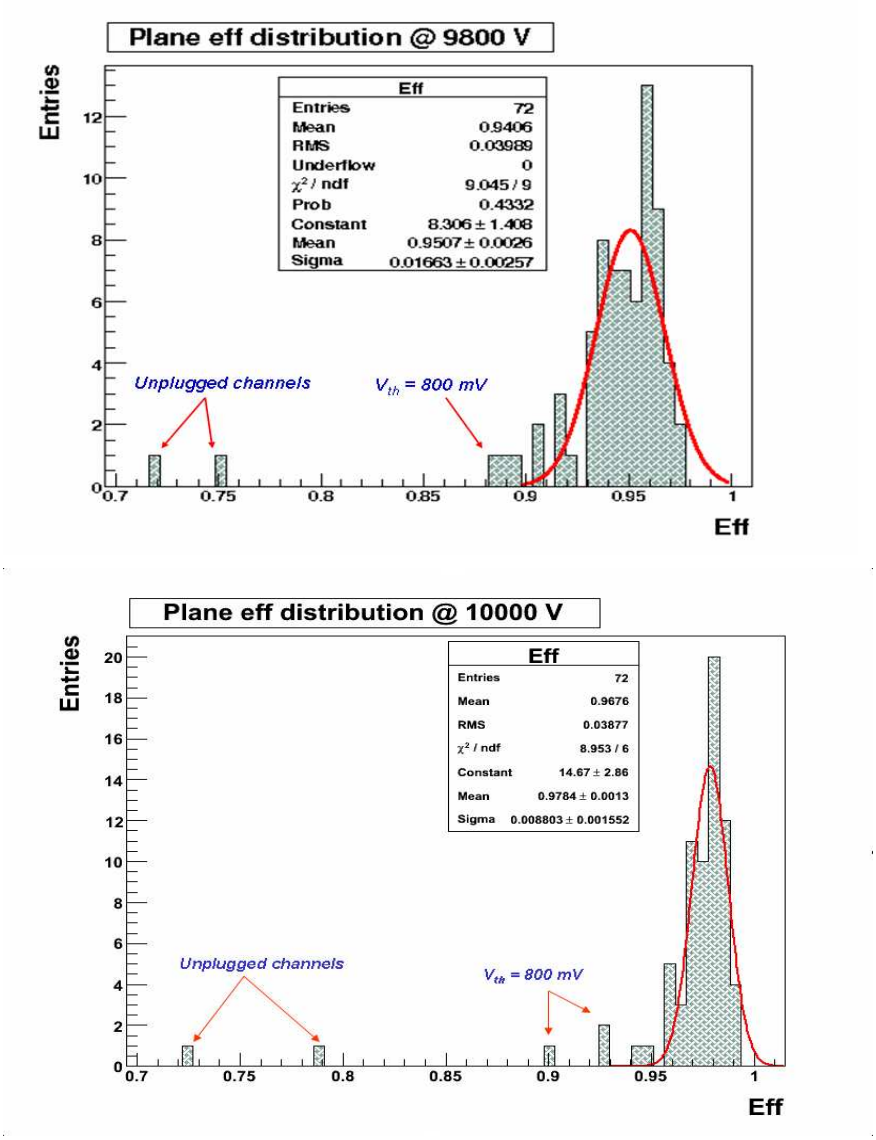

Figure 6.24: *Plane efficiency distribution for RPC in Sector 13 at* $V_{th} = 1000$ *mV. HV = 9800 V (on top), HV = 10000 V (bottom) .*

Fig.6.25 shows the size of the efficiency cluster distribution at 9800 and 10000 Volts.
The average value of the size of the efficient clusters are respectively: 1.4 at 9800 Volts and 1.6 at 10000 Volts.

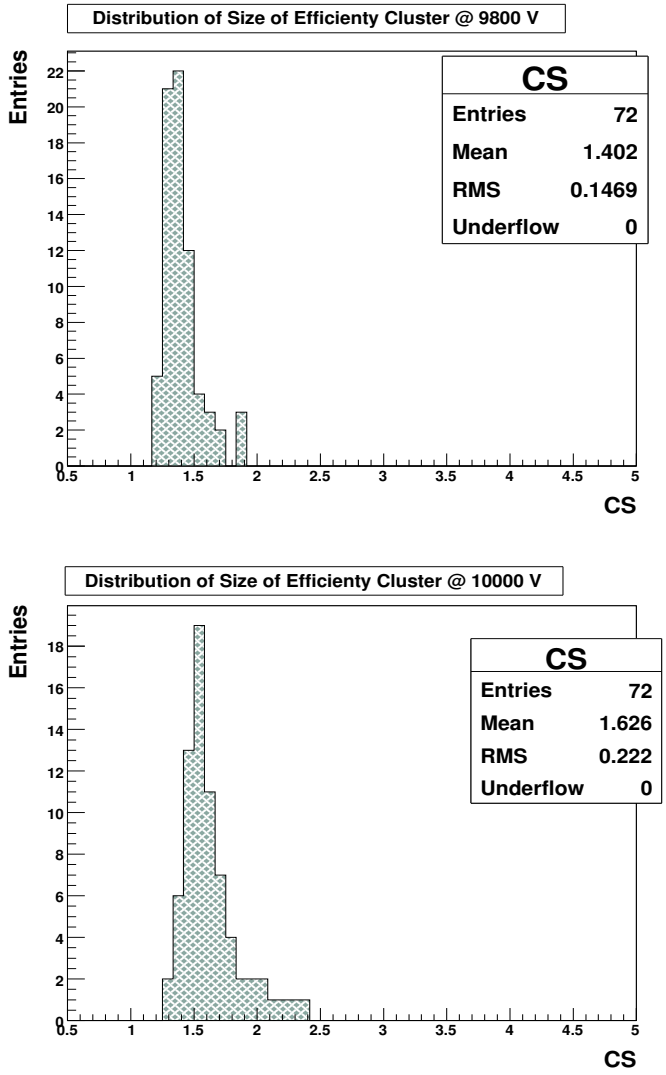

Figure 6.25: *Size of efficient clusters distribution for RPC in Sector 13 at* $V_{th} = 1000$ *mV. HV = 9800 V (on top), HV = 10000 V (bottom).*

The equivalent HV which one has to apply Lecce to reproduce the CERN test condition came from the empirical formula for HV correction (eq. 5.5). For CERN condition $T = 20^0C$ and $P = 980$ mbar became HV = 10026 V for HV = 9800 V and HV = 10231 V for HV = 10000 V. Fig. 6.26 shows the distribution obtained with Lecce data applying the same condition of CERN Sector 13 test (HV = 10231 V for HV = 10000 V).

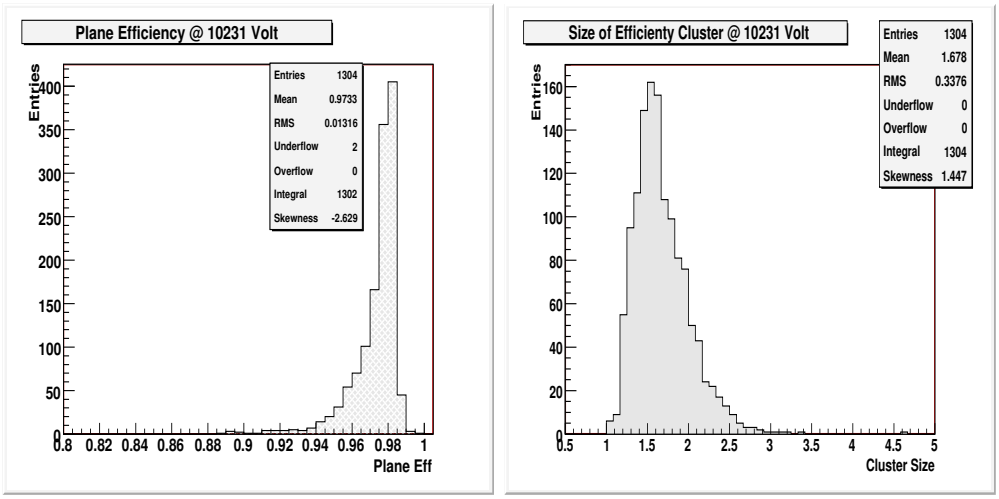

Figure 6.26: *Distribution obtained with Lecce data applying the same condition of CERN Sector 13 test.*

Comparing the results they appear in perfect agreement confirming the quality of test performed at the test stand and the correct calibration for temperature and pressure.

6.8 Conclusions

An exercise of pre-commissioning on ATLAS Sector 13 muon chambers has been done. All the electronic chain from the front-end to the DAQ has been tested. A dedicated RPC standalone reconstruction software has been developed and successfully tested. Many software tools have been realized in order to decode, understand and verify the raw data. First performance results satisfy the expectation, in particular the average value of plane

efficiency is above 95% and the average cluster size at 9800 V ($T = 20^0C$ and $P = 980$ mbar) is below 1.5 as ATLAS request.

Summary and Outlook

ATLAS is a general purpose experiment designed for the proton-proton Large Hadron Collider at CERN in Geneva. In order to minimize the muon multiple scattering an Air Core Toroidal Muon Spectrometer has been designed and realized. Resistive Plate Chamber, subject of this thesis, was chosen as trigger detector for muons in the barrel region. The studies presented in this thesis are a part of the large effort required to design and built a detector with the size and complexity of the ATLAS experiment.

1116 RPC units covering a total surface of about $4000m^2$ have been assembled at Lecce production facility. A cosmic ray test stand at Lecce Physics Departments and INFN has been built and it is capable of routinely testing ATLAS RPC units. An automatic test procedure has been implemented in order to minimize the test time and standardize the procedure. Dynamic web page linked to a MySQL database was realized to allow data and results presentation. During the 18 months of test 380 units have been certified and delivered to the CERN for the installation on the ATLAS apparatus.

A systematic ATLAS RPC characterization was given using for the first time a very large sample of detectors. The main properties of the detector have been extensively studied, the results showed that the RPC produced fulfill the ATLAS requirements. In particular noise, cluster size and currents are under control.

A performances dependence from temperature and pressure has been found, and specific correction to the data has been obtained for the first time. The nature of this particular behavior is under investigation.
Moreover extensive study of detector response for large temperature variation was performed finding sensible increase of the dark current with temperature

due both to the ohmic and to the multiplicative components of the current-voltage characteristics. In addition, a clear correlation is found between the multiplicative component of the dark current and the noise rate. This can be interpreted as due to a saturated avalanche regime where the saturated charge scales only linearly with the applied electric field. A low temperature of operation is preferable in ATLAS, in order to keep dark currents and noise rate as low as possible. Nevertheless, since in the ATLAS experiment a beam related background of about 10 Hz/cm^2 is expected, aging phenomena will likely be dominated by this noise component more than high temperature effects.

Finally a working point for all the Barrel Outer Chamber of ATLAS has been defined and extensively characterized. This is an useful step for the ATLAS commissioning phase.

In last year of my PhD I spent about six months at CERN laboratory; during this time an exercise of pre-commissioning on ATLAS Sector 13 muon chambers has been done. All the electronic chain from the front-end to DAQ has been tested. A dedicate RPC standalone reconstruction software has been developed and tested. Many software tools have been realized in order to decoding and understand the raw data. First performance results satisfy the expectation, in particular the average value of plane efficiency is above 95% and the average cluster size at 9800 V ($T = 20^0C$ and $P = 980$ mbar) is below 1.5 as ATLAS requests. The standalone program realized for Sector 13 cold be used for the commissioning of the entire ATLAS muon spectrometer. An automatic procedure of test and analysis have to be implemented for the final commissioning. The very large amount of plots necessary to certificate each trigger tower require a dedicate web page to allow at the user to find rapidly the informations.

Bibliography

[1] S.Weimber, Phys. Rev. Lett. 19 (1967) 1264.

[2] S. Glashow, Nucl. Phys. B 22,(1961) 579.

[3] C. N. Yang and R. L. Mills, Phy. Rev. 96 (1954) 191.

[4] F. Halzen e A.D. Martin: *QUARKS AND LEPTONS An Introductory Course in Modern Particle Physics.* John Wiley e Sons New York 1984.

[5] A. Salam, *Elementary Particle Theory.* Ed. N. Svartholm (1968).

[6] S. Weinberg: *Recent Progress in the Gauge Theories of the Weak and Electromagnetic Interaction.* Rev. Mod. Phys. 46, 255, (1974).

[7] Gargamelle Collaboration: F.J. Hasert et al. Phys Lect. 46B, 138 (1973).

[8] *Recent Result from the UA1 Experiment* at CERN. SLAC Pubs and Reports SS186-013.

[9] G.'t Hooft, Nuclear Physiscs B33, (1971) 173, Nuclear Physics B35 (1971) 167.

[10] J.Erlr, *Phys. Rev.* D 63 (2001).

[11] LEP Higgs Working group for Higgs boson serches, *Search for the Standard Model Higgs boson al LEP*, CERN-EP /2001-055.

[12] J.F.Gunion, H.E.Haber, G.Kane and S.Dawson:*The Higgs Hunter Guide*, Perseus Publishing, Cambridge, Massachussets,(2000)

[13] T. Hambye and K. Riesselmann *SM Higgs mass bounds from theory*, arXiv:hep-ph/9708416

[14] CDF Collaboration, *Phys Rev.* D50 2966, 1994; *Phys Rev.* D51 4623, (1995); *Phys. Rev.Lett.* 74 2626, 1995.

[15] Aitchison Ian J. R., *Supersimmetry and SMMS: An Elementary Introduction*, hep-ep/0505105 v1 May 2005.

[16] Y. Golfand and E. Liktam, JEPT Lett. 13 (1971) 323.

[17] J. Wess and B. Zumino, Nucl. Phys. B78 (1974) 39.

[18] General reviews of SUSY include H.P. Nilles, Phys. Rep. 111 (1984) 1.

[19] Keith R. Dienes, String theory and the path to unification: A review of recent developments, *Phys. Rept* 287, 447-524 (1997), hep-th/9602045.

[20] W-M Yao et al., J. Phys. G: Nucl. Part. Phys. 33 (2006) 1.

[21] Asai S. et al. Prospect for the search of a standard model higgs boson in atlas using vector boson fusion. *ATLAS internal note*, SN-ATLAS-2003-024, 4004.

[22] ATLAS Collaboration. *ATLAS Detector and Physics Performance Technical Desing Report*. CERN/LHCC/99-15, 99-16, (1999).

[23] Jakobs K. and Tresfger T. SM higgs searches for $H \rightarrow WW^* \rightarrow l\nu l\nu$ with a mass between 150 - 190 gev at LHC. *ATLAS internal note*, ATLAS-PHYS-COM-99-031, (1999).

[24] Savard P. and Azuelos G. The discovery potential of a heavy higgs ($m_H = 800GeV$) using full simulation of ATLAS.*ATLAS internal note*, ATLAS-PHYS-98-128, (1998)

[25] Ruiz H. and Bosman M. The discovery potential of heavy SM higgs boson through the $H \rightarrow ZZ \rightarrow ll\nu\nu$ channel at LHC with ATLAS detector. *ATLAS internal note*,ATLAS-PHYS-2002-027, 2002.

[26] G.Gomez-Ceballos and J.Piedra, *B Mixing and Lifetimes at the Tevatron*, hep-ex/0606048 (2006).

[27] *The Large Hardon Collider Accelerator Project*, LHC CERN-AC-93-03.

[28] *The Large Hardon Collider Accelerator Project*, LHC CERN-AC-95-05.

[29] LHC Collaboration, *LHC Technical Desing Report*,htt://ab-dv.web.cern.ch/ab-dv/Publications/LHC-DesignReport.html .

[30] M.Lamot, *Estimates of Annual Proton Doses in the LHC*, LHC Project Note 375.

[31] R.Bailey et al., *Overall Strategy for Early Luminosity Operation with Protons*, CERN EDMS Document LHC-OP-BCP-001 (2004).

[32] ATLAS Magnet Project Collaboration, CERN-ATLAS Team *ATLAS Magnet System Technical Design Report*. CERN/LHCC/97-18, (1997).

[33] ATLAS Magnet Project Collaboration, Central Solenoid Group *ATLAS Central Solenoid Technical Design Report*. CERN/LHCC/97-21, (1997).

[34] ATLAS Magnet Project Collaboration, Barrel Toroid Group *ATLAS Barrel Toroid Technical Design Report*. CERN/LHCC/97-19, (1997).

[35] ATLAS Inner Detector Community, *ATLAS Inner Detector Technical Design Report*. CERN/LHCC/97-16, (1997).

[36] ATLAS LARG Unit, *Liquid Argon Calorimeter Technical Design Report*. CERN/LHCC/96-41, (1996).

[37] ATLAS Collaboration, *Calorimeter Performance Technical Design Report*. CERN/LHCC/96-40, (1996).

[38] M. Fanti, *Optimatization of performance of the ATLAS electromagnetic calorimeter* Nuclear Physics B (Proc. Suppl.) 125 (2003) 117-121.

[39] ATLAS Tile Calorimeter Collaboration, *Tile Calorimeter Technical Design Report*. CERN/LHCC/96-42, (1996).

[40] P.Schacht et al., *Hadronic calibration of the ATLAS liquid argon end-cap calorimeter in the pseudorapidity region* $1.6 < |\eta| < 1.8$ *in beam test* Nuclear Instruments and Methods A 531, 481- 514 (2004).

[41] ATLAS Muon Collaboration, *ATLAS Muon Spectrometer Technical Design Report*. CERN/LHCC/97-22, (1997).

[42] M. Dikken et al., *The RASNIK In-Plane Alignment system* ATL-MUON-97-184 (1997).

[43] G. Aielli et al., *Performance of a large size RPC equipped with the final ATLAS front-end electronics at X5-GIF irradiation facility.* Nuclear Instruments and Methods A 456, 77- 81 (2000).

[44] ATLAS Trigger Performance Group, *ATLAS Trigger Performance Status Report.* CERN/LHCC/98-15, (1998).

[45] R. Santonico R. Cardarelli: *Development of resistive plate counters.* Nuclear Instruments and Methods, 187 (1981) 377.

[46] F. Bella, C. Franzinetti: *Nuovo Cimento 10.* 1335-1461, 1953,
Yu. N. Pestov et al., *A spark counter with large area*, Nuclear Instruments and Methods, 93, (1971) 269-276.

[47] R.Cardarelli, V.Makeev, R.Santonico: *Avalance and streamer mode operation of resistive plate chambers.* Nuclear Instruments and Methods A 382, 470- 474 (1996).

[48] H. Raether: *Electron avalanche and breakdown in gases.* London Butterworths 1964.

[49] P. Camarri, R. Cardarelli, A. Di Ciaccio, R. Santonico: *Streamer suppression with* SF_6 Nuclear Instruments and Methods, 414, (1998) 317.

[50] G.Aielli et al., *Performance of a large-size RPC equipped with the final ATLAS front-end electronics at X5-GIF irradiation facility* .Nuclear Instruments and Methods A 456 (2000) 77-81

[51] R. Perrino et al., *The fcility for ATLAS Resistive Plate Chambers Assembly.* Nuclear Instruments and Methods A 508 (2003) 116-119.

[52] M. Alviggi et al., *Cosmic ray test station for ATLAS RPC.* Nuclear Instruments and Methods A 508 (2003) 124-127

[53] M. Bianco et al., *The Lecce cosmic ray testing facility for the ATLAS RPC.* Nuclear Instruments and Methods A 565 (2006) 450-456

[54] M. Bianco: *Sistema di acquisizione dati e risultati preliminari della stazione di test degli RPC di ATLAS.* Bachelor thesis: UNIVERSITÀ DEGLI STUDI di Lecce A.A. 2002/2003.

[55] G. F. Tassielli: *Sistema di controllo e risultati preliminari della stazione di test degli RPC di ATLAS.* Bachelor thesis UNIVERSITÀ DEGLI STUDI di Lecce A.A. 2002/2003.

[56] http://www.caen.it/computing/opc_server.html

[57] R. Assiro e P. Creti: Atlas Latch VME, Technical Information. INFN-LE March 2000.

[58] R. Cardarelli e A.Di Ciaccio: *First-Level trigger for LHC experiment.* RD27 Status Report 9 Jan (1994).

[59] http://www.ni.com

[60] M. Abbrescia et al.,: *Resistive plate chambers performances at cosmics rays fluxes* Nuclear Instruments and Methods A 359 (1995) 603-609.

[61] ATLAS RPC Collaboration: *Resistive Plate Chambers, Production Readiness Review Documentation* CERN (1999).

[62] M. Bianco et al., *Temperature dependent performance of ATLAS RPC.* Nuclear Physics B 158 (2006) 204-207.

[63] G. Chiodini et al., *ATLAS RPC termal studies.* Nuclear Instruments and Methods A 572 (2007) 36-37.

[64] G. Aielli et al., *Saturated logistic avalanche model.* Nuclear Instruments and Methods A 508 (2003) 6-13.

[65] A. Digirolamo et al., *Assembly and Certification of ATLAS Muon Stations for Middle and Outer Barrel at CERN.* ATL-MUON-PUB-2007-001.

[66] ATLAS Computing Group, *ATLAS Computing Technical Design Report.* ATLAS TDR-017, CERN/LHCC/2005-022, (2005).

[67] http://root.cern.ch/

[68] Mario Caprio:*Integration and Test of RPC Trigger Chambers in the H8 ATLAS Test Beam Activity* PhD Thesis (2004).

[69] M.Bianco et al., *Test Beam results and integration of the ATLAS Level-1 Muon Barrel Trigger* ATL-DAQ-CONF-2005-012 Geneva CERN 2005.

Ringraziamenti

Grazie a Chiara per essere stata ogni giorno al mio fianco e per aver condiviso in questi anni sentimenti, speranze, gioie e momenti difficili.